MODELING, IDENTIFICATION AND CONTROL OF A WHEELED BALANCING SYSTEM

A Dissertation
Presented to
The Academic Faculty

by

Daniel D. Murdock

In Partial Fulfillment
of the Requirements for the Degree
Doctor of Philosophy in
Electrical and Computer Engineering

School of Electrical and Computer Engineering
Georgia Institute of Technology
December 2016

MODELING, IDENTIFICATION AND CONTROL OF A WHEELED BALANCING SYSTEM

Approved by:

Dr. David Taylor, Advisor
Professor, School of ECE
Georgia Institute of Technology

Dr. Aldo Ferri
Professor, School of ME
Georgia Institute of Technology

Dr. Yorai Wardi
Professor, School of ECE
Georgia Institute of Technology

Dr. Allen Robinson
Academic Professional, School of ECE
Georgia Institute of Technology

Dr. Bonnie Ferri
Professor, School of ECE
Georgia Institute of Technology

Date Approved: 15 September 2016

To LD,

You inspired me to become 3D

-Dr. Daniel David

ACKNOWLEDGEMENTS

I want to thank my advisor Dr. David Taylor for giving me the opportunity to be his teaching assistant throughout much of my time at Georgia Tech. While working with him in the digital control system design lab, I was able to guide top caliber students, develop my teaching skills, and refine my digital implementation techniques. Under his supervision, I am proud to have earned the CETL BP 2013-2014 Outstanding Teaching Assistant Award. Without his guidance, I would not have turned my engineering skill into a scalpel.

I want to thank Dr. Nagy Bengiamin, Dr. Pete Kinman, and Sven Fagerstrom for their contributions to my academic pursuits during the early years of my graduate studies. They inspired me to solve problems creatively, and it is because of my interactions with them that I can wield my engineering skill like a paint brush. Without them, I would not have developed the confidence in my engineering ability that I now have.

I want to thank CJ, Aunt Donna, and Mike for being the people that I did not want to disappoint; and I have to thank Rob, Chris, Jessica, and Irene for helping me stay mentally grounded. I also must thank my first electronics instructor Mr. Jim Simpson for introducing me to the electrical subject.

Collectively these are the people who believed in me even when I didn't believe in myself. Without them, I would not have tried twice as hard to succeed.

TABLE OF CONTENTS

DEDICATION . . . . . **iii**

ACKNOWLEDGEMENTS . . . . . **iv**

LIST OF TABLES . . . . . **ix**

LIST OF FIGURES . . . . . **x**

SUMMARY . . . . . **xii**

I INTRODUCTION **1**

II LITERATURE SURVEY **4**

2.1 The RWP Balance System 4

2.2 The WIP Balance System 7

2.3 Other Types of Balance Systems 9

2.4 Actuators for Balance Systems 12

2.5 Dissertation Outline 14

III MODELING **15**

3.1 Rigid Body Equations 15

3.2 Reaction Wheel Pendulum (RWP) 16

3.2.1 Pendulum Linkage 17

3.2.2 Inertia Wheel 18

3.2.3 Generalized Forces 19

3.2.4 Equations of Motion 19

3.3 Two Wheeled Axle (TWA) 19

3.3.1 Axle Linkage 20

3.3.2 Right Wheel 22

3.3.3 Left Wheel 23

3.3.4 Generalized Forces 24

3.3.5 Equations of Motion 24

3.4 Wheeled Inverted Pendulum (WIP) 24

3.4.1 Pendulum 26

3.4.2 Right Wheel 27

3.4.3 Left Wheel . . . 27
3.4.4 Generalized Forces . . . 28
3.4.5 Equations of Motion . . . 29
3.4.5.1 Special Case Validation: Two-Wheeled Axle . . . 29
3.4.5.2 Special Case Validation: Pendulum Linkage . . . 29
3.5 Wheeled Balance System (WBS) . . . 30
3.5.1 Axle Linkage . . . 31
3.5.2 Right Wheel . . . 33
3.5.3 Left Wheel . . . 34
3.5.4 Pendulum Linkage . . . 35
3.5.5 Inertia Wheel . . . 36
3.5.6 Generalized Forces . . . 38
3.5.7 Equations of Motion . . . 39
3.5.7.1 Special Case Validation: RWP . . . 39
3.5.7.2 Special Case Validation: TWA . . . 39
3.5.7.3 Special Case Validation: WIP . . . 40
IV IDENTIFICATION . . . 41
4.1 Inertia Calculations . . . 41
4.1.1 RWP Pendulum and Wheel . . . 41
4.1.2 WIP Chassis and Wheels . . . 44
4.1.3 Ideal WBS Prototype . . . 47
4.2 Quantization Effects . . . 49
4.2.1 PWM Actuation . . . 51
4.2.2 Current Measurements . . . 52
4.2.3 Inertial Sensing . . . 53
4.2.4 Position Encoder . . . 54
4.3 ADC Calibration . . . 54
4.4 AC Motor Characterization . . . 56
4.4.1 Motor Dynamics . . . 57
4.4.2 AC Drive System . . . 58
4.4.3 τ vs. ω Curve . . . 61

4.4.4 Parameter Identification 61
4.4.4.1 Encoder Initialization 64
4.4.4.2 Friction 65
4.4.4.3 Inertia 66
4.4.4.4 Cogging Torque 67
4.4.4.5 Model Validation 70
4.5 DC Motor Characterization 71
4.5.1 Motor Dynamics 71
4.5.2 Drive System 73
4.5.3 τ vs. ω Curve 74
4.5.4 Parameter Identification 75
4.5.4.1 Friction 76
4.5.4.2 Inertia 77
4.5.4.3 Model Validation 79
4.5.4.4 Gearbox Backlash 79
V CONTROL 82
5.1 Reaction Wheel Pendulum 82
5.1.1 Equilibrium Analysis 82
5.1.2 Controller Design 83
5.1.2.1 Slow Subsystem 83
5.1.2.2 Fast Subsystem 86
5.1.3 Implementation 88
5.1.3.1 Disturbance Rejection 89
5.1.3.2 Experimental Results 90
5.2 Wheeled Inverted Pendulum 91
5.2.1 Equilibrium Analysis 92
5.2.2 Controller Design 94
5.2.2.1 Slow Subsystem 94
5.2.2.2 Fast Subsystem 97
5.2.2.3 Reference Tracking 99
5.2.3 Implementation 101

5.2.3.1 Sensor Kinematics 101
5.2.3.2 Disturbance Rejection 103
5.2.3.3 Equilibrium on Flat Ground 104
5.2.3.4 Equilibrium on Inclined Plane 104
5.2.3.5 Experimental Results 106
5.3 Wheeled Balancing System 107
5.3.1 Equilibrium Analysis 110
5.3.2 Controller Design 112
5.3.2.1 Slow Subsystem 112
5.3.2.2 Reference Tracking 114
5.3.3 Simulation Results 115
VI CONCLUSION 120
APPENDIX A — WBS DYNAMIC EQUATIONS 122
APPENDIX B — IMPLEMENTATION CONSIDERATIONS 123
APPENDIX C — WIP EQUILIBRIUM COMPUTATIONS 125
REFERENCES 126

LIST OF TABLES

1 RWP Parameters and Inertias 43
2 WIP Parameters and Inertias 46
3 Wheel Parameters and Inertias 47
4 WBS Parameters and Inertias 49
5 Implemented Quantization Resolutions 50
6 Gyroscope and Accelerometer Resolution Options 54
7 Parameter Values of the AC Motor 64
8 Parameter Values of the DC Motors 76
9 DC Motor Gear Play Characteristics 81
10 Determination of WIP Equilibria 94
11 Determination of WBS Equilibria 112

LIST OF FIGURES

1 The wheeled balancing system (WBS), viewed as a combination of a reaction wheel pendulum (RWP) and a wheeled inverted pendulum (WIP). 2

2 Pitch-axis balance with energy efficient control [4]. 10

3 Double pendulum with reaction wheel augmentation [38]. 11

4 Self tilt up using a flywheel mounted along the yaw-axis [57]. 11

5 RWP variable and axes convention. 17

6 TWA variable and axes convention. 21

7 WIP variable and axes convention. 25

8 (Left) WBS prototype concept. (Right) WBS variable and axes convention. 30

9 RWP construction diagram and physical implementation. 42

10 Actual chassis body for the WIP. 44

11 Approximate chassis body for the WIP. 44

12 (Left) Wheel axis convention. (Right) Wheels used to drive the WIP/WBS. 47

13 (Left) ideal WBS concept, (Right) approximate WBS construction. 48

14 A family of quantization DFs representing the effective signal gain. 51

15 PWM leg voltages are generated by amplifying gating signals. 52

16 A half-bridge leg with sense resistor and differential op-amp circuit. 53

17 Exaggerated quantization effect. 55

18 PM synchronous motor magnetics. 57

19 PM synchronous motor drive system. 58

20 PM synchronous motor torque vs. speed characteristic. 62

21 AC motor identification results from constant-speed experiments. 66

22 AC motor identification results from coast-down experiments. 68

23 AC motor identification results from cogging-alignment and rotation-voltage experiments. 70

24 $E + \Gamma$ as a function of number of harmonic terms. 71

25 AC motor model validation, using $H = 6$; measurement versus simulation. . 72

26 DC motor magnetics. 72

27 DC motor drive system. 73

28 DC motor torque vs. speed characteristic. 75
29 DC motor identification results from constant-speed experiments. 78
30 DC motor identification results from coast-down experiments. 79
31 DC motor model validation; measurement versus simulation. 80
32 Experimental gear play measurements. 80
33 DC motor gearbox backlash models. 81
34 RWP digital implementation timing diagram. 88
35 (Left) Sensor bias and (Right) platform rotation defects. 90
36 RWP sensor bias rejection. 90
37 Experimental RWP sensor bias and platform rotation compensation. 91
38 RWP prototype expeiencing intentional sensor bias and platform shift. . . . 92
39 WIP regulator eigenvalue test: $\bar{v} \in [-10, 10]$, $\bar{\dot{\phi}} \in [-6.28, 6.28]$. 100
40 WIP estimator eigenvalue test: $\bar{v} \in [-10, 10]$, $\bar{\dot{\phi}} \in [-6.28, 6.28]$. 100
41 WBS digital implementation timing diagram. 102
42 WIP static analysis on incline. 104
43 (Top) WIP standing on an incline. (Bottom) Illustrating the effect of operating on a variable incline. 105
44 WIP pitch equilibrium deviation as a function of incline angle. 106
45 WIP torque equilibrium as a function of incline angle. 107
46 WIP standing upright while balancing a glass of wine. 108
47 WIP on flat ground responding to translation commands. 109
48 WIP on flat ground responding to rotation commands. 109
49 WBS regulator eigenvalue test: $\bar{v} \in [-10, 10]$, $\bar{\dot{\phi}} \in [-6.28, 6.28]$, $\bar{\dot{\delta}} = 0$. . . . 115
50 (Left) WBS navigating an S-curve slalom, and (Right) one wheel going over a speed bump. 116
51 WBS angle responses to an S-curve trajectory. 116
52 WBS velocity responses to an S-curve trajectory. 117
53 WBS commanded inputs for an S-curve trajectory. 117
54 WBS angle responses to asymmetrical wheel lift. 118
55 WBS velocity responses to asymmetrical wheel lift. 119
56 WBS commanded inputs for asymmetrical wheel lift. 119

SUMMARY

The purpose of this research is to develop a comprehensive modeling, identification, and control methodology for several inverted balancing systems. Symbolic software tools are created based on the general dynamic equation to derive the equations of motion for each system. Embedded programming techniques are designed and implemented to acquire data, perform sensor calibration, and impose actuator voltages. Actuator nonlinearities are characterized using only the hardware intended for implementation by processing the measured responses to specific embedded experiments; this low-cost approach does not require additional measurement devices or other expensive high-precision equipment. State-space integral controllers are designed to perform robust output feedback compensation and accomplish reference tracking. Several practical implementation issues are investigated such as disturbance rejection, digital controller design, switched mode reference tracking, and integrator anti-windup. Before implementation, a software environment is created to predict system performance with high-fidelity by testing how the full-order nonlinear plant dynamics respond to the two-time scale controller design while accounting for higher order friction effects, cogging torque, gearbox backlash, sensor bias, and parameter mismatch. The three applications this methodology is applied to are the reaction wheel pendulum (RWP), wheeled inverted pendulum (WIP), and wheeled balancing system (WBS); where the WBS is by definition a mechanical superposition of RWP and WIP technologies. Simulated predictions of the RWP and WIP are strongly validated by experimental measurements, and the developed methodology is theoretically applied in simulation to prove the success of the WBS concept.

CHAPTER I

INTRODUCTION

The objective of the research in this dissertation is to develop modeling, identification and control methods for a novel two-axis pendulum on wheels, referred to as a wheeled balancing system or WBS. The WBS is a mobile platform with an inverted pendulum payload as seen in Figure 1, and it may be viewed as a combination of a reaction wheel pendulum (RWP) and a wheeled inverted pendulum (WIP). The platform freely rotates along the pitch-axis, and the payload freely rotates along the roll-axis. Motors actuate the two wheels in ground contact to stabilize pitch motions, drive yaw-axis rotations, and impose linear translations. The reaction principle is used to stabilize roll-axis payload motions, by driving a motor with an inertia load, connected at the non-pivoting pendulum end. The first control objective is to stabilize the pendulum payload angle while it is experiencing centripetal acceleration, and the second objective is to keep the pendulum payload upright when only one wheel goes over a bump (or falls in a hole).

Symbolic software tools are developed based on the general dynamic equation, to derive the equations of motion for a sequence of mechanical systems that exhibit increasing levels of complexity including the RWP, two-wheeled axle (TWA), WIP, and WBS. The general dynamic equation has a simple implementation recipe that utilizes quasi-velocities to yield a minimum set of first-order dynamic equations, even when the system is subject to nonholonomic constraints. We show that when the WBS dynamics are subject to special assumptions that the RWP, TWA, and WIP are all special cases of the WBS problem.

The development of a high-fidelity simulation model is completed by measuring or deriving parameter coefficients, sensor imperfections, actuator nonlinearities, and drive system operating limits. Embedded programming techniques are designed and implemented to

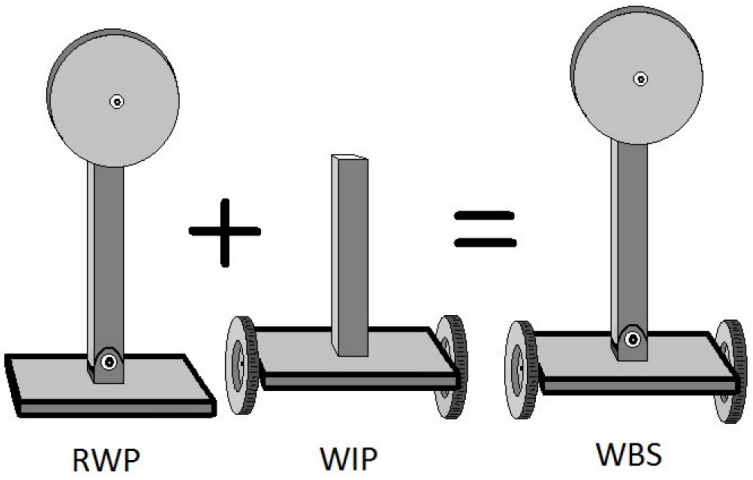

Figure 1: The wheeled balancing system (WBS), viewed as a combination of a reaction wheel pendulum (RWP) and a wheeled inverted pendulum (WIP).

acquire data, perform sensor calibration, and impose actuator voltages. Hardware characterization is performed using only the equipment intended for implementation by processing the measured responses to specific embedded experiments; this low-cost approach does not require additional measurement devices or other expensive high-precision equipment. As a result of following the developed procedures in Chapter 4, simulation trials can be conducted that accurately predict the plant model performance under the influence of a particular controller design without risking hardware damage.

After using the developed dynamic models to determine all candidate equilibria, a state-space integral controller is designed to provide robust feedback for reference tracking. Several practical implementation issues are investigated such as disturbance rejection, digital controller design, switched mode reference tracking, and integrator anti-windup. Before implementation, a software environment is created to predict system performance with high-fidelity by testing how the full-order nonlinear plant dynamics respond to the two-time scale controller design while accounting for higher order friction effects, cogging torque, gearbox backlash, sensor bias, and parameter mismatch. Simulated predictions of the RWP and WIP strongly agree with experimental measurements, and the developed methodology is

theoretically applied to the WBS in simulation.

The main contribution of this work is providing the first development of the WBS model, successfully controlling it in simulation, and demonstrating the cancellation of centripetal acceleration acting on the pendulum payload. The RWP application is extended in several directions by modeling the dynamics with the general dynamic equation, providing the first experimental demonstration of inertia wheel position tracking, and successfully rejecting the effects of sensor bias, cogging torque, higher-order friction, and disturbances due to operating on uneven terrain. The WIP application is studied comprehensively covering topics that include dynamic modeling, hardware characterization, two-time scale state-space integral controller design, robust reference tracking while switching between equilibria, and disturbance rejection of sensor bias while operating on uneven terrain.

The primary goal of this research is to prove the WBS concept can cancel out the effect of centripetal acceleration acting on the pendulum payload, thus demonstrating the viability of a novel safety device that can reduce the quantity of accidents and severity of harm that may come to human riders operating commercial WIP products. The improvement of WIP safety margins is just one outcome of this research that positively impacts the quality of human life. For example, any project requiring improvements to balance can benefit from the RWP research; e.g. providing balance/walking assistance for the elderly, or improving covert military infiltration techniques. Also, the benefits of integrating the presented actuator characterization techniques include improving hardware-in-the-loop (HIL) design methodologies and reducing the risk of catastrophic damage caused by torque disturbances during telepresent surgical operations.

CHAPTER II

LITERATURE SURVEY

The RWP and WIP systems actuate in different ways, and the WBS system represents a fusion of both technologies. Broad-scope investigations independently assess RWP and WIP state-of-the-art to determine how the applications have been studied and overlapped. The literature survey is synthesized into four sections: The RWP Balance System, The WIP Balance System, Other Types of Balance Systems, and Actuators for Balance Systems.

2.1 The RWP Balance System

The RWP is an inverted system connected on opposite ends to a freely rotating pivot and to an actuator driving an inertia-disk load, as seen in Figure 1. The RWP is stabilized by commanding torque inducing motions in a plane parallel to the un-driven pivot. The RWP is an underactuated mechanical system, meaning it possesses fewer actuators than degrees of freedom; it also has unstable open-loop plant dynamics at the vertical position. In [1], a comprehensive treatment of the RWP provides information relevant for both education and research. After originally being introduced in [2], the RWP has been well studied. The reaction principle has been utilized to balance a one-wheeled robot [3], perform WIP balance assistance [4], balance a 3D-pendulum cube on one corner [5,6], and model humanoid robot poses with variable inertia RWP models [7].

Accurate plant modeling is required to perform a proper controller design, and all nonlinearities need to be included in simulation trials to predict controller performance accurately. Typical RWP mathematical model development involves a Euler-Lagrange analysis; however, plant model dynamics and coefficients are occasionally obtained experimentally. In general, non-conservative forces are neglected during the RWP model derivation; however, throughout [8–13] viscous friction is assumed to be the only torque disturbance affecting rotor actuation. In [14], parameter identification is used to obtain actuator coefficients; however, the characterization is limited by not accounting for higher-order nonlinearity effects.

In [15], system identification is used to construct an RWP plant model from input/output data sets; however, the results are limited by not reporting and not validating the identified model nonlinearities. In general, the limit-cycling performances and steady-state errors measured throughout [4–6, 9–11, 16, 17] are undesirable outcomes that occur as a result of parameter uncertainty or model neglect. Higher-order nonlinearity effects such as Coulomb friction [1, 9] or rolling friction [14] are rarely considered during RWP investigations, and all previous RWP modeling efforts are limited by not accounting for Stribeck friction.

The two subproblems primarily associated with RWP control are: swing-up and balance. The swing-up subproblem offers an opportunity to solve both control objectives with one controller design. In [18] and [19], partial feedback linearization is simulated to control a three-state RWP model; however, all friction effects are ignored to simplify the feedback linearization transform. In [20], a backstepping technique is simulated to control a four-state RWP model; however, stability is proven by ignoring all friction effects during the search for an appropriate candidate Lyapunov function. In [12], nested saturation functions are simulated to control the four-state RWP while considering strong viscous damping; however, plant model coefficients are incorrectly computed (based on the reported values and relationships), and the control signal is permitted to vary arbitrarily high without concern for simulating hardware protection. In [21], experimental tracking of model-predictive control references are implemented on the three-state RWP model; however, all friction effects are ignored, and the reported results demonstrate a significant non-zero rotor speed at steady-state. All previous RWP investigations attempting to perform swing-up and balance in one design are limited by not experimentally demonstrating four-state RWP control.

Hybrid controller designs have been used to accomplish both RWP control objectives by switching between swing-up and balance methodologies. The most popular balancing solution utilizes a linear control design methodology on the three-state RWP while neglecting friction, and assuming that all state variables are perfectly measurable. Throughout [2,8,10,14,16,17,22–24], controlling the three-state RWP first involves performing swing-up and then switching to a different methodology for balance. Several swing-up variations

implemented as part of the hybrid design methodology are: simple bang-bang [8, 16], collocated partial feedback linearization [2], variable amplitude bang-bang [14], speed-gradient energy functions [22], reference-trajectory optimization [23], and a noteworthy mechanical alternative that uses high-speed internal collisions to generate swing-up momentum [6]. Several balancing variations implemented as part of the hybrid design methodology are: pole placement compensation utilizing discrete-time differentiation [1,8], feedback linearization [2], general PI control [16], sliding mode control (SMC) [22], fuzzy-logic control [17], dynamic surface control utilizing feedback linearization [24], and PID gain assignments utilizing genetic and particle swarm optimizations [10]. All previous RWP hybrid control strategies are limited by not experimentally demonstrating four-state RWP control.

One undesirable performance outcome commonly associated with RWP experimental trials is a steady-state error in rotor speed. In [1], the sensor bias measurement defect is theoretically predicted to cause persistent rotor rotation. During experimental implementation of [25], Murdock and Taylor observed that improper encoder initializations lead to the theoretically predicted defect in [1], and the measured steady-state errors reported in [10,17]. Throughout [2,8,14,16,18,19,21,22], sensor bias is avoided by performing system initialization at the stable equilibrium, and then swinging up to the unstable equilibrium; however, initialization at the stable equilibrium is not always possible. In [13], a nonlinear estimator is designed to reject bias error for a special class of systems including the three-state RWP, while assuming viscous friction is the only torque disturbance present. The methodology in [13] also requires simultaneously solving multiple PDEs, and once all RWP nonlinearities are considered this condition may not be achievable. All previous RWP studies involving sensor bias are limited by not experimentally demonstrating rejection of this defect.

Another undesirable performance outcome associated with RWP experimental trials is limit-cycling of the pendulum angle near the unstable equilibrium. Although some researchers have investigated robust tracking of sinusoidal pendulum angle references [11, 26–28], not achieving four-state RWP equilibrium is an undesirable performance outcome. In [25], we provide the first systematic presentation of a differentiator-free, output-feedback,

reduced-order control design methodology for an RWP based on multi-output loop transfer recovery procedures. During experimental implementation, we found that limit-cycling occurs at the vertical position due to quantization, cogging torque, and Stribeck friction effects. The procedures in Chapter 4 are used to predict the presence of limit-cycling behavior; however, all previous investigations are limited by not implementing experimental control over the four-state RWP model.

2.2 The WIP Balance System

The WIP is a two-wheeled mobile platform that freely rotates along the pitch-axis as seen in Figure 1. A rigid-body payload is stabilized by driving wheels that are in ground contact to provide yaw-axis rotations, and impose linear translations. Due to its mechanically underactuated nature and open-loop instability at the unstable equilibrium, the WIP has become a useful tool to teach control theory [29–31] and for researching prototype fabrication techniques [32, 33]. There are several considerations that complicate plant model selection such as robust consideration of passenger inertia [34], human-friendly disturbance rejection [35], and utilizing multiple connected masses for balance assistance [36–38]. In [39], a comprehensive review of modeling and control techniques for all types of two-wheeled mobile platforms is conducted; the review considered terrain variations, obstacle avoidance, swing suppression, and additional actuation sources.

Previous WIP plant modeling efforts slightly favor the Euler-Lagrange energy based approach [36, 40–48] over Newtonian free body derivations [30, 31, 34, 35, 49, 50]; however, Kane's method [51–53] and multi-body dynamic software packages (such as MotionGenesis or ADAMS) have occasionally been used [38, 54]. In one study [53], Kane's and Lagrange's methods are both used to validate the dynamic equations; however, the purpose of the study is to show how poor modeling assumptions propagate erroneous results when using Lagrange's method. Frequently the yaw axis rotation dynamics have been derived [31, 40, 42, 44–49, 52, 54–57]; however, most studies only focus on performing pitch balance and forward translation, and rarely WIP operation on an inclined surface is considered [39–43, 53]. WIP friction models sometimes account for viscous [32, 35–37, 41–43, 49, 58] and Coulomb [36, 41,

59] effects, while assuming the device undergoes pure rolling motion without slip. When WIP investigations contain a device fabrication component, or static and dynamic stress analyses, computer programs such as SolidWorks [29,58], or Ansys Workbench [32] are used to generate 3D models.

During WIP investigations, the yaw-axis dynamics are frequently considered [31, 42, 44–49, 52–57], and in one study the roll-axis angle is accounted for to perform terrain mapping [56]. In [60–62], experimental results are obtained for various control objectives; however, perfect balance is assumed during yaw rotations. Occasionally control laws are presented without a stability analysis or consideration for the yaw-axis dynamics [50,63], and one study performs manual calibration before implementing open-loop yaw control [33]. In [44], the yaw-axis dynamics are modeled and controlled by simulating partial feedback linearization; however, friction effects are neglected to simplify the feedback linearization transform. In [45], experimental results are obtained using a neural-fuzzy based approach; however, the planar motion and upright balance dynamics are improperly derived as separate subsystems, only point masses are considered, and the results report a significant wobble. In [57], WIP swing-up is implemented; however, the control methodology does not provide smooth motions and would likely cause discomfort for potential human operators. In rare cases [31, 42, 47, 49, 53], the yaw-axis dynamics are both developed with rigor and supported by experimental validation. Roll-axis stability is commonly assumed along with pure rolling motion without slip; however, the WIP does not have a roll-axis torque source [39, 54], and no investigation has attempted to provide roll-axis corrections.

WIP balance has been accomplished using several feedback control strategies including root-locus PID gain assignments [32], feedback linearization [44], SMC [41, 43, 46, 48], neural-fuzzy-logic compensation [45], adaptive PD control [64], LQR full state feedback [31, 33, 48, 52, 58], and a self tuning PID neural network [49]. Position reference following was accomplished by implementing a dedicated navigation-subsystem [50], by simulating a machine-learning algorithm to optimize path-planning [61], by tracking GPS coordinates [42], and by commanding polar position coordinates of arbitrary size [47]. Velocity tracking is simulated by implementing LQR full-state feedback [52], a two-level adaptive

controller [64] and an SMC [43, 48]. Other improvements include swing suppression by implementing LQR [29], energy based limit-cycle minimization using a passivity observer [59], custom BLDC motor driver design using logic gates [32], and pitch angle error tracking to improve motion transients [46, 47].

Since observability is a sufficient condition to implement output feedback, an observability analysis should be performed to validate the chosen sensor arrangement [55]. When attempting new sensor placement combinations, sensor fusion designs should be investigated [30,56,64] to prevent sensor noise from causing an undesirable performance [32]. Popular WIP sensor combinations include accelerometer and gyroscope [30,31,35,45,56,59,64], inclinometer and gyroscope [29, 49, 52]; and specific control objectives have been accomplished by utilizing either a gyroscope [50] or an inclinometer [40] individually. The most common sensor fusion methodologies include complementary filtering [30,64] and unscented Kalman filtering [58]; however, sensor data is sometimes fed back directly [32, 35, 45, 59]. Special sensory goals include terrain mapping [62], obstacle detection [60], and using fuzzy expert rules to optimize sensor fusion over various terrain elevations and surface types [56]. Typical challenges associated with the WIP sensory system include performing on-line sensor calibration [56, 60], overcoming steady-state offsets or limit-cycling [59], and compensating for noise introduced by feeding back differentiated encoder measurements or error introduced by integrating gyroscope drift [31, 52].

2.3 Other Types of Balance Systems

Other studies considered within this survey scope are investigations that integrate reaction wheel technology, investigations considering alternative means of WIP payload stabilization, and investigations that study human-WIP interaction. In §2.1, a comprehensive review of all modeling and control techniques for the RWP system was conducted. In [39], a comprehensive review of modeling and control techniques for all types of two-wheeled mobile platforms is conducted and supplemented by the WIP survey in §2.2. There is very limited overlap spanning RWP and WIP technologies.

Non-WIP applications integrating reaction wheels include a Lego cart platform with

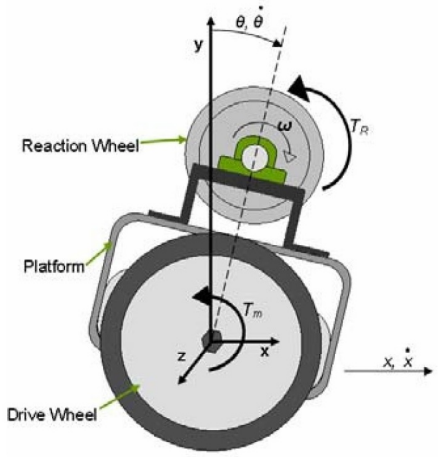

Figure 2: Pitch-axis balance with energy efficient control [4].

RWP payload [9], a 3D pendulum cube balancing on one corner [5,6], and a one wheel robot maintaining balance [3]. In the first recorded combination of WIP and RWP technologies [4], an inverted mobile platform is augmented with a rigidly connected RWP payload to demonstrate energy efficient control along the pitch-axis, as seen in Figure 2. In [4], the yaw-axis dynamics are not considered, all friction effects are neglected, and the reported results exhibit significant oscillations. Note that if the wheels in Figure 2 do not rotate then the dynamics of that device reduce to the RWP balance problem studied in §5.1. In the second recorded combination of WIP and RWP technologies [38], a double inverted pendulum is augmented with a rigidly connected reaction wheel (depicted in Figure 3) and simulated to demonstrate improved balance.

Non-RWP studies investigating other WIP payload stabilization enhancements include simulating virtual payload variations [34], providing human-friendly motion control [35], integrating multiple-linked masses to provide additional balance improvements [36,37], and designing the WIP to possess a COG below the wheel axis [65]. The first recorded WIP swing-up implementation [57] utilizes conservation of angular momentum by mounting a flywheel along the yaw-axis as seen in Figure 4; however, the oscillatory swing-up motions are not designed for a human passenger. One noteworthy attempt to prevent tip-over of a track-tread cart system investigates the algorithm effectiveness of heuristic tip-over controller designs [66].

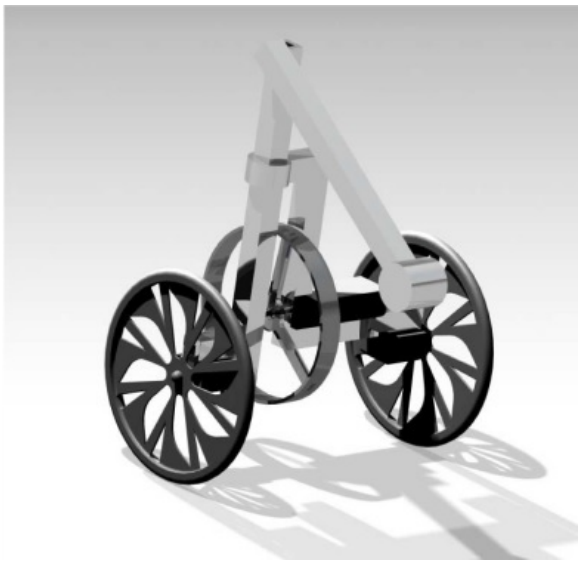

Figure 3: Double pendulum with reaction wheel augmentation [38].

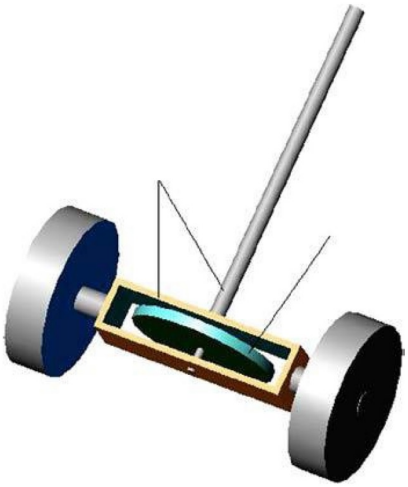

Figure 4: Self tilt up using a flywheel mounted along the yaw-axis [57].

A human WIP operator behaves like a variable inertia RWP [7], which adaptively shifts load inertia like an interconnection of springs and dampers to compensate for vibration modes [63]. The human rider plays a critical role in maintaining stability while maneuvering the WIP, and when cornering the device with a 'perfect' lean, then forces applied to the handlebar are at a minimum [63]. In [54], a safety article simulating various human-WIP (Segway Personal Transporter) operational hazards reported several major accidents, including instants of severe brain trauma; and concluded: "In fact, there is no physical mechanism on the machine that can be used to actively stabilize the roll dynamics." One researcher has studied how to incorporate an extra degree of freedom to cancel the effects of a centrifugal force by leaning the WIP apparatus [67]; however, any effort to design a device that provides WIP roll correction using RWP technology with or without human interaction is unprecedented.

2.4 Actuators for Balance Systems

There are several practical factors to consider prior to integrating an actuator into a particular application; such as weight, cost, and torque-speed capability. The actuator must be modeled adequately to accomplish the control objective, and in many cases important actuator characteristics are neglected to simplify plant model derivations. Many researchers implement more complicated control methodologies than needed to make up for using these oversimplified design models. Murdock and Taylor discovered while experimentally implementing [25] that limit-cycling occurs in the RWP application as a result of neglecting actuator cogging torque and Stribeck friction. In [68] and [69], comprehensive efforts to characterize AC and DC machines (including nonlinearities) are presented; however, a practical, accurate, and low-cost modeling alternative is still needed.

Although it is common to apply some actuator characterization efforts prior to implementation, several non-modeling based methods have been used to reduce the effect of nonlinearities and accomplish control objectives. In [70], an adaptive control method performs reference tracking while most motor parameters are initially unknown; however, Stribeck friction is neglected, and the identified cogging torque does not agree with torque

sensor measurements. In [71], a variable periodic disturbance rejection filter increases control effort in response to accurately measured disturbances; however, cogging effects are not necessarily periodic nor easily measured. In [72], a sensorless PMSM cogging torque compensation technique is developed; however, torque estimates are based on a velocity estimation method that requires the system to operate at speeds exceeding 2Hz. In [73], a feed-forward control strategy utilizes pulsating torque decoupling to generate identification data; however, by neglecting all friction effects the least-squares error residual lumps the effects of cogging and friction into one signal. Although some methods can reduce the effects of cogging torque without an explicit model, it is more practical to exert some characterization effort so that sophisticated control methods and special operating conditions are not required.

Rather than designing a complex controller, some researchers have chosen to implement elegant mechanical alterations. Post-manufacturing mechanical redesign and pre-fabrication magnetic optimization techniques usually involve finite element analysis. In [74], a comprehensive review of FEA optimal machine design techniques is presented. FE methods are used to design new machines with low-energy density magnets [75], and to analyze the source of audible noise attributed to cogging torque [76]. FE techniques are also used to identify cogging torque from ideal electromagnetic field computations [77], and to extrapolate the cogging waveform shape from a detailed analysis of one single stator slot [78]. All studies placing emphasis on the finite element method are limited by requiring very detailed knowledge about the motor interior and are unable to account for other physical properties such as friction.

Elaborate attempts to model AC PMSM nonlinearities include driving the motor under test with additional actuation devices and constructing multiple high-precision testing stations. In [79], an additional actuator provides a controllable load to drive the motor under test; however, the use of additional actuation devices increases the system order and the amount of effort required to perform characterization. In [69], the cogging and friction of a DC motor is characterized using multiple testing stations, a torque sensor, and an extraordinary high precision current amplifier. These methods are limited by using expensive

additional equipment not required during control implementation.

If the modeling exercise does not utilize physical principles, then an improper nonlinearity model will be constructed. Since cogging torque possesses symmetric characteristics, a nonlinearity model possessing multiple harmonic phase shifts [68, 80] or a DC offset [79, 80] would not have a reconstruction that agrees with physical expectations. In [81], a simulation study generated identification data from a disturbance observer while assuming Coulomb and viscous friction are present; however, actual experimental results would be contaminated by all other unmodeled disturbance effects. In [68], nonlinearities are characterized from constant speed experiments; however, after neglecting the cogging torque phase shift the nonlinearity model is appended with an artificial polynomial to make the data fit. In [80], a disturbance observer generating data for an offline least-squares identification is affected by other unmodeled disturbances resulting in a cogging torque model possessing multiple harmonic phase shifts and a DC offset. Since there is no guarantee that cogging torque is mechanically manufactured to align along any electrical phase, the cogging torque phase shift cannot be assumed to be zero and must be accounted for in a deterministic manner. All previous cogging torque modeling efforts are limited by not accounting for the cogging torque phase shift at the identification stage, which leads to a nonlinearity model that does not agree with physical principles.

2.5 Dissertation Outline

Chapter 3 provides detailed derivations for the system models used throughout this dissertation and demonstrates how each model is a special case of the WBS. In Chapter 4, procedures are developed that characterize system nonlinearities, coefficients, and actuator limits to obtain a high-fidelity plant model for simulation. The work in Chapter 5 utilizes the derived models to perform controller design, simulate controller performance and report experimental measurements. The dissertation is concluded in Chapter 6 with a summary of completed work and novel contributions.

CHAPTER III

MODELING

Throughout this chapter, the procedure in §3.1 has been adopted from [82] to derive the equations of motion for a sequence of mechanical systems exhibiting increasing levels of complexity. This method has a simple implementation utilizing quasi-velocities (us) as velocity variables and yields a minimum set of $(n-m)$ first-order dynamic equations for a system with n generalized coordinates (qs) and m independent nonholonomic constraints.

3.1 Rigid Body Equations

For a system of N rigid bodies, the ith rigid body has a reference point $\mathbf{O}_i \in \mathcal{R}^3$ fixed in the body, a scalar mass m_i, and an inertia dyadic $\mathbf{I}_i \in \mathcal{R}^{3\times 3}$ about $\mathbf{O}_i$. The applied forces acting on the ith rigid body are equivalent to a force $\mathbf{F}_i \in \mathcal{R}^3$ and a moment $\mathbf{M}_i \in \mathcal{R}^3$. The linear velocity $\mathbf{v}_i \in \mathcal{R}^3$ of reference point $\mathbf{O}_i$, and angular velocity $\boldsymbol{\omega}_i \in \mathcal{R}^3$ of the ith body are written in terms of quasi-velocities $\mathbf{u} \in \mathcal{R}^{n-m}$ which depend on the generalized coordinates $\mathbf{q} \in \mathcal{R}^n$ and time $t \in \mathcal{R}$,

$$\mathbf{v}_i = \sum_{j=1}^{n-m} \boldsymbol{\gamma}_{ij}(\mathbf{q},t)u_j + \boldsymbol{\gamma}_{it}(\mathbf{q},t)$$

$$\boldsymbol{\omega}_i = \sum_{j=1}^{n-m} \boldsymbol{\beta}_{ij}(\mathbf{q},t)u_j + \boldsymbol{\beta}_{it}(\mathbf{q},t)$$

where γs are called velocity coefficients, and βs are called angular velocity coefficients. [1] For both sets of coefficients the ij^{th}-component represents the body reference point sensitivity to changes in the quasi-velocities:

$$\boldsymbol{\gamma}_{ij} = \frac{\partial \mathbf{v}_i}{\partial u_j} \in \mathcal{R}^3, \quad \boldsymbol{\beta}_{ij} = \frac{\partial \boldsymbol{\omega}_i}{\partial u_j} \in \mathcal{R}^3 \quad (j = 1, \ldots, n-m),$$

and for a non-scleronomic system (when the constraint equations do not explicitly depend on time) we find $\gamma_{it} = \frac{\partial \mathbf{v}_i}{\partial t}$ and $\beta_{it} = \frac{\partial \boldsymbol{\omega}_i}{\partial t}$ are equal to zero.

[1] Throughout this chapter, $\mathbf{u}$ is a representation of some quasi-velocity and should not be confused with the variable typically associated with control input.

Once all linear and angular velocity coefficients are determined then the linear momentum rate $\dot{\mathbf{p}}_\mathbf{i} \in \mathcal{R}^3$ and angular momentum rate $\dot{\mathbf{H}}_\mathbf{i} \in \mathcal{R}^3$ can be computed for all N rigid bodies according to

$$\dot{\mathbf{p}}_i = m_i\big(\dot{\mathbf{v}}_i + \ddot{\boldsymbol{\rho}}_{ci}\big)$$

$$\dot{\mathbf{H}}_i = \mathbf{I}_i\,\dot{\boldsymbol{\omega}}_i + \boldsymbol{\omega}_i \times \mathbf{I}_i\,\boldsymbol{\omega}_i$$

where $\ddot{\boldsymbol{\rho}}_{ci}$ is the second derivative of a position vector $\boldsymbol{\rho}_{ci}$ directed from $\mathbf{O}_i$ to the ith body center of mass (COM). The generalized force associated with u_j is

$$Q_j = \sum_{i=1}^{N}\left(\mathbf{F}_i \cdot \boldsymbol{\gamma}_{ij} + \mathbf{M}_i \cdot \boldsymbol{\beta}_{ij}\right) \tag{1}$$

and the general dynamic equation is used to obtain the equations of motion:

$$\sum_{i=1}^{N}\left[\dot{\mathbf{p}}_i \cdot \boldsymbol{\gamma}_{ij} + \big(\dot{\mathbf{H}}_i + m_i\boldsymbol{\rho}_{ci} \times \dot{\mathbf{v}}_i\big) \cdot \boldsymbol{\beta}_{ij}\right] = Q_j \quad (j = 1, \ldots, n-m). \tag{2}$$

3.2 Reaction Wheel Pendulum (RWP)

The RWP is an underactuated mechanical system composed of a pendulum linkage, motor actuator, and inertia wheel as illustrated in Figure 5. For this system of two rigid bodies, the ith rigid body has a reference point $\mathbf{O}_i$ fixed in the body, a scalar mass m_i, and an inertia dyadic

$$\mathbf{I}_i = \begin{bmatrix} I_{ix} & 0 & 0 \\ 0 & I_{iy} & 0 \\ 0 & 0 & I_{iz} \end{bmatrix}^T$$

about $\mathbf{O}_i$, where the off-diagonal elements are zero due to symmetry. The COM for each mass m_i is located a distance d_i away from the reference point in ground contact ($\mathbf{O}_1$). The applied forces acting on the ith body are equivalent to a force $\mathbf{F}_i = [F_{ix},\ F_{iy},\ F_{iz}]^T$ acting at $\mathbf{O}_i$ plus a moment $\mathbf{M}_i = [M_{ix},\ M_{iy},\ M_{iz}]^T$. The actuator generates a torque (τ) and experiences viscous friction (k_v) about reference point $\mathbf{O}_2$. Encoders are used to measure the angular displacement of the pendulum linkage away from the vertical position (θ_1) and the angular rotation of the inertia wheel (θ_2). The chosen quasi-velocities are

$$\mathbf{u} = [\dot{\theta}_1,\ \dot{\theta}_2]^T.$$

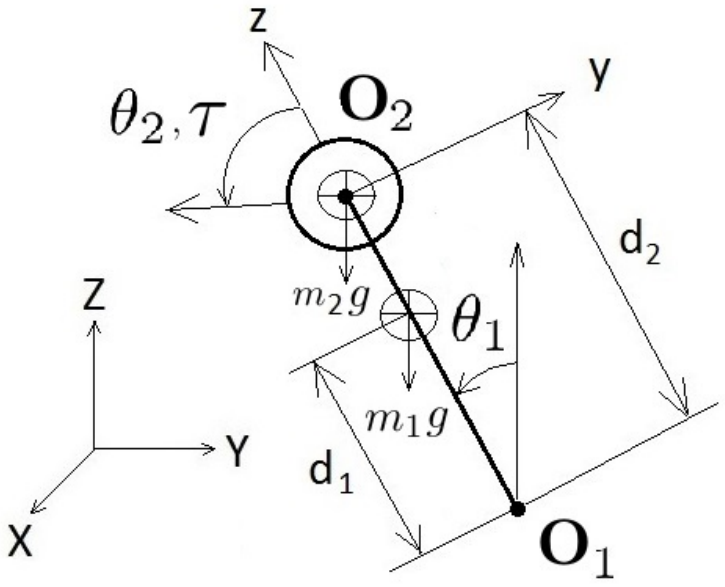

Figure 5: RWP variable and axes convention.

3.2.1 Pendulum Linkage

The reference point ($\mathbf{O}_1$) is chosen at the pendulum pivot in ground contact:

$$\boldsymbol{\rho}_{c_1} = [0,\ 0,\ d_1]^T$$

$$\dot{\boldsymbol{\rho}}_{c_1} = [0,\ -d_1\dot{\theta}_1,\ 0]^T$$

$$\ddot{\boldsymbol{\rho}}_{c_1} = [0,\ -d_1\ddot{\theta}_1,\ -d_1\dot{\theta}_1^2]^T.$$

The linear velocity and linear velocity coefficients about $\mathbf{O}_1$ are determined:

$$\mathbf{v}_1 = [0,\ 0,\ 0]^T$$

$$\boldsymbol{\gamma}_{11} = [0,\ 0,\ 0]^T$$

$$\boldsymbol{\gamma}_{12} = [0,\ 0,\ 0]^T.$$

The angular velocity and angular velocity coefficients about $\mathbf{O}_1$ are determined:

$$\boldsymbol{\omega}_1 = [\dot{\theta}_1,\ 0,\ 0]^T$$

$$\boldsymbol{\beta}_{11} = [1,\ 0,\ 0]^T$$

$$\boldsymbol{\beta}_{12} = [0,\ 0,\ 0]^T.$$

Derivatives of linear and angular velocity in the rotating frame are determined:

$$\dot{\mathbf{v}}_1 = [0,\ 0,\ 0]^T$$

$$\dot{\boldsymbol{\omega}}_1 = [\ddot{\theta}_1,\ 0,\ 0]^T.$$

Derivatives of linear and angular momentum are determined:

$$\dot{\mathbf{p}}_1 = m_1\dot{\mathbf{v}}_1$$

$$\dot{\mathbf{H}}_1 = [I_{1x}\ddot{\theta},\ 0,\ 0]^T$$

$$m_1\boldsymbol{\rho}_{c_1} \times \dot{\mathbf{v}}_1 = [0,\ 0,\ 0]^T.$$

3.2.2 Inertia Wheel

The reference point ($\mathbf{O}_2$) is chosen at the wheel center of mass:

$$\boldsymbol{\rho}_{c_2} = [0,\ 0,\ 0]^T$$

$$\dot{\boldsymbol{\rho}}_{c_2} = [0,\ 0,\ 0]^T$$

$$\ddot{\boldsymbol{\rho}}_{c_2} = [0,\ 0,\ 0]^T.$$

The linear velocity and linear velocity coefficients about $\mathbf{O}_2$ are determined:

$$\mathbf{v}_2 = [0,\ -d_2\dot{\theta}_1,\ 0]^T$$

$$\boldsymbol{\gamma}_{21} = [0,\ -d_2,\ 0]^T$$

$$\boldsymbol{\gamma}_{22} = [0,\ 0,\ 0]^T.$$

The angular velocity and angular velocity coefficients about $\mathbf{O}_2$ are determined:

$$\boldsymbol{\omega}_2 = [\dot{\theta}_1 + \dot{\theta}_2,\ 0,\ 0]^T$$

$$\boldsymbol{\beta}_{21} = [1,\ 0,\ 0]^T$$

$$\boldsymbol{\beta}_{22} = [1,\ 0,\ 0]^T.$$

Derivatives of linear and angular velocity in the rotating frame are determined:

$$\dot{\mathbf{v}}_2 = [0,\ -d_2\ddot{\theta}_1,\ -d_2(\dot{\theta}^2 + \dot{\theta}_1\dot{\theta}_2)]^T$$

$$\dot{\boldsymbol{\omega}}_2 = [\ddot{\theta}_1 + \ddot{\theta}_2,\ 0,\ 0]^T.$$

Derivatives of linear and angular momentum are determined:

$$\begin{aligned}\dot{\mathbf{p}}_2 &= m_2\dot{\mathbf{v}}_2 \\ \dot{\mathbf{H}}_2 &= [I_{2x}(\ddot{\theta}_1 + \ddot{\theta}_2),\ 0,\ 0]^T \\ m_2\boldsymbol{\rho}_{c_2} \times \dot{\mathbf{v}}_2 &= [0,\ 0,\ 0]^T.\end{aligned}$$

3.2.3 Generalized Forces

According to (1) the forces and torques that require consideration are determined:

$$\begin{aligned}Q_1 &= M_{1x} + M_{2x} - F_{2y}d_2 \\ Q_2 &= M_{2x}.\end{aligned}$$

By inspecting Figure 5, expressions for the relevant forces and moments are obtained:

$$\begin{aligned}F_{2y} &= -m_2 g \sin\theta_1 \\ M_{1x} &= -(\tau - k_v\dot{\theta}_2) + m_1 g d_1 \sin\theta_1 \\ M_{2x} &= \tau - k_v\dot{\theta}_2.\end{aligned}$$

3.2.4 Equations of Motion

The symbolic equations of motion are obtained with (2):

$$\begin{aligned}(m_2 d_2^2 + I_{1x} + I_{2x})\ddot{\theta}_1 + I_{2x}\ddot{\theta}_2 &= (m_1 d_1 + m_2 d_2) g \sin\theta_1 \\ I_{2x}\ddot{\theta}_2 + I_{2x}\ddot{\theta}_1 &= \tau - k_v\dot{\theta}_2.\end{aligned} \tag{3}$$

Upon substituting $I_{1x} = I_{1cm} + m_1 {d_1}^2$ and $I_{2x} = I_{2cm}$ (where $I_{i\,cm}$ is the moment of inertia of body i at the COM along the x-axis) the dynamics match RWP equations derived by Lagrange's method in previous work [25].

3.3 Two Wheeled Axle (TWA)

The TWA is a special mechanical system whose dynamics represent a special case of more difficult problems that follow. The TWA is composed of two motor actuators connected at opposite ends of an axle linkage (body 1) and two wheels in ground contact mounted on the actuator rotors (bodies 2 and 3), as illustrated in Figure 6. For this system of three rigid

bodies, the ith rigid body has a reference point $\mathbf{O}_i$ fixed in the body, a scalar mass m_i, and an inertia dyadic

$$\mathbf{I}_i = \begin{bmatrix} I_{ix} & 0 & 0 \\ 0 & I_{iy} & 0 \\ 0 & 0 & I_{iz} \end{bmatrix}^T$$

about $\mathbf{O}_i$, where the off-diagonal elements are zero due to symmetry. The linkage has mass m_1 and length L, and each wheel has a mass m_w and radius r. The applied forces acting on the ith body are equivalent to a force $\mathbf{F}_i = [F_{ix},\ F_{iy},\ F_{iz}]^T$ acting at $\mathbf{O}_i$ plus a moment $\mathbf{M}_i = [M_{ix},\ M_{iy},\ M_{iz}]^T$. The actuators generate torques (τ_R and τ_L) and experience viscous friction (k_v) about reference points $\mathbf{O}_2$ and $\mathbf{O}_3$. If physically constructed, encoders would be used to measure the angular displacement of each wheel (Θ_R and Θ_L); and both wheels are assumed to roll without slip. The chosen quasi-velocities are the linear velocity (v) and yaw rotation rate ($\dot{\phi}$)

$$\mathbf{u} = [v,\ \dot{\phi}]^T.$$

3.3.1 Axle Linkage

The reference point ($\mathbf{O}_1$) is chosen at the axle center of mass:

$$\boldsymbol{\rho}_{c_1} = \dot{\boldsymbol{\rho}}_{c_1} = \ddot{\boldsymbol{\rho}}_{c_1} = [0,\ 0,\ 0]^T.$$

The linear velocity and linear velocity coefficients about $\mathbf{O}_1$ are determined:

$$\mathbf{v}_1 = [0,\ v,\ 0]^T$$

$$\boldsymbol{\gamma}_{11} = [0,\ 1,\ 0]^T$$

$$\boldsymbol{\gamma}_{12} = [0,\ 0,\ 0]^T$$

$$\boldsymbol{\gamma}_{13} = [0,\ 0,\ 0]^T.$$

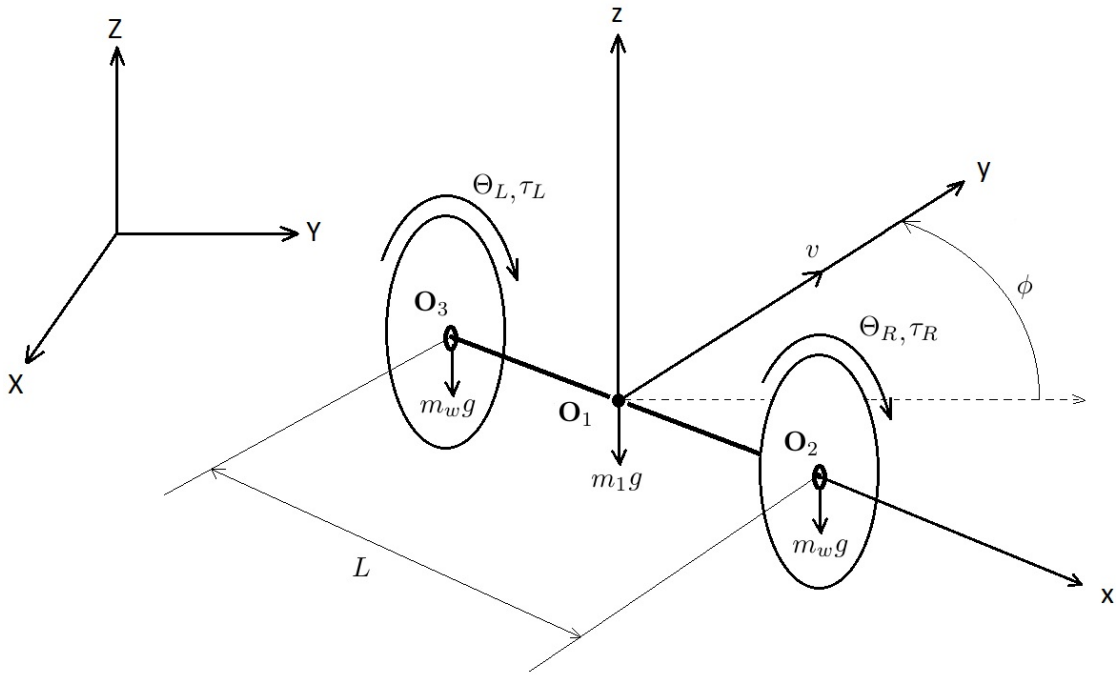

Figure 6: TWA variable and axes convention.

The angular velocity and angular velocity coefficients about $\mathbf{O}_1$ are determined:

$$\boldsymbol{\omega}_1 = [\dot{\theta},\ \dot{\phi}\sin\theta,\ \dot{\phi}\cos\theta]^T$$

$$\boldsymbol{\beta}_{11} = [0,\ 0,\ 0]^T$$

$$\boldsymbol{\beta}_{12} = [0,\ \sin\theta,\ \cos\theta]^T$$

$$\boldsymbol{\beta}_{13} = [1,\ 0,\ 0]^T.$$

Derivatives of linear and angular velocity in the rotating frame are determined:

$$\dot{\mathbf{v}}_1 = \begin{bmatrix} -\dot{\phi}v\cos\theta \\ \dot{v} \\ \dot{\theta}v. \end{bmatrix}$$

$$\dot{\boldsymbol{\omega}}_1 = \begin{bmatrix} \ddot{\theta} \\ \ddot{\phi}\sin\theta + \dot{\phi}\dot{\theta}\cos\theta \\ \ddot{\phi}\cos\theta - \dot{\phi}\dot{\theta}\sin\theta. \end{bmatrix}$$

Derivatives of linear and angular momentum are determined:

$$\dot{\mathbf{p}}_1 = m_1 \dot{\mathbf{v}}_1$$

$$\dot{\mathbf{H}}_1 = [0,\ 0,\ I_{1z}\ddot{\phi}]^T$$

$$m_1 \boldsymbol{\rho}_{c_1} \times \dot{\mathbf{v}}_1 = [0,\ 0,\ 0]^T.$$

3.3.2 Right Wheel

The reference point ($\mathbf{O}_2$) is chosen at the right wheel center of mass:

$$\boldsymbol{\rho}_{c_2} = \dot{\boldsymbol{\rho}}_{c_2} = \ddot{\boldsymbol{\rho}}_{c_2} = [0,\ 0,\ 0]^T.$$

The linear velocity and linear velocity coefficients about $\mathbf{O}_2$ are determined:

$$\mathbf{v}_2 = [\ 0,\ v + \frac{L}{2}\dot{\phi},\ 0]^T$$

$$\boldsymbol{\gamma}_{21} = [0,\ 1,\ 0]^T$$

$$\boldsymbol{\gamma}_{22} = [0,\ \frac{L}{2},\ 0]^T$$

$$\boldsymbol{\gamma}_{23} = [0,\ 0,\ 0]^T.$$

The angular velocity and angular velocity coefficients about $\mathbf{O}_2$ are determined:

$$\boldsymbol{\omega}_2 = [-\frac{v}{r} - \frac{L\dot{\phi}}{2r},\ 0,\ \dot{\phi}]^T$$

$$\boldsymbol{\beta}_{21} = [-\frac{1}{r},\ 0,\ 0]^T$$

$$\boldsymbol{\beta}_{22} = [-\frac{L}{2r},\ 0,\ 1]^T$$

$$\boldsymbol{\beta}_{23} = [0,\ 0,\ 0]^T.$$

Derivatives of linear and angular velocity in the rotating frame are determined:

$$\dot{\mathbf{v}}_2 = [-v\dot{\phi} - \frac{L}{2}\dot{\phi}^2,\ \dot{v} + \frac{L}{2}\ddot{\phi},\ -\frac{1}{r}(v + \frac{L}{2}\dot{\phi})^2]^T$$

$$\dot{\boldsymbol{\omega}}_2 = [-\frac{1}{r}(\dot{v} + \frac{L}{2}\ddot{\phi}),\ 0,\ \ddot{\phi}]^T.$$

Derivatives of linear and angular momentum are determined:

$$\dot{\mathbf{p}}_2 = m_2 \dot{\mathbf{v}}_2$$

$$\dot{\mathbf{H}}_2 = [-\frac{I_{2x}}{r}(\dot{v} + \frac{L}{2}\ddot{\phi}),\ -\frac{I_{2x} - I_{2z}}{r}(v\dot{\phi} + \frac{L}{2}\dot{\phi}^2),\ I_{2z}\ddot{\phi}\ ]^T$$

$$m_2 \boldsymbol{\rho}_{c_2} \times \dot{\mathbf{v}}_2 = [0,\ 0,\ 0]^T.$$

3.3.3 Left Wheel

The reference point ($\mathbf{O}_3$) is chosen at the left wheel center of mass:

$$\boldsymbol{\rho}_{c_3} = \dot{\boldsymbol{\rho}}_{c_3} = \ddot{\boldsymbol{\rho}}_{c_3} = [0,\ 0,\ 0]^T.$$

The linear velocity and linear velocity coefficients about $\mathbf{O}_3$ are determined:

$$\begin{aligned}
\mathbf{v}_3 &= [0,\ v - \frac{L}{2}\dot{\phi},\ 0]^T \\
\boldsymbol{\gamma}_{31} &= [0,\ 1,\ 0]^T \\
\boldsymbol{\gamma}_{32} &= [0,\ -\frac{L}{2},\ 0]^T \\
\boldsymbol{\gamma}_{33} &= [0,\ 0,\ 0]^T.
\end{aligned}$$

The angular velocity and angular velocity coefficients about $\mathbf{O}_3$ are determined:

$$\begin{aligned}
\boldsymbol{\omega}_3 &= [-\frac{v}{r} + \frac{L\dot{\phi}}{2r},\ 0,\ \dot{\phi}]^T \\
\boldsymbol{\beta}_{31} &= [-\frac{1}{r},\ 0,\ 0]^T \\
\boldsymbol{\beta}_{32} &= [\frac{L}{2r},\ 0,\ 1]^T \\
\boldsymbol{\beta}_{33} &= [0,\ 0,\ 0]^T.
\end{aligned}$$

Derivatives of linear and angular velocity in the rotating frame are determined:

$$\begin{aligned}
\dot{\mathbf{v}}_3 &= [-v\dot{\phi} + \frac{L}{2}\dot{\phi}^2,\ \dot{v} - \frac{L}{2}\ddot{\phi},\ -\frac{1}{r}(v - \frac{L}{2}\dot{\phi})^2]^T \\
\dot{\boldsymbol{\omega}}_3 &= [-\frac{1}{r}(\dot{v} - \frac{L}{2}\ddot{\phi}),\ 0,\ \ddot{\phi}]^T.
\end{aligned}$$

Derivatives of linear and angular momentum are determined:

$$\begin{aligned}
\dot{\mathbf{p}}_3 &= m_3\dot{\mathbf{v}}_3 \\
\dot{\mathbf{H}}_3 &= [-\frac{I_{3x}}{r}(\dot{v} - \frac{L}{2}\ddot{\phi}),\ -\frac{I_{3x} - I_{3z}}{r}(v\dot{\phi} - \frac{L}{2}\dot{\phi}^2),\ I_{3z}\ddot{\phi}]^T \\
m_3\boldsymbol{\rho}_{c_3} \times \dot{\mathbf{v}}_3 &= [0,\ 0,\ 0]^T.
\end{aligned}$$

3.3.4 Generalized Forces

According to (1) the forces and torques that require consideration are determined:

$$
\begin{aligned}
Q_1 &= F_{1y} + F_{2y} + F_{3y} - \frac{1}{r}(M_{2x} + M_{3x}) \\
Q_2 &= \frac{L}{2}(F_{2y} - F_{3y}) + M_{1z}\cos\theta + M_{1y}\sin\theta + M_{2z} + M_{3z} - \frac{L}{2r}(M_{2x} - M_{3x}) \\
Q_3 &= M_{1x}.
\end{aligned}
$$

By inspecting Figure 6, expressions for the relevant forces and torques are obtained:

$$
\begin{aligned}
F_{1y} &= F_{2y} = F_{3y} = 0 \\
M_{2x} &= -\tau_R + k_v\left(\frac{v}{r} + \frac{L}{2r}\dot{\phi}\right) \\
M_{3x} &= -\tau_L + k_v\left(\frac{v}{r} - \frac{L}{2r}\dot{\phi}\right) \\
M_{1x} &= -(M_{2x} + M_{3x}) \\
M_{1y} &= M_{1z} = M_{2z} = M_{3z} = 0.
\end{aligned}
$$

3.3.5 Equations of Motion

The symbolic equations of motion are obtained with (2)

$$
\begin{aligned}
\left(m_1 + 2m_w + \frac{2I_{wx}}{r^2}\right)\dot{v} &= \frac{1}{r}(\tau_R + \tau_L) - \frac{2k_v}{r^2}v \\
\left(I_{1_z} + 2I_{wz} + \frac{L^2}{2}(m_w + \frac{I_{wx}}{r^2})\right)\ddot{\phi} &= \frac{L}{2r}(\tau_R - \tau_L) - \frac{L^2 k_v}{2r^2}\dot{\phi} \\
I_{1x}\ddot{\theta} &= \tau_R + \tau_L - \frac{2k_v}{r}v
\end{aligned}
\tag{4}
$$

where $m_w = m_2 = m_3$ and $I_{wx} = I_{2x} = I_{3x}$.

3.4 Wheeled Inverted Pendulum (WIP)

The WIP is an underactuated mechanical system composed of two motor actuators connected at opposite ends of the pendulum/chassis (body 1) and two wheels in ground contact mounted on the actuator rotors (bodies 2 and 3), as illustrated in Figure 7. For this system of three rigid bodies, the ith rigid body has a reference point $\mathbf{O}_i$ fixed in the body, a scalar

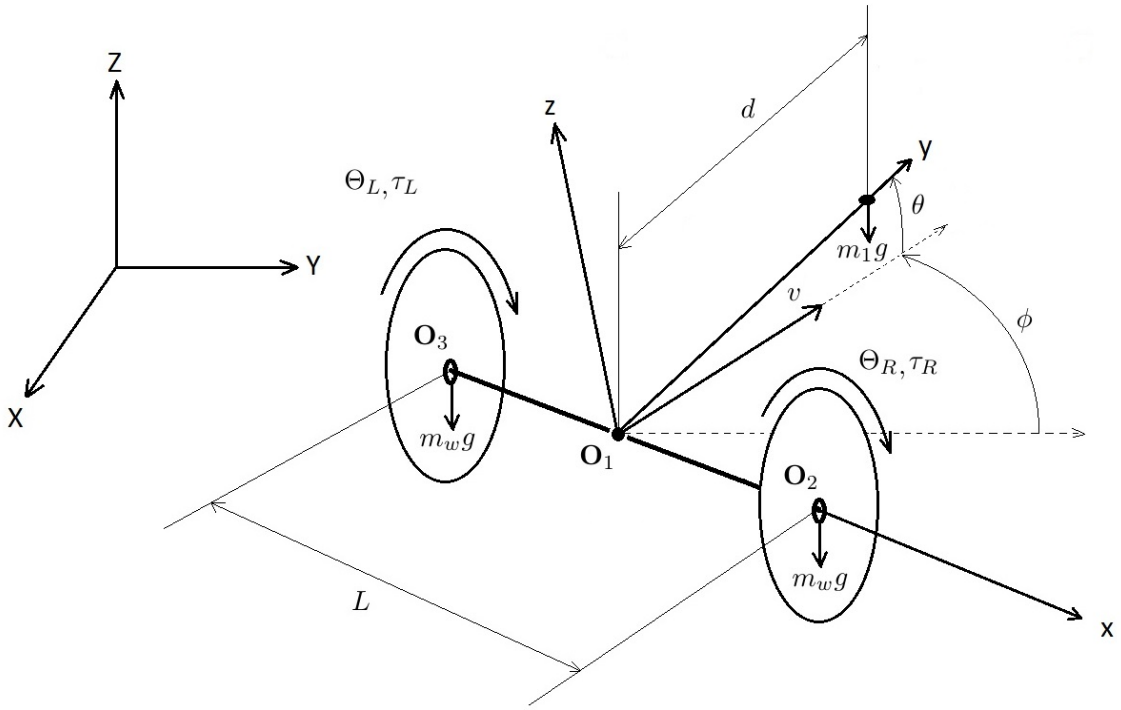

Figure 7: WIP variable and axes convention.

mass m_i, and an inertia dyadic

$$\mathbf{I}_i = \begin{bmatrix} I_{ix} & 0 & 0 \\ 0 & I_{iy} & 0 \\ 0 & 0 & I_{iz} \end{bmatrix}^T$$

about $\mathbf{O}_i$, where the off-diagonal elements are zero due to symmetry. The pendulum/chassis has mass m_1, length L and distance to COM d; and each wheel has a mass m_w and radius r. The applied forces acting on the ith body are equivalent to a force $\mathbf{F}_i = [F_{ix},\ F_{iy},\ F_{iz}]^T$ acting at $\mathbf{O}_i$ plus a moment $\mathbf{M}_i = [M_{ix},\ M_{iy},\ M_{iz}]^T$. The actuators generate torques (τ_R and τ_L) and experience viscous friction (k_v) about reference points $\mathbf{O}_2$ and $\mathbf{O}_3$. Encoders are used to measure the angular displacement of each wheel (Θ_R and Θ_L); and the drive wheels are assumed to roll without slip. The chosen quasi-velocities are the linear velocity (v), yaw rotation rate ($\dot{\phi}$), and pitch rotation rate ($\dot{\theta}$)

$$\mathbf{u} = [v,\ \dot{\phi},\ \dot{\theta}]^T.$$

3.4.1 Pendulum

The reference point ($\mathbf{O}_1$) is chosen at center between the wheels:

$$\boldsymbol{\rho}_{c_1} = [0,\ d,\ 0]^T$$
$$\dot{\boldsymbol{\rho}}_{c_1} = [-d\dot{\phi}\cos\theta,\ 0,\ d\dot{\theta}]^T$$
$$\ddot{\boldsymbol{\rho}}_{c_1} = [-d\big(\ddot{\phi}\cos(\theta) - 2\dot{\phi}\dot{\theta}\sin\theta\big),\ -d\big(\dot{\phi}^2\cos^2\theta + \dot{\theta}^2\big),\ d\big(\ddot{\theta} + \frac{1}{2}\sin(2\theta)\dot{\phi}^2\big)]^T.$$

The linear velocity and linear velocity coefficients about ($\mathbf{O}_1$) are determined:

$$\mathbf{v}_1 = [0,\ v\cos\theta,\ -v\sin\theta]^T$$
$$\boldsymbol{\gamma}_{11} = [0,\ \cos\theta,\ -\sin\theta]^T$$
$$\boldsymbol{\gamma}_{12} = [0,\ 0,\ 0]^T$$
$$\boldsymbol{\gamma}_{13} = [0,\ 0,\ 0]^T.$$

The angular velocity and angular velocity coefficients about ($\mathbf{O}_1$) are determined:

$$\boldsymbol{\omega}_1 = [\dot{\theta},\ \dot{\phi}\sin\theta,\ \dot{\phi}\cos\theta]^T$$
$$\boldsymbol{\beta}_{11} = [0,\ 0,\ 0]^T$$
$$\boldsymbol{\beta}_{12} = [0,\ \sin\theta,\ \cos\theta]^T$$
$$\boldsymbol{\beta}_{13} = [1,\ 0,\ 0]^T.$$

Derivatives of linear and angular velocity in the rotating frame are determined:

$$\dot{\mathbf{v}}_1 = [-v\dot{\phi},\ \dot{v}\cos\theta,\ -\dot{v}\sin\theta]^T$$
$$\dot{\boldsymbol{\omega}}_1 = [\ddot{\phi},\ \ddot{\phi}\sin\theta + \dot{\phi}\dot{\theta}\cos\theta,\ \ddot{\phi}\cos\theta - \dot{\phi}\dot{\theta}\sin\theta]^T.$$

Derivatives of linear and angular momentum are determined:

$$\dot{\mathbf{p}}_1 = m_1\dot{\mathbf{v}}_1$$
$$\dot{\mathbf{H}}_1 = \begin{bmatrix} I_{1x}\ddot{\theta} + (I_{1z} - I_{1y})\dot{\phi}^2\sin\theta\cos\theta \\ I_{1y}\ddot{\phi}\sin\theta + (I_{1y} + I_{1x} - I_{1z})\dot{\phi}\dot{\theta}\cos\theta \\ I_{1z}\ddot{\phi}\cos\theta + (I_{1y} - I_{1x} - I_{1z})\dot{\phi}\dot{\theta}\sin\theta \end{bmatrix}$$
$$m_1\boldsymbol{\rho}_{c_1} \times \dot{\mathbf{v}}_1 = [-dm_1\dot{v}\sin\theta,\ 0,\ dm_1\dot{\phi}v]^T.$$

3.4.2 Right Wheel

The reference point ($\mathbf{O}_2$) is chosen at the wheel center of mass:

$$\boldsymbol{\rho}_{c_2} = \dot{\boldsymbol{\rho}}_{c_2} = \ddot{\boldsymbol{\rho}}_{c_2} = [0,\ 0,\ 0]^T.$$

The linear velocity and linear velocity coefficients about $\mathbf{O}_2$ are determined:

$$\begin{aligned}
\mathbf{v}_2 &= [0,\ v + \frac{L}{2}\dot{\phi},\ 0]^T \\
\boldsymbol{\gamma}_{21} &= [0,\ 1,\ 0]^T \\
\boldsymbol{\gamma}_{22} &= [0,\ \frac{L}{2},\ 0]^T \\
\boldsymbol{\gamma}_{23} &= [0,\ 0,\ 0]^T.
\end{aligned}$$

The angular velocity and angular velocity coefficients about $\mathbf{O}_2$ are determined:

$$\begin{aligned}
\boldsymbol{\omega}_2 &= [-\frac{v}{r} - \frac{L\dot{\phi}}{2r},\ 0,\ \dot{\phi}]^T \\
\boldsymbol{\beta}_{21} &= [-\frac{1}{r},\ 0,\ 0]^T \\
\boldsymbol{\beta}_{22} &= [-\frac{L}{2r},\ 0,\ 1]^T \\
\boldsymbol{\beta}_{23} &= [0,\ 0,\ 0]^T.
\end{aligned}$$

Derivatives of linear and angular velocity in the rotating frame are determined:

$$\begin{aligned}
\dot{\mathbf{v}}_2 &= [-v\dot{\phi} - \frac{L}{2}\dot{\phi}^2,\ \dot{v} + \frac{L}{2}\ddot{\phi},\ -\frac{1}{r}(v + \frac{L}{2}\dot{\phi})^2]^T \\
\dot{\boldsymbol{\omega}}_2 &= [-\frac{1}{r}(\dot{v} + \frac{L}{2}\ddot{\phi}),\ 0,\ \ddot{\phi}]^T.
\end{aligned}$$

Derivatives of linear and angular momentum are determined:

$$\begin{aligned}
\dot{\mathbf{p}}_2 &= m_2\dot{\mathbf{v}}_2 \\
\dot{\mathbf{H}}_2 &= [-\frac{I_{2x}}{r}(\dot{v} + \frac{L}{2}\ddot{\phi}),\ -\frac{I_{2x} - I_{2z}}{r}(v\dot{\phi} + \frac{L}{2}\dot{\phi}^2),\ I_{2z}\ddot{\phi}]^T \\
m_2\boldsymbol{\rho}_{c_2} \times \dot{\mathbf{v}}_2 &= [0,\ 0,\ 0]^T.
\end{aligned}$$

3.4.3 Left Wheel

The reference point ($\mathbf{O}_3$) is chosen at the wheel center of mass:

$$\boldsymbol{\rho}_{c_3} = \dot{\boldsymbol{\rho}}_{c_3} = \ddot{\boldsymbol{\rho}}_{c_3} = [0,\ 0,\ 0]^T.$$

The linear velocity and linear velocity coefficients about $\mathbf{O}_3$ are determined:

$$\begin{aligned}
\mathbf{v}_3 &= [0,\ v - \frac{L}{2}\dot{\phi},\ 0]^T \\
\boldsymbol{\gamma}_{31} &= [0,\ 1,\ 0]^T \\
\boldsymbol{\gamma}_{32} &= [0,\ -\frac{L}{2},\ 0]^T \\
\boldsymbol{\gamma}_{33} &= [0,\ 0,\ 0]^T.
\end{aligned}$$

The angular velocity and angular velocity coefficients about $\mathbf{O}_3$ are determined:

$$\begin{aligned}
\boldsymbol{\omega}_3 &= [-\frac{v}{r} + \frac{L\dot{\phi}}{2r},\ 0,\ \dot{\phi}]^T \\
\boldsymbol{\beta}_{31} &= [-\frac{1}{r},\ 0,\ 0]^T \\
\boldsymbol{\beta}_{32} &= [\frac{L}{2r},\ 0,\ 1]^T \\
\boldsymbol{\beta}_{32} &= [0,\ 0,\ 0]^T.
\end{aligned}$$

Derivatives of linear and angular velocity in the rotating frame are determined:

$$\begin{aligned}
\dot{\mathbf{v}}_3 &= [-v\dot{\phi} + \frac{L}{2}\dot{\phi}^2,\ \dot{v} - \frac{L}{2}\ddot{\phi},\ -\frac{1}{r}(v - \frac{L}{2}\dot{\phi})^2]^T \\
\dot{\boldsymbol{\omega}}_3 &= [-\frac{1}{r}(\dot{v} - \frac{L}{2}\ddot{\phi}),\ 0,\ \ddot{\phi}]^T.
\end{aligned}$$

Derivatives of linear and angular momentum are determined:

$$\begin{aligned}
\dot{\mathbf{p}}_3 &= m_3\dot{\mathbf{v}}_3 \\
\dot{\mathbf{H}}_3 &= [-\frac{I_{3x}}{r}(\dot{v} - \frac{L}{2}\ddot{\phi}),\ -\frac{I_{3x} - I_{3z}}{r}(v\dot{\phi} - \frac{L}{2}\dot{\phi}^2),\ I_{3z}\ddot{\phi}]^T \\
m_3\boldsymbol{\rho}_{c_3} \times \dot{\mathbf{v}}_3 &= [0,\ 0,\ 0]^T.
\end{aligned}$$

3.4.4 Generalized Forces

According to (1) the forces and torques that require consideration are determined:

$$\begin{aligned}
Q_{u_1} &= F_{1y}\cos\theta - F_{1z}\sin\theta + F_{2y} + F_{3y} - \frac{1}{r}(M_{2x} + M_{3x}) \\
Q_{u_2} &= \frac{L}{2}(F_{2y} - F_{3y}) + M_{1y}\sin\theta + M_{1z}\cos\theta + M_{2z} + M_{3z} - \frac{L}{2r}(M_{2x} - M_{3x}) \\
Q_{u_3} &= M_{1x}.
\end{aligned}$$

By inspecting Figure 7, expressions for the relevant forces and torques are obtained:

$$
\begin{aligned}
F_{1y} &= F_{1z} = F_{2y} = F_{3y} = 0 \\
M_{1x} &= \tau_R + \tau_L - 2k_v\frac{v}{r} - m_1 g d\cos\theta \\
M_{2x} &= -\tau_R + k_v(\frac{v}{r} + \frac{L}{2r}\dot{\phi}) \\
M_{3x} &= -\tau_L + k_v(\frac{v}{r} - \frac{L}{2r}\dot{\phi}) \\
M_{1y} &= M_{1z} = M_{2z} = M_{3z} = 0.
\end{aligned}
$$

3.4.5 Equations of Motion

The symbolic equations of motion are obtained with (2)

$$
\begin{aligned}
\big(m_1 + 2m_w + \frac{2I_{wx}}{r^2}\big)\dot{v} - m_1 d\big(\cos\theta(\dot{\phi}^2 + \dot{\theta}^2) + \ddot{\theta}\sin\theta\big) &= \frac{1}{r}(\tau_R + \tau_L) - \frac{2k_v}{r^2}v \\
\ddot{\phi}\alpha + (I_{1y} - I_{1z})\dot{\phi}\dot{\theta}\sin(2\theta) + m_1 d\dot{\phi}v\cos\theta &= \frac{L}{2r}(\tau_R - \tau_L) - \frac{L^2 k_v}{2r^2}\dot{\phi} \\
I_{1x}\ddot{\theta} + \frac{I_{1z} - I_{1y}}{2}\dot{\phi}^2\sin(2\theta) - m_1 d\dot{v}\sin\theta &= \tau_R + \tau_L - \frac{2k_v}{r}v - dgm_1\cos\theta
\end{aligned}
\tag{5}
$$

where $m_w = m_2 = m_3$ and $I_{wx} = I_{2x} = I_{3x}$, and

$$
\alpha = I_{1y}\sin^2\theta + I_{1z}\cos^2\theta + 2I_{wz} + \frac{I_{wx}L^2}{2r^2} + \frac{m_w L^2}{2}.
$$

3.4.5.1 Special Case Validation: Two-Wheeled Axle

By assuming that the length to pendulum center of mass is at the axle ($d = 0$) and that inertias about the roll and yaw axes of body 1 are equal ($I_{yy} = I_{1z}$), the resulting equations of motion are identical to those found for the TWA in (4):

$$
\begin{aligned}
(m_1 + 3m_w)\dot{v} &= \frac{1}{r}(\tau_R + \tau_L) - \frac{2k_v}{r^2}v \\
\left(\frac{m_1 L^2}{12} + \frac{3m_w L^2}{4} + \frac{m_w r^2}{2}\right)\ddot{\phi} &= \frac{L}{2r}(\tau_R - \tau_L) - \frac{L^2 k_v}{2r^2}\dot{\phi} \\
I_{1x}\ddot{\theta} &= \tau_R + \tau_L - \frac{2k_v}{r}v
\end{aligned}
$$

3.4.5.2 Special Case Validation: Pendulum Linkage

If it is assumed that the wheels are massless, inertia-less, undriven, while the pendulum inertias are left generic, then the derived expressions degenerate into a problem solved

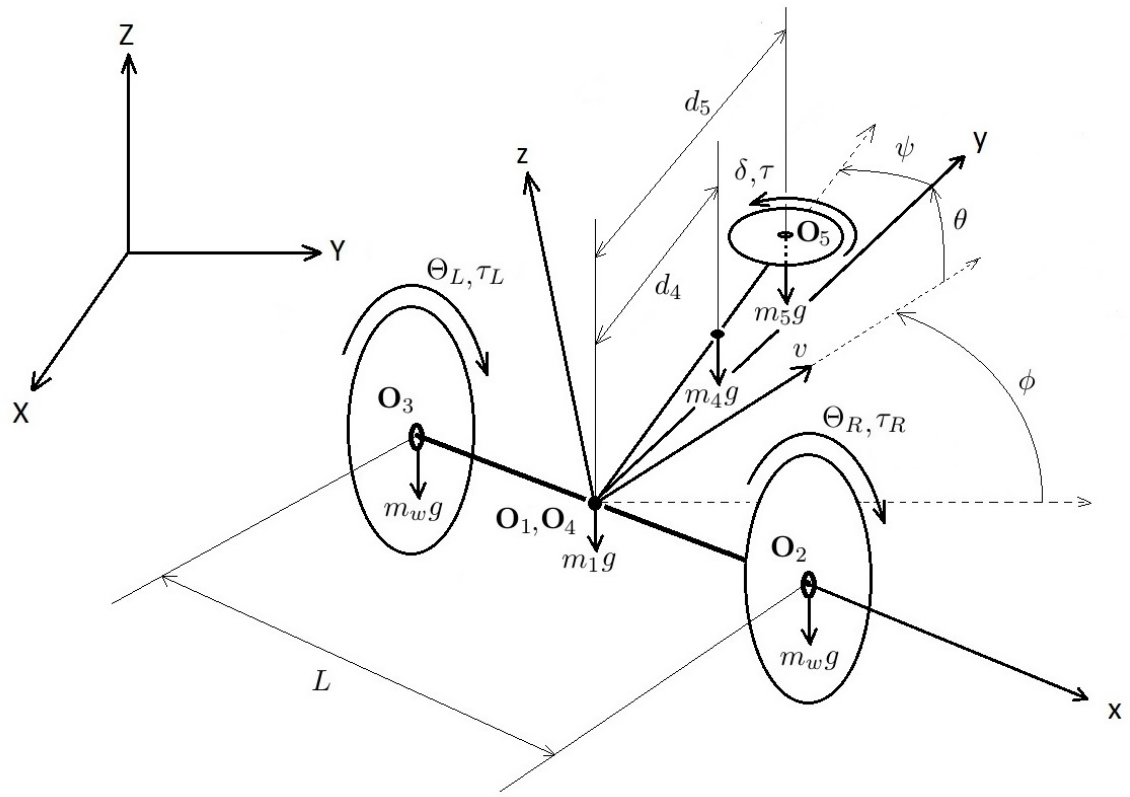

Figure 8: (Left) WBS prototype concept. (Right) WBS variable and axes convention.

in [82].

$$m_w = I_{wx} = I_{wz} = \tau_R = \tau_L = 0$$

The mechanical analysis text did not study the RHS terms, and the WIP is solved here with a slightly different axis convention; however, if the coordinate conventions were symbolically identical then the LHS dynamics would be an exact match:

$$m_1\dot{v} - m_1 d\big(\cos\theta(\dot{\phi}^2 + \dot{\theta}^2) + \ddot{\theta}\sin\theta\big) = 0$$

$$\big(I_{1z}\cos^2\theta + I_{1y}\sin^2\theta\big)\ddot{\phi} + (I_{1y} - I_{1z})\dot{\phi}\dot{\theta}\sin(2\theta) + m_1 d\dot{\phi}v\cos\theta = 0$$

$$I_{1x}\ddot{\theta} + \frac{I_{1z} - I_{1y}}{2}\dot{\phi}^2\sin(2\theta) - m_1 d\dot{v}\sin\theta = -m_1 g d\cos\theta$$

3.5 Wheeled Balance System (WBS)

The WBS is an underactuated mechanical system composed of an RWP (bodies 4 and 5) connected to the axle of a TWA (bodies 1,2 and 3), as illustrated in Figure 8. For this

system of five rigid bodies, the ith rigid body has a reference point $\mathbf{O}_i$ fixed in the body, a scalar mass m_i, and an inertia dyadic

$$\mathbf{I}_i = \begin{bmatrix} I_{ix} & 0 & 0 \\ 0 & I_{iy} & 0 \\ 0 & 0 & I_{iz} \end{bmatrix}^T$$

about $\mathbf{O}_i$, where the off-diagonal elements are zero due to symmetry. The chassis has mass m_1 and length L, each wheel has a mass m_w and radius r, the pendulum has mass m_4 and distance to COM d_4, and the inertia wheel has mass m_5 and distance to COM d_5. The applied forces acting on the ith body are equivalent to a force $\mathbf{F}_i = [F_{ix},\ F_{iy},\ F_{iz}]^T$ acting at $\mathbf{O}_i$ plus a moment $\mathbf{M}_i = [M_{ix},\ M_{iy},\ M_{iz}]^T$. The drive wheel actuators generate torques (τ_R and τ_L) and experience viscous friction (k_{vw}) about reference points $\mathbf{O}_2$ and $\mathbf{O}_3$. The inertia wheel actuator generates a torque (τ) and experiences viscous friction (k_{v5}) about reference point $\mathbf{O}_5$. Encoders are used to measure the angular displacement of each drive wheel (Θ_R and Θ_L) and the inertia wheel (δ); and the drive wheels are assumed to roll without slip. The chosen quasi-velocities are the chassis linear velocity (v), chassis yaw rotation rate ($\dot{\phi}$), chassis pitch rotation rate ($\dot{\theta}$), pendulum roll rate ($\dot{\psi}$), and inertia wheel angular velocity ($\dot{\delta}$)

$$\mathbf{u} = [v,\ \dot{\phi},\ \dot{\theta},\ \dot{\psi},\ \dot{\delta}]^T.$$

3.5.1 Axle Linkage

The reference point ($\mathbf{O}_1$) is chosen at the axle center of mass:

$$\boldsymbol{\rho}_{c_1} = \dot{\boldsymbol{\rho}}_{c_1} = \ddot{\boldsymbol{\rho}}_{c_1} = [0,\ 0,\ 0]^T.$$

The linear velocity and linear velocity coefficients about $\mathbf{O}_1$ are determined:

$$\mathbf{v}_1 = [0,\ v\cos\theta,\ -v\sin\theta]^T$$
$$\boldsymbol{\gamma}_{11} = [0,\ \cos\theta,\ -\sin\theta]^T$$
$$\boldsymbol{\gamma}_{12} = [0,\ 0,\ 0]^T$$
$$\boldsymbol{\gamma}_{13} = [0,\ 0,\ 0]^T$$
$$\boldsymbol{\gamma}_{14} = [0,\ 0,\ 0]^T$$
$$\boldsymbol{\gamma}_{15} = [0,\ 0,\ 0]^T.$$

The angular velocity and angular velocity coefficients about $\mathbf{O}_1$ are determined:

$$\boldsymbol{\omega}_1 = [\dot{\theta},\ \dot{\phi}\sin\theta,\ \dot{\phi}\cos\theta]^T$$
$$\boldsymbol{\beta}_{11} = [0,\ 0,\ 0]^T$$
$$\boldsymbol{\beta}_{12} = [0,\ \sin\theta,\ \cos\theta]^T$$
$$\boldsymbol{\beta}_{13} = [1,\ 0,\ 0]^T$$
$$\boldsymbol{\beta}_{14} = [0,\ 0,\ 0]^T$$
$$\boldsymbol{\beta}_{15} = [0,\ 0,\ 0]^T.$$

Derivatives of linear and angular velocity in the rotating frame are determined:

$$\dot{\mathbf{v}}_1 = [-v\dot{\phi},\ \dot{v}\cos\theta,\ -\dot{v}\sin\theta]^T$$
$$\dot{\boldsymbol{\omega}}_1 = [\ddot{\phi},\ \ddot{\phi}\sin\theta + \dot{\phi}\dot{\theta}\cos\theta,\ \ddot{\phi}\cos\theta - \dot{\phi}\dot{\theta}\sin\theta]^T.$$

Derivatives of linear and angular momentum are determined:

$$\dot{\mathbf{p}}_1 = m_1\dot{\mathbf{v}}_1$$
$$\dot{\mathbf{H}}_1 = \begin{bmatrix} I_{1x}\ddot{\theta} + (I_{1z} - I_{1y})\dot{\phi}^2\sin\theta\cos\theta \\ I_{1y}\ddot{\phi}\sin\theta + (I_{1y} + I_{1x} - I_{1z})\dot{\phi}\dot{\theta}\cos\theta \\ I_{1z}\ddot{\phi}\cos\theta + (I_{1y} - I_{1x} - I_{1z})\dot{\phi}\dot{\theta}\sin\theta \end{bmatrix}$$
$$m_1\boldsymbol{\rho}_{c_1} \times \dot{\mathbf{v}}_1 = [0,\ 0,\ 0]^T.$$

3.5.2 Right Wheel

The reference point ($\mathbf{O}_2$) is chosen at the wheel center of mass:

$$\boldsymbol{\rho}_{c_2} = \dot{\boldsymbol{\rho}}_{c_2} = \ddot{\boldsymbol{\rho}}_{c_2} = [0,\ 0,\ 0]^T.$$

The linear velocity and linear velocity coefficients about $\mathbf{O}_2$ are determined:

$$\begin{aligned}
\mathbf{v}_2 &= [0,\ v + \frac{L}{2}\dot{\phi},\ 0]^T \\
\boldsymbol{\gamma}_{21} &= [0,\ 1,\ 0]^T \\
\boldsymbol{\gamma}_{22} &= [0,\ \frac{L}{2},\ 0]^T \\
\boldsymbol{\gamma}_{23} &= [0,\ 0,\ 0]^T \\
\boldsymbol{\gamma}_{24} &= [0,\ 0,\ 0]^T \\
\boldsymbol{\gamma}_{25} &= [0,\ 0,\ 0]^T.
\end{aligned}$$

The angular velocity and angular velocity coefficients about $\mathbf{O}_2$ are determined:

$$\begin{aligned}
\boldsymbol{\omega}_2 &= [-\frac{v}{r} - \frac{L\dot{\phi}}{2r},\ 0,\ \dot{\phi}]^T \\
\boldsymbol{\beta}_{21} &= [-\frac{1}{r},\ 0,\ 0]^T \\
\boldsymbol{\beta}_{22} &= [-\frac{L}{2r},\ 0,\ 1]^T \\
\boldsymbol{\beta}_{23} &= [0,\ 0,\ 0]^T \\
\boldsymbol{\beta}_{24} &= [0,\ 0,\ 0]^T \\
\boldsymbol{\beta}_{25} &= [0,\ 0,\ 0]^T.
\end{aligned}$$

Derivatives of linear and angular velocity in the rotating frame are determined:

$$\begin{aligned}
\dot{\mathbf{v}}_2 &= [-v\dot{\phi} - \frac{L}{2}\dot{\phi}^2,\ \dot{v} + \frac{L}{2}\ddot{\phi},\ -\frac{1}{r}(v + \frac{L}{2}\dot{\phi})^2]^T \\
\dot{\boldsymbol{\omega}}_2 &= [-\frac{1}{r}(\dot{v} + \frac{L}{2}\ddot{\phi}),\ 0,\ \ddot{\phi}]^T.
\end{aligned}$$

Derivatives of linear and angular momentum are determined:

$$\begin{aligned}
\dot{\mathbf{p}}_2 &= m_2\dot{\mathbf{v}}_2 \\
\dot{\mathbf{H}}_2 &= [-\frac{I_{2x}}{r}(\dot{v} + \frac{L}{2}\ddot{\phi}),\ -\frac{I_{2x} - I_{2z}}{r}(v\dot{\phi} + \frac{L}{2}\dot{\phi}^2),\ I_{2z}\ddot{\phi}]^T \\
m_2\boldsymbol{\rho}_{c_2} \times \dot{\mathbf{v}}_2 &= [0,\ 0,\ 0]^T.
\end{aligned}$$

3.5.3 Left Wheel

The reference point ($\mathbf{O}_3$) is chosen at the wheel center of mass:

$$\boldsymbol{\rho}_{c_3} = \dot{\boldsymbol{\rho}}_{c_3} = \ddot{\boldsymbol{\rho}}_{c_3} = [0,\ 0,\ 0]^T.$$

The linear velocity and linear velocity coefficients about $\mathbf{O}_3$ are determined:

$$\begin{aligned}
\mathbf{v}_3 &= [0,\ v - \frac{L}{2}\dot{\phi},\ 0]^T \\
\boldsymbol{\gamma}_{31} &= [0,\ 1,\ 0]^T \\
\boldsymbol{\gamma}_{32} &= [0,\ -\frac{L}{2},\ 0]^T \\
\boldsymbol{\gamma}_{33} &= [0,\ 0,\ 0]^T \\
\boldsymbol{\gamma}_{34} &= [0,\ 0,\ 0]^T \\
\boldsymbol{\gamma}_{35} &= [0,\ 0,\ 0]^T.
\end{aligned}$$

The angular velocity and angular velocity coefficients about $\mathbf{O}_3$ are determined:

$$\begin{aligned}
\boldsymbol{\omega}_3 &= [-\frac{v}{r} + \frac{L\dot{\phi}}{2r},\ 0,\ \dot{\phi}]^T \\
\boldsymbol{\beta}_{31} &= [-\frac{1}{r},\ 0,\ 0]^T \\
\boldsymbol{\beta}_{32} &= [\frac{L}{2r},\ 0,\ 1]^T \\
\boldsymbol{\beta}_{32} &= [0,\ 0,\ 0]^T \\
\boldsymbol{\beta}_{34} &= [0,\ 0,\ 0]^T \\
\boldsymbol{\beta}_{35} &= [0,\ 0,\ 0]^T.
\end{aligned}$$

Derivatives of linear and angular velocity in the rotating frame are determined:

$$\begin{aligned}
\dot{\mathbf{v}}_3 &= [-v\dot{\phi} + \frac{L}{2}\dot{\phi}^2,\ \dot{v} - \frac{L}{2}\ddot{\phi},\ -\frac{1}{r}(v - \frac{L}{2}\dot{\phi})^2]^T \\
\dot{\boldsymbol{\omega}}_3 &= [-\frac{1}{r}(\dot{v} - \frac{L}{2}\ddot{\phi}),\ 0,\ \ddot{\phi}]^T.
\end{aligned}$$

Derivatives of linear and angular momentum are determined:

$$\begin{aligned}
\dot{\mathbf{p}}_3 &= m_3\dot{\mathbf{v}}_3 \\
\dot{\mathbf{H}}_3 &= [-\frac{I_{3x}}{r}(\dot{v} - \frac{L}{2}\ddot{\phi}),\ -\frac{I_{3x} - I_{3z}}{r}(v\dot{\phi} - \frac{L}{2}\dot{\phi}^2),\ I_{3z}\ddot{\phi}]^T \\
m_3\boldsymbol{\rho}_{c_3} \times \dot{\mathbf{v}}_3 &= [0,\ 0,\ 0]^T.
\end{aligned}$$

3.5.4 Pendulum Linkage

The reference point ($\mathbf{O}_4$) is chosen where the pendulum and axle linkages connect:

$$\begin{aligned}
\boldsymbol{\rho}_{c_4} &= [0,\ d_4,\ 0]^T \\
\dot{\boldsymbol{\rho}}_{c_4} &= \begin{bmatrix} -d_4\big(\dot{\psi} + \dot{\phi}\cos\theta\big) \\ 0 \\ d_4\dot{\theta} \end{bmatrix} \\
\ddot{\boldsymbol{\rho}}_{c_4} &= \begin{bmatrix} -d_4\big(\ddot{\psi} + \ddot{\phi}\cos\theta - 2\dot{\phi}\dot{\theta}\sin\theta\big) \\ -d_4\dot{\theta}^2 - d_4\big(\dot{\psi} + \dot{\phi}\cos\theta\big)^2 \\ d_4\ddot{\theta} + d_4\dot{\phi}\sin\theta\big(\dot{\psi} + \dot{\phi}\cos\theta\big) \end{bmatrix}.
\end{aligned}$$

The linear velocity and linear velocity coefficients about $\mathbf{O}_4$ are determined:

$$\begin{aligned}
\mathbf{v}_4 &= [0,\ v\cos\theta,\ -v\sin\theta]^T \\
\boldsymbol{\gamma}_{41} &= [0,\ \cos\theta,\ -\sin\theta]^T \\
\boldsymbol{\gamma}_{42} &= [0,\ 0,\ 0]^T \\
\boldsymbol{\gamma}_{43} &= [0,\ 0,\ 0]^T \\
\boldsymbol{\gamma}_{44} &= [0,\ 0,\ 0]^T \\
\boldsymbol{\gamma}_{45} &= [0,\ 0,\ 0]^T.
\end{aligned}$$

The angular velocity and angular velocity coefficients about $\mathbf{O}_4$ are determined:

$$\begin{aligned}
\boldsymbol{\omega}_4 &= [\dot{\theta},\ \dot{\phi}\sin\theta,\ \dot{\psi} + \dot{\phi}\cos\theta]^T \\
\boldsymbol{\beta}_{41} &= [0,\ 0,\ 0]^T \\
\boldsymbol{\beta}_{42} &= [0,\ \sin\theta,\ \cos\theta]^T \\
\boldsymbol{\beta}_{43} &= [1,\ 0,\ 0]^T \\
\boldsymbol{\beta}_{44} &= [0,\ 0,\ 1]^T \\
\boldsymbol{\beta}_{45} &= [0,\ 0,\ 0]^T.
\end{aligned}$$

Derivatives of linear and angular velocity in the rotating frame are determined:

$$\dot{\mathbf{v}}_4 = \begin{bmatrix} -v\big(\dot{\phi} + \dot{\psi}\cos\theta\big) \\ \dot{v}\cos\theta \\ -\dot{v}\sin\theta \end{bmatrix}$$

$$\dot{\boldsymbol{\omega}}_4 = \begin{bmatrix} \ddot{\theta} \\ \ddot{\phi}\sin\theta + \dot{\phi}\dot{\theta}\cos\theta \\ \ddot{\psi} + \ddot{\phi}\cos\theta - \dot{\phi}\dot{\theta}\sin\theta \end{bmatrix}.$$

Derivatives of linear and angular momentum are determined:

$$\dot{\mathbf{p}}_4 = m_4\dot{\mathbf{v}}_4$$

$$\dot{\mathbf{H}}_4 = \begin{bmatrix} I_{4x}\ddot{\theta} + (I_{4z} - I_{4y})\dot{\phi}\sin\theta\big(\dot{\psi} + \dot{\phi}\cos\theta\big) \\ I_{4y}\big(\ddot{\phi}\sin\theta + \dot{\phi}\dot{\theta}\cos\theta\big) + (I_{4x} - I_{4z})\dot{\theta}\big(\dot{\psi} + \dot{\phi}\cos\theta\big) \\ I_{4z}\big(\ddot{\psi} + \ddot{\phi}\cos\theta\big) + (I_{4y} - I_{4z} - I_{4x})\dot{\phi}\dot{\theta}\sin\theta \end{bmatrix}$$

$$m_4\boldsymbol{\rho}_{c_4} \times \dot{\mathbf{v}}_4 = \begin{bmatrix} -d_4 m_4 \dot{v}\sin\theta \\ 0 \\ d_4 m_4 v\big(\dot{\phi} + \dot{\psi}\cos\theta\big) \end{bmatrix}.$$

3.5.5 Inertia Wheel

The reference point ($\mathbf{O}_5$) is chosen at the inertia wheel center of mass:

$$\boldsymbol{\rho}_{c_5} = [0,\ 0,\ 0]^T$$

$$\dot{\boldsymbol{\rho}}_{c_5} = [0,\ 0,\ 0]^T$$

$$\ddot{\boldsymbol{\rho}}_{c_5} = [0,\ 0,\ 0]^T.$$

The linear velocity and linear velocity coefficients about $\mathbf{O}_5$ are determined:

$$\mathbf{v}_5 = \begin{bmatrix} -d_5\big(\dot{\psi} + \dot{\phi}\cos\theta\big) \\ v\cos\theta \\ d_5\dot{\theta} - v\sin\theta \end{bmatrix}$$

$$\boldsymbol{\gamma}_{51} = [0,\ \cos\theta,\ -\sin\theta]^T$$

$$\boldsymbol{\gamma}_{52} = [-d_5\cos\theta,\ 0,\ 0]^T$$

$$\boldsymbol{\gamma}_{53} = [0,\ 0,\ d_5]^T$$

$$\boldsymbol{\gamma}_{54} = [-d_5,\ 0,\ 0]^T$$

$$\boldsymbol{\gamma}_{55} = [0,\ 0,\ 0]^T.$$

The angular velocity and angular velocity coefficients about$\mathbf{O}_5$ are determined:

$$\boldsymbol{\omega}_5 = [\dot{\theta},\ \dot{\phi}\sin\theta,\ \dot{\delta} + \dot{\psi} + \dot{\phi}\cos\theta]^T$$

$$\boldsymbol{\beta}_{51} = [0,\ 0,\ 0]^T$$

$$\boldsymbol{\beta}_{52} = [0,\ \sin\theta,\ \cos\theta]^T$$

$$\boldsymbol{\beta}_{53} = [1,\ 0,\ 0]^T$$

$$\boldsymbol{\beta}_{54} = [0,\ 0,\ 1]^T$$

$$\boldsymbol{\beta}_{55} = [0,\ 0,\ 1]^T.$$

Derivatives of linear and angular velocity in the rotating frame are determined:

$$\dot{\mathbf{v}}_5 = \begin{bmatrix} 2d_5\dot{\phi}\dot{\theta}\sin\theta - \dot{\phi}v - d_5\ddot{\phi}\cos\theta - \dot{\delta}v\cos\theta - \dot{\psi}v\cos\theta - d_5\ddot{\psi} \\ -d_5\dot{\theta}^2 + \dot{v}\cos\theta - d_5(\dot{\psi} + \dot{\phi}\cos\theta)\big(\dot{\delta} + \dot{\psi} + \dot{\phi}\cos\theta\big) \\ d_5\ddot{\theta} - \dot{v}\sin\theta + d_5\dot{\phi}\sin\theta\big(\dot{\psi} + \dot{\phi}\cos\theta\big) \end{bmatrix}$$

$$\dot{\boldsymbol{\omega}}_5 = \begin{bmatrix} \ddot{\theta} \\ \ddot{\phi}\sin\theta + \dot{\phi}\dot{\theta}\cos\theta \\ \ddot{\delta} + \ddot{\psi} + \ddot{\phi}\cos\theta - \dot{\phi}\dot{\theta}\sin\theta \end{bmatrix}.$$

Derivatives of linear and angular momentum are determined:

$$\dot{\mathbf{p}}_5 = m_5\dot{\mathbf{v}}_5$$

$$\dot{\mathbf{H}}_5 = \begin{bmatrix} I_{5x}\ddot{\theta} + (I_{5z} - I_{5y})\dot{\phi}\sin\theta\big(\dot{\delta} + \dot{\psi} + \dot{\phi}\cos\theta\big) \\ I_{5y}\big(\ddot{\phi}\sin\theta + \dot{\phi}\dot{\theta}\cos\theta\big) + (I_{5x} - I_{5z})\dot{\theta}\big(\dot{\delta} + \dot{\psi} + \dot{\phi}\cos\theta\big) \\ I_{5z}\big(\ddot{\delta} + \ddot{\psi} + \ddot{\phi}\cos\theta\big) + (I_{5y} - I_{5z} - I_{5x})\dot{\phi}\dot{\theta}\sin\theta \end{bmatrix}$$

$$m_5\boldsymbol{\rho}_{c_5} \times \dot{\mathbf{v}}_5 = [0,\ 0,\ 0]^T.$$

3.5.6 Generalized Forces

According to (1) the forces and torques that require consideration are determined:

$$Q_{u_1} = F_{2y} + F_{3y} + (F_{1y} + F_{4y} + F_{5y})\cos\theta - (F_{1z} + F_{4z} + F_{5z})\sin\theta - (M_{2x} + M_{3x})\frac{1}{r}$$

$$Q_{u_2} = M_{2z} + M_{3z} + (M_{1z} + M_{4z} + M_{5z})\cos\theta + (M_{1y} + M_{4y} + M_{5y})\sin\theta - (M_{2x} - M_{3x})\frac{L}{2r}$$
$$+ (F_{2y} - F_{3y})\frac{L}{2} - F_{5x}d_5\cos\theta$$

$$Q_{u_3} = M_{1x} + M_{4x} + M_{5x} + F_{5z}d_5$$

$$Q_{u_4} = M_{4z} + M_{5z} - F_{5x}d_5$$

$$Q_{u_5} = M_{5z}.$$

By inspecting Figure 8, expressions for the relevant forces and torques are obtained:

$$F_{1y} = F_{1z} = F_{2y} = F_{3y} = F_{4y} = F_{4z} = F_{5y} = F_{5z} = 0$$

$$M_{1y} = M_{1z} = M_{2z} = M_{3z} = M_{4x} = M_{4y} = M_{5x} = M_{5y} = 0$$

$$M_{1x} = \tau_L + \tau_R - \frac{2k_{v_w}}{r}v - (d_4m_4 + d_5m_5)g\cos\theta\cos\psi$$

$$M_{2x} = -\tau_R + k_{vw}\Big(\frac{v}{r} + \frac{L}{2r}\dot{\phi}\Big)$$

$$M_{3x} = -\tau_L + k_{vw}\Big(\frac{v}{r} - \frac{L}{2r}\dot{\phi}\Big)$$

$$M_{4z} = -(\tau - k_{v5}\dot{\delta}) + m_4gd_4\sin\theta\sin\psi$$

$$M_{5z} = \tau - k_{v5}\dot{\delta}$$

$$F_{5x} = -m_5g\sin\theta\sin\psi.$$

3.5.7 Equations of Motion

The general dynamic equation is used to obtain generic equations of motion; however, a concise representation of the result cannot be conveyed using typeset (due to complexity) and the interested reader may consult Appendix A to see lengthly dynamic relationships. During WBS simulations, a function containing the symbolic derivation is called and evaluated to update the model states. The WBS model is highly nonlinear, and dynamic models of the RWP, TWA, and WIP, are all special cases of this derivation. In general, the WBS dynamics can be compactly written

$$\dot{z} = f(z, u).$$

3.5.7.1 Special Case Validation: RWP

The WBS dynamic model reduces to that found for the RWP by not permitting the pendulum to rotate along the pitch or yaw axes

$$\theta = \frac{\pi}{2}, \quad \dot{\theta} = 0, \quad \dot{\phi} = 0$$

which results in

$$I_{5z}\ddot{\delta} + \ddot{\psi}(m_5 d_5^2 + I_{4z} + I_{5z}) = (d_4 m_4 + d_5 m_5) g \sin\psi$$
$$I_{5z}\ddot{\delta} + I_{5z}\ddot{\psi} = \tau - \dot{\delta} k_{v5}.$$

and by substituting in $I_{4z} = I_{4\text{com}} + m_4 d_4^2$ this results in an exact match to (3).

3.5.7.2 Special Case Validation: TWA

The WBS dynamic model reduces to that found for the TWA by removing the masses of bodies 4 and 5, and setting inertias of body 1 about the roll and yaw axes equal,

$$m_4 = m_5 = 0, \quad I_{4i} = I_{5i} = 0, \quad I_{1y} = I_{1z}$$

which yields

$$\left(m_1 + 2m_w + \frac{2I_{wx}}{r^2}\right)\dot{v} = \frac{1}{r}(\tau_R + \tau_L) - \frac{2k_{vw}}{r^2} v$$
$$\left(I_{1z} + 2I_{wz} + \frac{L^2}{2}\left(m_w + \frac{I_{wx}}{r^2}\right)\right)\ddot{\phi} = \frac{L}{2r}(\tau_R - \tau_L) - \frac{L^2 k_{vw}}{2r^2}\dot{\phi}$$
$$I_{1x}\ddot{\theta} = \tau_L + \tau_R - \frac{2k_{vw}}{r} v$$

where $m_w = m_2 = m_3$ and $I_{wx} = I_{2x} = I_{3x}$, and this results in an exact match to (4).

3.5.7.3 Special Case Validation: WIP

The WBS dynamic model reduces to that found for the WIP by removing the mass of body 5, and by letting body 4 represent one rigid combination of axle and pendulum linkages

$$m_1 = m_5 = 0, \quad I_{1i} = I_{5i} = 0, \quad \psi = \dot{\psi} = \ddot{\psi} = 0$$

which results in

$$\begin{aligned}
\big(m_4 + 2m_w + \frac{2I_{wx}}{r^2}\big)\dot{v} - m_4 d_4\big(\cos\theta(\dot{\phi}^2 + \dot{\theta}^2) + \ddot{\theta}\sin\theta\big) &= \frac{1}{r}(\tau_R + \tau_L) - \frac{2k_{vw}}{r^2}v \\
\ddot{\phi}\alpha + (I_{4y} - I_{4z})\dot{\phi}\dot{\theta}\sin(2\theta) + m_4 d_4 \dot{\phi} v\cos\theta &= \frac{L}{2r}(\tau_R - \tau_L) - \frac{L^2 k_{vw}}{2r^2}\dot{\phi} \\
I_{4x}\ddot{\theta} + \frac{I_{4z} - I_{4y}}{2}\dot{\phi}^2\sin(2\theta) - m_4 d_4 \dot{v}\sin\theta &= \tau_L + \tau_R - \frac{2k_{vw}}{r}v - m_4 d_4 g\cos\theta
\end{aligned}$$

where $m_w = m_2 = m_3$ and $I_{wx} = I_{2x} = I_{3x}$ and

$$\alpha = I_{4y}\sin^2\theta + I_{4z}\cos^2\theta + 2I_{wz} + \frac{I_{wx}L^2}{2r^2} + \frac{m_w L^2}{2}$$

which results in an exact match to (5).

CHAPTER IV

IDENTIFICATION

To accurately simulate plant physics, every effort must be made to identify all system parameters, imperfections, and operating limits. This chapter goes through a sequence of topics that includes computing moments of inertia, followed by a discussion about sensor resolution issues, and concludes by deriving feasible actuator operating limits. Actuator imperfections such as cogging torque, gearbox backlash, Coulomb friction, and Stribeck friction are all modeled based on measurements of the hardware intended for implementation. As a result of following the procedures in this chapter, a high-fidelity simulation study can be conducted that accurately predicts the success or failure of a particular controller design without risking hardware damage.

4.1 Inertia Calculations

To provide parameter values for the dynamics derived in Chapter 3 only a few specific moments of inertia require computation. For each rigid body, the specific inertias we require knowledge of are found about a reference point where that individual body rotates. Inertia tables are consulted to provide known expressions for basic shapes, and more complicated expressions are derived using the parallel-axis theorem. In the case of composite bodies, the final step is to sum multiple collocated contributions (perhaps also involving the parallel-axis theorem) about a specified axis.

4.1.1 RWP Pendulum and Wheel

The RWP is composed of a composite pendulum body and a composite inertia wheel. The pendulum body consists of a linkage arm connected to the motor stator. The wheel body is composed of two cylindrical disks (one smaller for mounting purposes) and includes the motor rotor. The simplified RWP construction diagram and the actual prototype are shown in Figure 9.

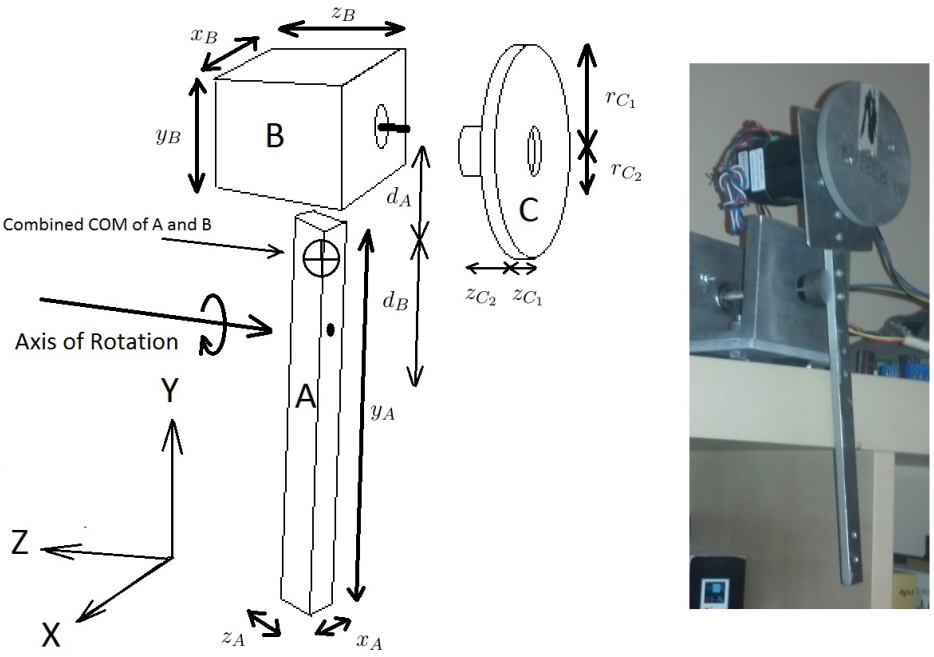

Figure 9: RWP construction diagram and physical implementation.

The pendulum COM ($\mathbf{p}$) is computed using the scaled masses of bodies A (m_A) and B (m_B) and the measured lengths of both bodies along the y-axis (y_A and y_B),

$$y_{\text{com}} = \frac{m_A \frac{y_A}{2} + m_B(y_A + \frac{y_B}{2})}{m_A + m_B}$$

$$\mathbf{p} = (0,\ y_{\text{com}},\ 0)$$

where x_{com} and z_{com} are zero due to symmetry. The moments of inertia about the pendulum COM ($I_{p_{\text{com}}}$) are found by taking the summation of contributions from bodies A and B (I_{Ap} and I_{Bp}) along the z-axis through $\mathbf{p}$ resulting in

$$I_{A_p} = \frac{1}{12} m_A (x_A^2 + y_A^2) + m_A d_A^2$$

$$I_{B_p} = \frac{1}{12} m_B (x_B^2 + y_B^2) + m_B d_B^2$$

$$I_{p_{\text{com}}} = I_{A_p} + I_{B_p}$$

where d_A and d_B are the distances from the COMs of bodies A and B to $\mathbf{p}$.

The inertia wheel sub-masses m_{C_1} and m_{C_2} are determined by weighing their combined mass (body C), assuming uniform density, and distributing the assigned masses proportional to each volume. The volumes of each sub-body are determined by measuring each radius

Table 1: RWP Parameters and Inertias

Parameter	Value	Units
m_A	0.114	kg
x_A	13.0×10^{-3}	m
y_A	255.0×10^{-3}	m
z_A	6.70×10^{-3}	m
d_A	122.0×10^{-3}	m
m_B	0.520	kg
x_B	42.0×10^{-3}	m
y_B	42.0×10^{-3}	m
z_B	60.0×10^{-3}	m
d_B	26.7×10^{-3}	m
m_{C_1}	0.128	kg
r_{C_1}	47.5×10^{-3}	m
z_{C_1}	7.0×10^{-3}	m
m_{C_2}	0.062	kg
r_{C_2}	20.0×10^{-3}	m
z_{C_2}	19.0×10^{-3}	m
$I_{p_{\text{com}}}$	2.80×10^{-3}	$\text{kg} \cdot \text{m}^2$
$I_{r_{\text{com}}}$	0.155×10^{-3}	$\text{kg} \cdot \text{m}^2$
l_p	63.3×10^{-3}	m
l_r	90.0×10^{-3}	m
I_p	5.40×10^{-3}	$\text{kg} \cdot \text{m}^2$

(r_{C_1}, r_{C_2}) and thickness (z_{C_1}, z_{C_2}) of composite body C. The moment of inertia about the actuator rotor ($I_{r_{\text{com}}}$) is computed by summing the inertias of each sub-body resulting in

$$I_{r_{\text{com}}} = \frac{1}{2}(m_{C_1} r_{C_1}^2 + m_{C_2} r_{C_2}^2)$$

where C_1 refers to the larger inertia disk and C_2 refers to the smaller mounting disk.

To complete the parameterization of the equations of motion in §3.2, l_p is the distance from the pendulum COM to the pivot, and l_r is the distance from body C to the pivot. The pendulum inertia about the pivot is determined according to

$$I_p = I_{p_{\text{com}}} + (m_A + m_B) l_p^2 \tag{6}$$

and Table 1 lists all RWP physical measurements and computed inertias.

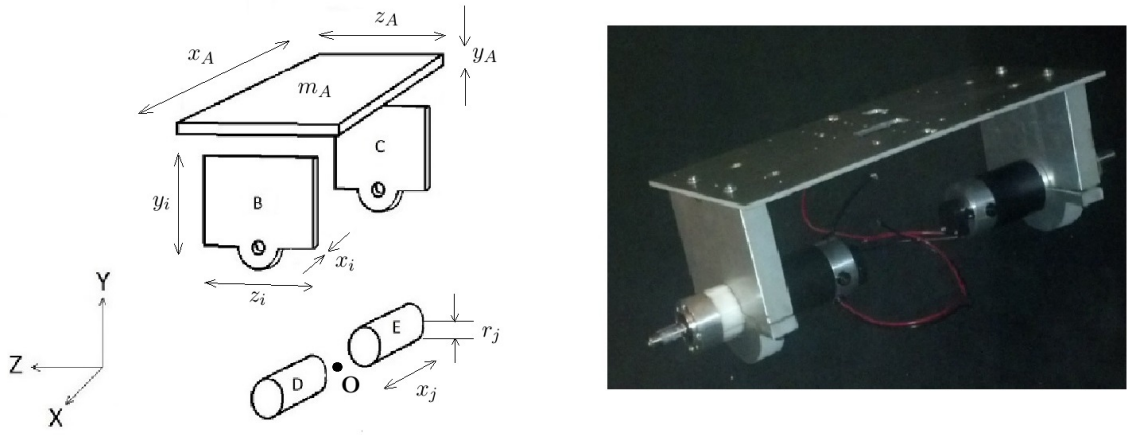

Figure 10: Actual chassis body for the WIP.

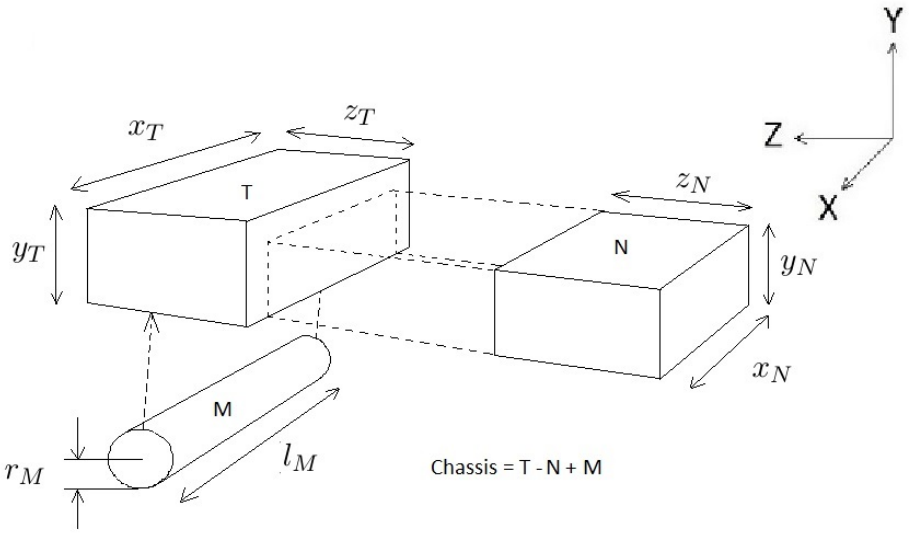

Figure 11: Approximate chassis body for the WIP.

4.1.2 WIP Chassis and Wheels

The WIP chassis is a composite body consisting of three slabs of aluminum, two motor stators, and the entire body rotates about point O as implied in Figure 10. The inertia calculations are simplified by approximately representing the chassis as a composite body composed of three basic solid aluminum shapes. These simplified shapes are one large solid aluminum rectangle of positive mass (body T), one smaller solid aluminum rectangle of negative mass (body N), and one solid aluminum cylinder of positive mass (body M) as depicted in Figure 11. The dimensions of bodies T, N, and M are

$$(x_T,\, y_T,\, z_T\,) = (x_A,\, y_A + y_i,\, z_A\,)$$

$$(x_N,\, y_N,\, z_N\,) = (x_A - 2x_i,\, y_i,\, z_A\,)$$

$$(l_M,\, r_M) = (x_A,\, r_j)$$

where $i \in [\,B,\, C\,]$ and $j \in [\,D,\, E\,]$.

To determine the chassis COM $(x_{\text{COM}}, y_{\text{COM}}, z_{\text{COM}})$, first the COMs for each approximate body are defined by inspecting Figure 11

$$T_{\text{com}} = \left(0,\ \frac{y_T}{2},\ 0\right), \quad N_{\text{com}} = \left(0,\ \frac{y_N}{2},\ 0\right) \quad M_{\text{com}} = \left(0,\ 0,\ 0\right)$$

then the y-component values are substituted into

$$y_{\text{com}} = \frac{m_T T_{\text{com}_y} - m_N N_{\text{com}_y} + m_M M_{\text{com}_y}}{m_T - m_N + m_M} \tag{7}$$

and since the body rotates about point **O**, x_{com} and z_{com} are zero by symmetry. The chassis inertias (I_{cx}, I_{cy}, I_{cz}) are determined by computing the inertias for each approximate body (I_{kx}, I_{ky}, I_{kz} with $k \in [\,T,\, N,\, M\,]$) and summing the individual contributions about each axis of rotation through point **O**.

The chassis inertia about the x-axis through **O** is:

$$\begin{aligned}
I_{Tx} &= \frac{1}{12} m_T (z_T^2 + y_T^2) + m_T (y_T - y_{\text{com}})^2 \\
I_{Nx} &= \frac{1}{12} m_N (z_N^2 + y_N^2) + m_N (y_N - y_{\text{com}})^2 \\
I_{Mx} &= m_M r_M^2 + m_M y_{\text{com}}^2 \\
I_{cx} &= I_{Tx} - I_{Nx} + I_{Mx}.
\end{aligned}$$

The chassis inertia about the y-axis through **O** is:

$$\begin{aligned}
I_{Ty} &= \frac{1}{12} m_T (x_T^2 + z_T^2) \\
I_{Ny} &= \frac{1}{12} m_N (x_N^2 + z_N^2) \\
I_{My} &= \frac{1}{4} m_M r_M^2 + \frac{1}{12} m_M l_M^2 \\
I_{cy} &= I_{Ty} - I_{Ny} + I_{My}.
\end{aligned}$$

Table 2: WIP Parameters and Inertias

	Parameter	Value	Units
Body A	m_A	1.250	kg
	x_A	405.0×10^{-3}	m
	y_A	5.0×10^{-3}	m
	z_A	250.0×10^{-3}	m
Body $i \in [\,B, C\,]$	m_i	1.346	kg
	x_i	25.6×10^{-3}	m
	y_i	124.0×10^{-3}	m
	z_i	152.0×10^{-3}	m
Body $j \in [\,D, E\,]$	m_j	1.484	kg
	l_j	170.0×10^{-3}	m
	r_j	57.4×10^{-3}	m
Chassis	I_{cx}	49.6×10^{-3}	$\mathrm{kg} \cdot \mathrm{m}^2$
	I_{cy}	192.5×10^{-3}	$\mathrm{kg} \cdot \mathrm{m}^2$
	I_{cz}	213.8×10^{-3}	$\mathrm{kg} \cdot \mathrm{m}^2$

The chassis inertia about the z-axis through **O** is

$$
\begin{aligned}
I_{Tz} &= \frac{1}{12} m_T (y_T^2 + x_T^2) + m_T (y_{\mathrm{com}} - \frac{1}{2} y_T)^2 \\
I_{Nz} &= \frac{1}{12} m_N (y_N^2 + x_N^2) + m_N (y_{\mathrm{com}} - \frac{1}{2} y_N)^2 \\
I_{Mz} &= \frac{1}{4} m_M r_M^2 + \frac{1}{12} m_M l_M^2 \\
I_{cz} &= I_{Tz} - I_{Nz} + I_{Mz}.
\end{aligned}
$$

Table 2 lists all WIP chassis measurements and computed inertias.

The left and right wheels are identical and are approximated by a solid plastic cylinder. The reference point is chosen at the wheel center of mass as indicated in Figure 12 and the inertias are computed according to

$$
\begin{aligned}
I_{wx} &= \frac{1}{2} m_w r_w^2 \\
I_{wy} &= \frac{1}{4} m_w r_w^2 + \frac{1}{12} m_w x_w^2 \\
I_{wz} &= \frac{1}{4} m_w r_w^2 + \frac{1}{12} m_w x_w^2
\end{aligned}
$$

where r_w is the wheel radius, and x_w is the wheel thickness. Table 3 provides the wheel measurements and computed inertias.

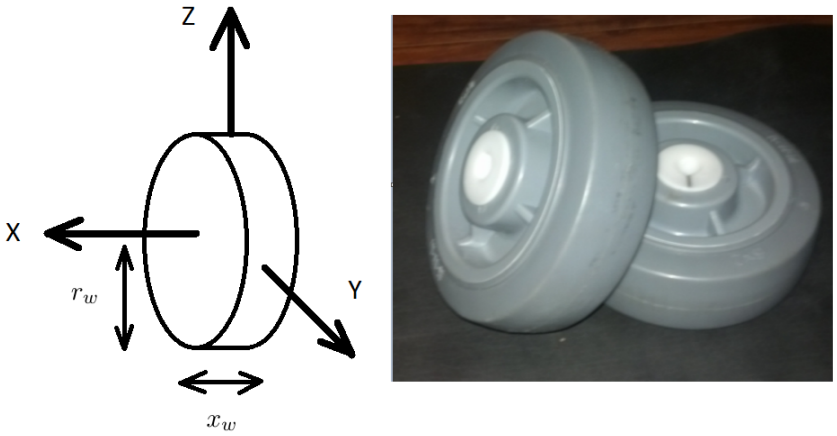

Figure 12: (Left) Wheel axis convention. (Right) Wheels used to drive the WIP/WBS.

Table 3: Wheel Parameters and Inertias

Parameter	Value	Units
m_w	0.544	kg
x_w	50.0×10^{-3}	m
r_w	75.0×10^{-3}	m
I_{wx}	1.5×10^{-3}	$\text{kg} \cdot \text{m}^2$
I_{wy}	0.878×10^{-3}	$\text{kg} \cdot \text{m}^2$
I_{wz}	0.878×10^{-3}	$\text{kg} \cdot \text{m}^2$

4.1.3 Ideal WBS Prototype

It is future work to construct the WBS apparatus and to experimentally implement control over it; however, the relevant parameters for the ideal prototype are derived so as to predict the controlled performance as an outcome of the simulation study in §5.3. The ideal WBS is composed of five rigid bodies: one axle linkage, two wheels, one pendulum linkage, and one inertia payload as illustrated in Figure 13. The WBS rigid members rotate about reference points $\mathbf{O}_1$-$\mathbf{O}_5$ matching the convention used in Figure 8 to derive the equations of motion in §3.5. The inertias for each rigid member are determined using the measured masses and lengths previously listed in Tables 1, 2, and 3.

The axle linkage (body 1) is a composite body consisting of two motor stators separated by a cylindrical space where the pendulum linkage is mounted, and a solid cylinder

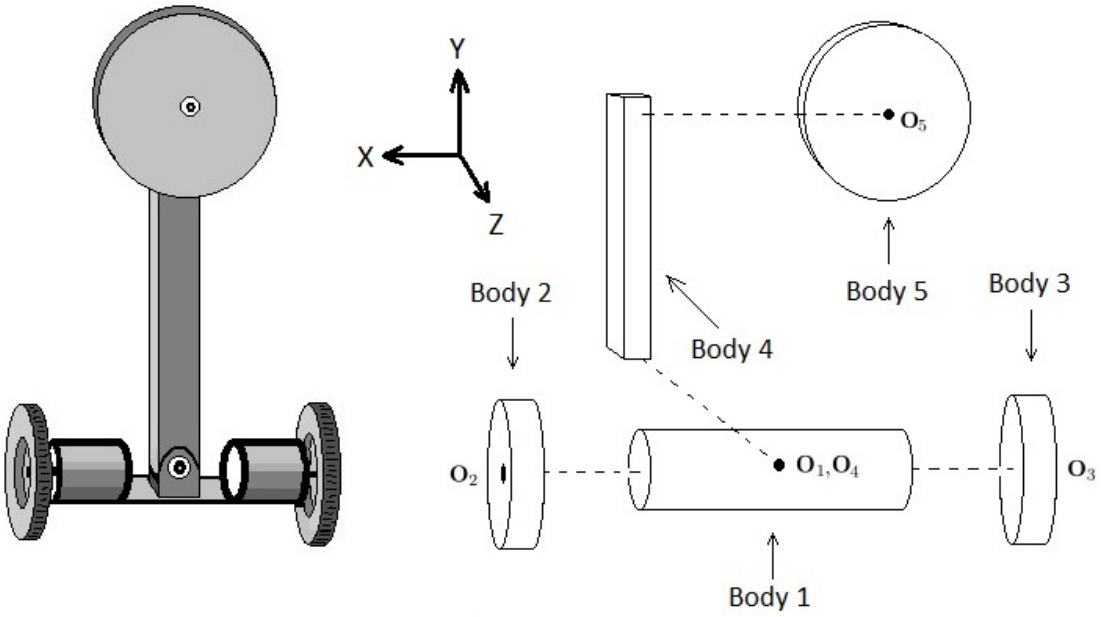

Figure 13: (Left) ideal WBS concept, (Right) approximate WBS construction.

approximately represents it. Body 1 rotates about $\mathbf{O}_1$, and the inertias are computed by

$$
\begin{aligned}
I_{1x} &= m_1 r_1^2 \\
I_{1y} &= \frac{1}{4} m_1 r_1^2 + \frac{1}{12} m_1 l_1^2 \\
I_{1z} &= \frac{1}{4} m_1 r_1^2 + \frac{1}{12} m_1 l_1^2
\end{aligned}
$$

where Table 2 is consulted to assign $m_1 = 2m_j$, $r_1 = r_j$, and $l_1 = x_A$. The inertias for both wheels (bodies 2 and 3) have been computed in previous work and are reported in Table 3.

The pendulum linkage (body 4) rotates about $\mathbf{O}_4$, and the inertias are computed by

$$
\begin{aligned}
I_{4x} &= \frac{1}{12} m_A (y_A^2 + z_A^2) + m_A d_A^2 + \frac{1}{12} m_B (y_B^2 + z_B^2) + m_B d_B^2 + (m_A + m_B) y_{\text{com}}^2 \\
I_{4y} &= \frac{1}{12} m_A (z_A^2 + x_A^2) + \frac{1}{12} m_B (z_B^2 + x_B^2) \\
I_{4z} &= \frac{1}{12} m_A (x_A^2 + y_A^2) + m_A d_A^2 + \frac{1}{12} m_B (x_B^2 + y_B^2) + m_B d_B^2 + (m_A + m_B) y_{\text{com}}^2
\end{aligned}
$$

where Table 1 is consulted to assign values to all parameters here except for y_{com} which is computed in (7).

The inertia wheel (body 5) is approximated by one solid cylindrical disk of mass $m_5 = m_{C_1} + m_{C_2}$, radius $r_5 = r_{C_1}$, and thickness $h_5 = z_{C_1}$; where Table 1 is consulted to assign

Table 4: WBS Parameters and Inertias

Body	Parameter	Value	Units
Chassis	I_{cx}	16.4×10^{-3}	$\mathrm{kg} \cdot \mathrm{m}^2$
	I_{cy}	25.5×10^{-3}	$\mathrm{kg} \cdot \mathrm{m}^2$
	I_{cz}	25.5×10^{-3}	$\mathrm{kg} \cdot \mathrm{m}^2$
Drive Wheels	Extracted from Table 3		
Pendulum Linkage	I_{px}	5.40×10^{-3}	$\mathrm{kg} \cdot \mathrm{m}^2$
	I_{py}	0.235×10^{-3}	$\mathrm{kg} \cdot \mathrm{m}^2$
	I_{pz}	5.50×10^{-3}	$\mathrm{kg} \cdot \mathrm{m}^2$
Inertia Wheel	I_{rx}	0.108×10^{-3}	$\mathrm{kg} \cdot \mathrm{m}^2$
	I_{ry}	0.108×10^{-3}	$\mathrm{kg} \cdot \mathrm{m}^2$
	I_{rz}	0.214×10^{-3}	$\mathrm{kg} \cdot \mathrm{m}^2$

values to the m_5, r_5, and h_5 parameters. Body 5 rotates about $\mathbf{O}_5$, and the inertias are computed according to

$$I_{5x} = \frac{1}{12} m_5 (3r_5^2 + h_5^2)$$
$$I_{5y} = \frac{1}{12} m_5 (3r_5^2 + h_5^2)$$
$$I_{5z} = \frac{1}{2} m_5 r_5^2.$$

Table 4 provides a list of the computed WBS inertias.

4.2 Quantization Effects

Quantization is a nonlinearity that affects the representation accuracy of a signal. Resolution is the physical limit that describes how accurately a sensor or actuation device can measure or impose some signal. Given a sensor or actuation resolution Q then the quantization effect on variable x is simulated by

$$x_{\text{eff}} = Q \ \text{round}\left(\frac{x_{\text{act}}}{Q}\right).$$

The quantization resolutions are typically fixed parameters once implementation begins; however, during the initialization of an embedded program, some of these values can be chosen or altered. The chosen AC and DC motors have position encoders with identical and fixed resolutions known before embedded code execution. A 12-bit ADC processes

Table 5: Implemented Quantization Resolutions

Device	Affected Quantity	Symbol	Value	Units
Encoder	Angular Position	Q_p	1.6×10^{-3}	rad/bit
ADC	Motor Current	Q_i	4.0×10^{-3}	A/bit
PWM	AC Voltage	Q_{ac}	16.0×10^{-3}	V/bit
	DC Voltage	Q_{dc}	48.0×10^{-3}	V/bit
Gyroscope	Angular Velocity	Q_v	532.6×10^{-6}	$\frac{\text{rad}}{\text{s}}$/bit
Accelerometer	Linear Acceleration	Q_a	598.1×10^{-6}	$\frac{\text{m}}{\text{s}^2}$ /bit

current measurements over a range of values determined either by circuit analysis of the hardware schematic or by the calibration procedure described in §4.3. The implemented gyroscope and accelerometer can each be programmed to hold one of four values representing full-scale internal deflection. Motor actuation is a programmable variable but cannot be chosen arbitrarily small. AC motor actuation is finer than DC motor actuation by a factor of two so as to identify the motor nonlinearities described in §4.4.4.2 and §4.4.4.4 with high-fidelity. The quantization resolutions, symbols, and values listed in Table 5 represent the hardware resolutions implemented throughout this project.

Describing function (DF) theory can be used to predict the effects of quantization. The quantization DF is

$$N(A) = \begin{cases} 0, & A < \delta_1 \\ \frac{4Q}{\pi A} \sum_{i=1}^{n} \sqrt{1 - \left(\frac{\delta_i}{A}\right)^2}, & A > \delta_n \end{cases}$$

and

$$\delta_i = Q\left(\frac{1}{2} + k\right), \quad k \in [0, \infty),$$

where Q is the quantization resolution, k is an integer, and $N(A)$ represents the effective gain of quantization as a function of the signal amplitude (A) processed by the quantizing device. In Figure 14, a family of effective gains for several resolutions are shown, and there are two important observations to make. First, for large values of A, quantization has little effect and the DF gain approaches unity. Second, the DF kernel represents a region

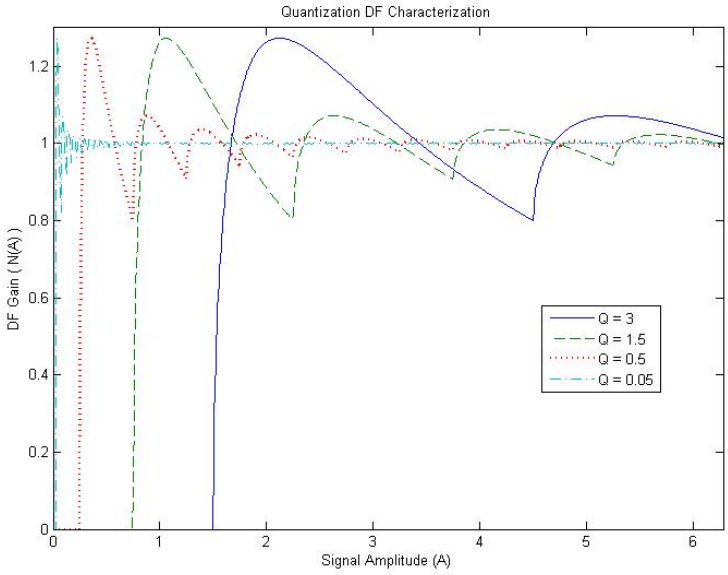

Figure 14: A family of quantization DFs representing the effective signal gain.

either where sensors are not detecting a change in variable state, or where an actuator is unresponsive to feedback law updates. The null space region is one source of limit-cycling behavior and will shrink for smaller quantization resolutions; however, simply implementing a smaller quantization resolution will not eliminate the existence of a limit-cycle.

4.2.1 PWM Actuation

Pulse-width modulation (PWM) is a popular technique used to generate voltages for motor actuation. Typical PWM implementation involves bipolar switching of logic levels at a specified operating frequency (f_{pwm}) to create the gating signals that manipulate power transistors on an H-bridge circuit. By changing the duty ratio, converter output voltages can be manipulated, and a simple calculation is used to predict the average leg voltage,

$$\bar{v}_{\text{leg}}[k] = \int_{kT}^{kT+T} v(t)\ dt = d[k]\ V_{\text{dc}}$$

which means that the duty cycle that must be imposed to obtain this leg voltage is

$$d[k] = \frac{\bar{v}_{\text{leg}}[k]}{V_{\text{dc}}}, \quad \bar{v}_{\text{leg}}[k] \in [0,\ V_{\text{dc}}].$$

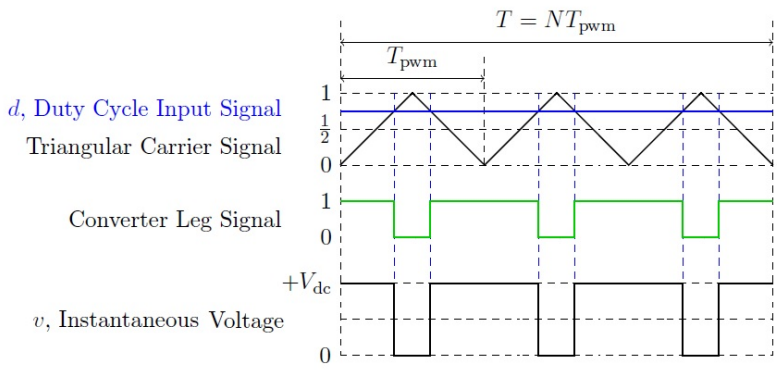

Figure 15: PWM leg voltages are generated by amplifying gating signals.

The number of realizable voltages is

$$N_v = \frac{\Delta V}{Q},$$

where ΔV is the full range of voltages to be represented and Q is the implemented actuator resolution. The triangular carrier signal seen in Figure 15 counts from zero to N_v and back to zero at a specified system clock frequency (f_{sys}) to generate f_{pwm}.

4.2.2 Current Measurements

The ADC module is only capable of interpreting voltages that are sensed on the input pin to a sample and hold circuit. Since we are interested in measuring (potentially very large) currents, the motor currents must be processed through a current to voltage converter. Shunt resistors that have a very small ohmic value and are placed in series with each half-bridge leg to drop relatively small voltages that represent the current flowing during motor operation. As currents flow through these shunt resistors, the differential op-amp circuit shown in Figure 16 is designed to shift and amplify the voltage to a safe level that can be applied to the ADC sample and hold circuit (vpin). The figure only shows one bridge leg; however, two legs (for a DC motor) or three legs (for an AC motor) are required to have a meaningful discussion about instantaneous motor currents. The circuit is designed to transform currents in the range $i \in [-16.4\text{A},\ 16.4\text{A}]$ into voltages in the range $v_{\text{pin}} \in [0\text{V},\ 3.3\text{V}]$, and the implemented quantization for this circuit is listed in Table 5.

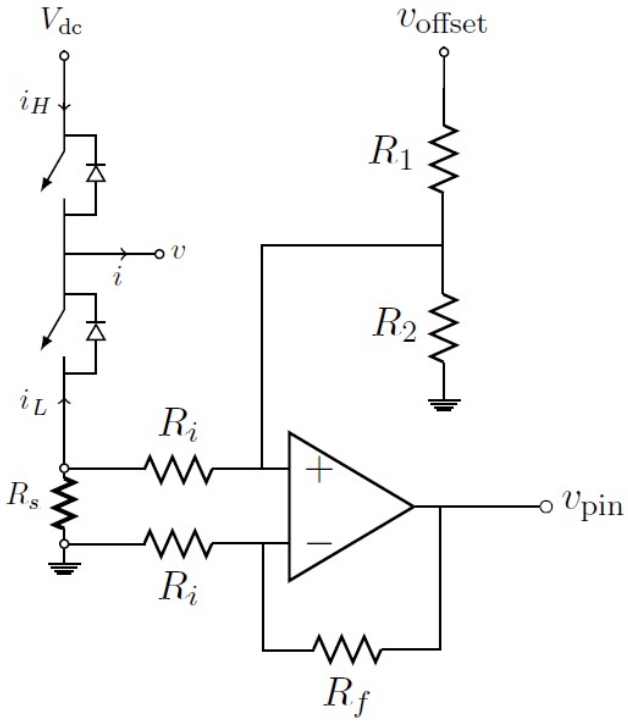

Figure 16: A half-bridge leg with sense resistor and differential op-amp circuit.

4.2.3 Inertial Sensing

An inertial sensor is a device that uses the inertia of an internally moving element to perform a measurement of the motion being experienced by the system. There are two main types of inertial sensors: gyroscopes and accelerometers. Inertial sensors with internal moving parts are called inertial micro-electromechanical systems (inertial MEMS). The implemented inertial sensing circuitry is designed to operate along the I^2C serial bus and possesses a few programmable features such as clocking rates, digital filtering, self-testing, and sensor resolution options. The accelerometer and gyroscope were experimented with at each sensor resolution to determine which full-scale deflection options did not saturate the sensor and still had an acceptable zero-bias. Table 6 lists all programmable gyroscope and accelerometer sensor resolutions, and Table 5 includes the implemented sensor resolutions.

Table 6: Gyroscope and Accelerometer Resolution Options

Device	Register Value	Resolution	Unit
Gyroscope (Address 0x1B)	0	133.2×10^{-6}	$\frac{\text{rad}}{\text{s}}$/bit
	1	266.3×10^{-6}	
	2	532.6×10^{-6}	
	3	1.065×10^{-3}	
Accelerometer (Address 0x1C)	0	598.8×10^{-6}	$\frac{\text{m}}{\text{s}^2}$ /bit
	1	1.198×10^{-3}	
	2	2.395×10^{-3}	
	3	4.790×10^{-3}	

4.2.4 Position Encoder

A quadrature encoder is mounted on each axis of rotation to measure all angular positions. The optoelectronic assembly permits light to pass through small slits that are spaced a specific distance apart. As the shaft rotates, the light detection outputs will change state due to the lines on the disc periodically interfering with the light directed from the emitters. An encoder with N-many lines on the disk will resolve $4N$ possible angular positions over one full revolution. A circuit internal to the encoder decodes the motion information into a counter register that keeps track of the traversed angular position. The implemented motor encoder resolutions are listed in Table 5, and Figure 17 shows an exaggerated demonstration of the encoder quantization effect.

4.3 ADC Calibration

The current sensing calibration applies mainly to the AC and DC motor friction identification experiments as discussed in §4.4.4.2 and §4.5.4.1 respectively. The calibration of the current sensing system on each converter leg is somewhat involved, since the measurement of each converter leg current involves a shunt resistor, an op-amp circuit and an analog-to-digital converter; each of these components introduces its own imperfection that, if not properly accounted for, will lead to inaccurate current measurements and hence inaccurate modeling of electromagnetic torque.

Converter leg currents are measured by sampling the voltage drops across low-resistance

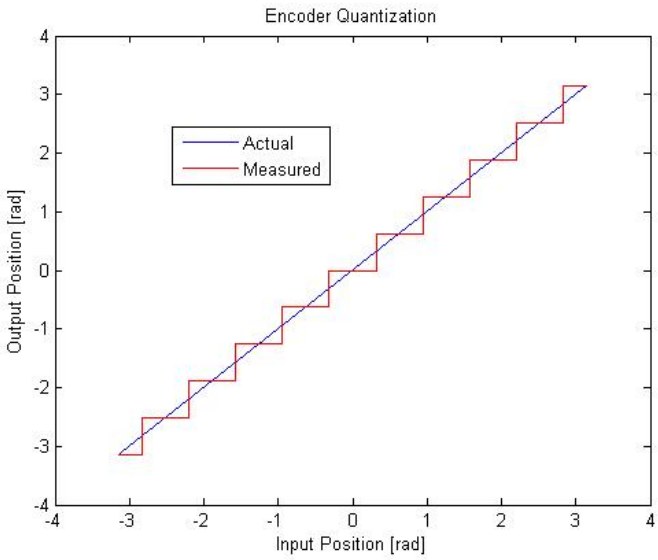

Figure 17: Exaggerated quantization effect.

shunt resistors located between the low-side switch of each leg and ground. Since current may flow in either direction through the shunt resistor, its voltage drop may be positive or negative. An op-amp circuit is necessary to perform scaling and shifting of the shunt resistor voltage, so that the microcontroller pin voltage remains between 0 V and 3.3 V.

On the highest level, the current sensing system for leg A may be characterized by

$$i_A = \alpha_A \cdot \mathtt{A} + \beta_A$$

where `A` is the 12-bit unsigned integer generated by the analog-to-digital converter, and where α_A are β_A are constant real-valued coefficients having units of A. Assuming nothing more than linearity, the op-amp circuit can be expected to satisfy an affine relationship of the form

$$i_A = \alpha_{A1} v_{\text{pin}} + \beta_{A1}$$

and the analog-to-digital converter circuit can be expected to satisfy the affine relationship

$$v_{\text{pin}} = \alpha_{A2} \mathtt{A} + \beta_{A2}.$$

Combining these results yields another overall affine relationship of the form

$$i_A = (\alpha_{A1}\alpha_{A2})\,\mathtt{A} + (\beta_{A1} + \alpha_{A1}\beta_{A2})\,.$$

If it is possible to force known values of current to flow, then the resulting data pairs $(i_A, \mathtt{A})$ may be used to determine the unknown gain and offset parameters using least-squares data fitting. In particular, if data pairs $(i_A[n], \mathtt{A}[n])$ for $n = 1, 2, 3, \ldots$ are obtained experimentally, then

$$\begin{bmatrix} \mathtt{A}[1] & 1 \\ \mathtt{A}[2] & 1 \\ \mathtt{A}[3] & 1 \\ \vdots & \vdots \end{bmatrix} \begin{bmatrix} \alpha_A \\ \beta_A \end{bmatrix} = \begin{bmatrix} i_A[1] \\ i_A[2] \\ i_A[3] \\ \vdots \end{bmatrix}$$

represents an overdetermined system of linear algebraic equations involving the two unknown variables α_A and β_A. The normal form of this system of equations is obtained by multiplying both sides by the transpose of the coefficient matrix, resulting in

$$\begin{bmatrix} A_1 & A_2 \\ A_2 & N \end{bmatrix} \begin{bmatrix} \alpha_A \\ \beta_A \end{bmatrix} = \begin{bmatrix} b_1 \\ b_2 \end{bmatrix}$$

where

$$A_1 = \sum_{n=1}^{N} \mathtt{A}[n]^2, \quad A_2 = \sum_{n=1}^{N} \mathtt{A}[n], \quad b_1 = \sum_{n=1}^{N} \mathtt{A}[n] i_A[n], \quad b_2 = \sum_{n=1}^{N} i_A[n].$$

The explicit solution to the 2×2 normal form equations is therefore

$$\begin{bmatrix} \alpha_A \\ \beta_A \end{bmatrix} = \frac{1}{NA_1 - A_2^2} \begin{bmatrix} Nb_1 - A_2 b_2 \\ A_1 b_2 - A_2 b_1 \end{bmatrix}.$$

Current sensing calibration parameters for converter legs B and C may be similarly obtained.

4.4 AC Motor Characterization

The AC motor is characterized to provide a simulation model that can accurately predict controller performance in the presence of various imperfections. The torque vs. speed capability of the AC machine is developed from an analysis of the motor dynamics, converter operating limits, and data sheet values. Procedures for identifying the parameters of characteristics such as cogging torque and higher-order friction effects are developed, implemented,

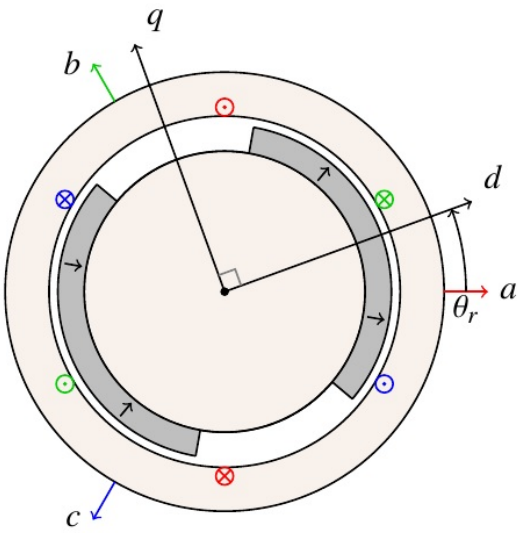

Figure 18: PM synchronous motor magnetics.

and validated. Information obtained from the torque vs. speed capability analysis indicates what the actuator saturation limits are, and this data can be incorporated during control design to implement integrator anti-windup.

4.4.1 Motor Dynamics

The cross section view of the three-phase motor is depicted in Figure 18, for the case of $N_r = 1$ rotor pole pair, so as to reveal its magnetic geometry. The phase voltages and phase currents may be transformed into the rotor reference frame according to

$$\begin{aligned} \star_d &= \sqrt{\tfrac{2}{3}}\left(\star_a \cos\vartheta_a + \star_b \cos\vartheta_b + \star_c \cos\vartheta_c\right) \\ \star_q &= -\sqrt{\tfrac{2}{3}}\left(\star_a \sin\vartheta_a + \star_b \sin\vartheta_b + \star_c \sin\vartheta_c\right) \\ \star_0 &= \sqrt{\tfrac{1}{3}}\left(\star_a + \star_b + \star_c\right) \end{aligned} \tag{8}$$

where $\star$ stands for v or i and

$$\begin{aligned} \vartheta_a &= N_r\theta_r \\ \vartheta_b &= N_r\theta_r - \tfrac{2\pi}{3} \\ \vartheta_c &= N_r\theta_r + \tfrac{2\pi}{3}. \end{aligned} \tag{9}$$

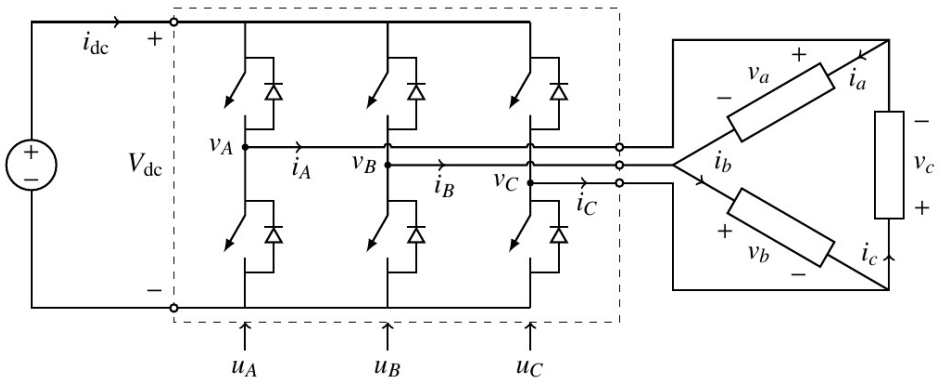

Figure 19: PM synchronous motor drive system.

Using rotor frame variables to represent ac behavior in terms of equivalent dc behavior, the electromagnetic torque is

$$\tau = \Lambda_r N_r i_q$$

and the current dynamics are

$$\begin{aligned} L_s \frac{di_d}{dt} &= v_d - R_s i_d + L_s i_q N_r \omega_r \\ L_s \frac{di_q}{dt} &= v_q - R_s i_q - L_s i_d N_r \omega_r - \Lambda_r N_r \omega_r \\ L_s \frac{di_0}{dt} &= v_0 - R_s i_0 \end{aligned}$$

where N_r is the number of rotor pole pairs, Λ_r is the rotor flux, ω_r is the rotor speed, R_s is the stator resistance and L_s is the stator inductance.

4.4.2 AC Drive System

The drive system, consisting of the delta-connected motor, the switched-mode power converter and the dc voltage source, is depicted in Figure 19. The legs of the power converter are commanded by pulse-width modulation switching signals u_A, u_B and u_C so as to impose desired average values on converter leg voltages v_A, v_B and v_C. Suppose that the converter leg voltages are assigned using measured θ_r and control parameters (v_m, ϕ_v) such that

$$\begin{aligned} v_A &= \tfrac{1}{2} V_{\rm dc} + \sqrt{\tfrac{2}{9}}\, v_m \cos \vartheta_{v_A} \\ v_B &= \tfrac{1}{2} V_{\rm dc} + \sqrt{\tfrac{2}{9}}\, v_m \cos \vartheta_{v_B} \\ v_C &= \tfrac{1}{2} V_{\rm dc} + \sqrt{\tfrac{2}{9}}\, v_m \cos \vartheta_{v_C} \end{aligned}$$

where

$$\vartheta_{v_A} = N_r\theta_r + \phi_v - \tfrac{\pi}{6}$$

$$\vartheta_{v_B} = N_r\theta_r + \phi_v - \tfrac{\pi}{6} - \tfrac{2\pi}{3}$$

$$\vartheta_{v_C} = N_r\theta_r + \phi_v - \tfrac{\pi}{6} + \tfrac{2\pi}{3}.$$

If the motor phase voltages

$$v_a = v_A - v_B$$

$$v_b = v_B - v_C$$

$$v_c = v_C - v_A$$

are transformed using 8 and 9, then

$$v_d = v_m \cos\phi_v$$

$$v_q = v_m \sin\phi_v$$

$$v_0 = 0.$$

Due to the physical constraints

$$0 \le v_A \le V_{\mathrm{dc}}$$

$$0 \le v_B \le V_{\mathrm{dc}}$$

$$0 \le v_C \le V_{\mathrm{dc}}$$

it is required that

$$0 \le \sqrt{\tfrac{2}{9}}\, v_m \le \tfrac{1}{2} V_{\mathrm{dc}}$$

and hence

$$\|(v_d, v_q)\| \le \sqrt{\tfrac{9}{8}}\, V_{\mathrm{dc}}.$$

Suppose that the motor current flowing in response to the application of motor voltage is expressed in the form

$$i_d = i_m \cos\phi_i$$

$$i_q = i_m \sin\phi_i$$

$$i_0 = 0.$$

The converter leg currents

$$i_A = i_a - i_c$$

$$i_B = i_b - i_a$$

$$i_C = i_c - i_b$$

obtained using 8 and 9 are

$$i_A = \sqrt{2}\, i_m \cos \vartheta_{i_A}$$

$$i_B = \sqrt{2}\, i_m \cos \vartheta_{i_B}$$

$$i_C = \sqrt{2}\, i_m \cos \vartheta_{i_C}$$

where

$$\vartheta_{i_A} = N_r \theta_r + \phi_i - \tfrac{\pi}{6}$$

$$\vartheta_{i_B} = N_r \theta_r + \phi_i - \tfrac{\pi}{6} - \tfrac{2\pi}{3}$$

$$\vartheta_{i_C} = N_r \theta_r + \phi_i - \tfrac{\pi}{6} + \tfrac{2\pi}{3}.$$

Due to the physical constraints

$$|i_A| \leq I_{\max}$$

$$|i_B| \leq I_{\max}$$

$$|i_C| \leq I_{\max}$$

it is required that

$$0 \leq \sqrt{2}\, i_m \leq I_{\max}$$

and hence

$$\|(i_d, i_q)\| \leq \sqrt{\tfrac{1}{2}}\, I_{\max}.$$

The torque-speed capability of the drive system is limited by the voltage and current limits

$$|(v_d, v_q)| \leq \sqrt{\tfrac{9}{8}}\, V_{\mathrm{dc}}, \quad \|(i_d, i_q)\| \leq \sqrt{\tfrac{1}{2}}\, I_{\max}.$$

4.4.3 τ vs. ω Curve

The torque vs. speed capability of the AC machine has been determined by an analysis adopted from [83]. The schematic diagrams, reference manuals, and data sheets of the motor and driver chip were consulted to determine the operational limits of each component. AC motor operation is rated for 24.0V and 5.81A and has a peak current of 11.0A. The driver chip is capable of boosting PWM gating signals anywhere from $6-60$V, and the current sense circuitry is designed to measure ± 16.4A. In this project, the chosen operation limits are 5.0A and 24.0V, and over-current protection is programmed to disable the driver circuitry if currents in excess of 10.0A are measured. The base speed (ω_{base}) is by definition the largest speed at which the maximum torque is available,

$$\omega_{\text{base}} = \frac{V_{\max}}{N\sqrt{\Lambda^2 + L^2 {I_{\max}}^2}}$$

and since the feedback control law does not prohibit the motor from operating in the flux weakening region, the maximum speed is

$$\omega_{\max} = \omega_{\text{base}} \frac{\Lambda^2 + L^2 {I_{\max}}^2}{\Lambda^2 - L^2 {I_{\max}}^2}.$$

Based on the consulted quantities the actuator will operate with a torque-speed characteristic as shown in Figure 20.

4.4.4 Parameter Identification

The parameter identification problem considered here relates to a single-axis rotational motion system, driven by a PM synchronous motor, satisfying dynamic equations of the form

$$\begin{aligned} \dot{\theta} &= \omega \\ J\dot{\omega} &= T_e(i_q) - T_f(\omega) - T_c(\theta) \end{aligned} \tag{10}$$

where θ and ω denote angular position and angular speed, i_q denotes the q-axis current, T_e denotes the electromagnetic torque function, T_f denotes the friction torque function, T_c denotes the cogging torque function, and J denotes the unknown combined inertia of the

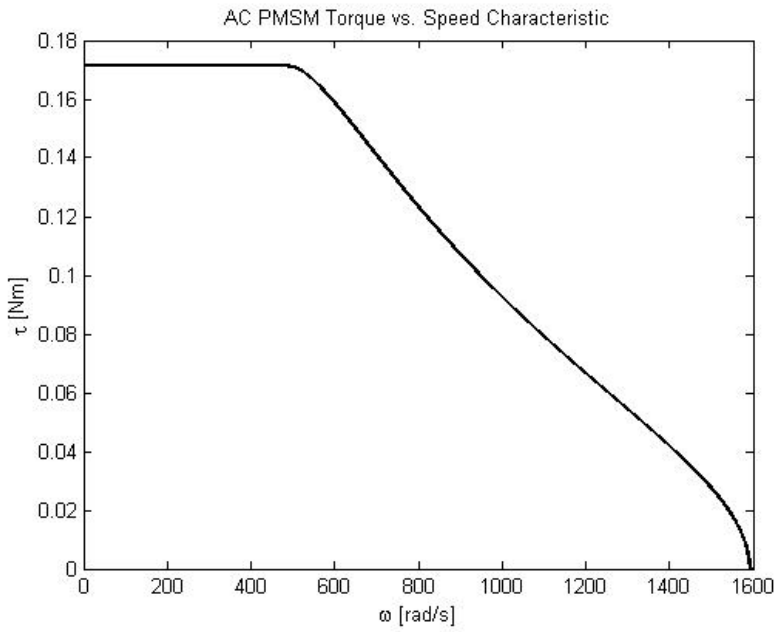

Figure 20: PM synchronous motor torque vs. speed characteristic.

rotor and its load. The relationship between electromagnetic torque and q-axis current is given by

$$T_e(i_q) = K_r i_q, \quad K_r = \Lambda_r N_r$$

where K_r is a known constant. The relationship between friction torque and speed is given by

$$T_f(\omega) = \alpha\,\omega + \left(\beta_c + (\beta_s - \beta_c)\, e^{-\left(\frac{\omega}{\omega_s}\right)^2}\right) \operatorname{sgn}(\omega) \tag{11}$$

where α is the unknown viscous friction coefficient, β_c is the unknown Coulomb friction value, β_s is the unknown Stribeck friction value, and ω_s is the unknown Stribeck friction speed. The relationship between cogging torque and position is given by

$$T_c(\theta) = \sum_{n=1}^{H} \gamma_n \sin\left(nP\left(\theta - \phi\right)\right) \tag{12}$$

where H is the number of harmonic components, P is the cogging torque frequency, $\gamma_1, \ldots, \gamma_H$ are the unknown cogging torque amplitudes, and ϕ is the unknown cogging torque phase.

Of all the unknown parameters, P is the simplest to determine. Cogging torque is a consequence of rotor poles interacting with stator slots, and it is straightforward to establish

that $P = \text{lcm}(N_p, N_s)$ where N_p is the number of rotor poles, N_s is the number of stator slots, and lcm stands for least common multiple. If $N_p = 8$ and $N_s = 6$, which is true for the experimental system, then the multiples of N_p are $\{8, 16, 24, \ldots\}$, the multiples of N_s are $\{6, 12, 18, 24, \ldots\}$, and hence $P = 24$. If the values of N_p and N_s are not known, then P may be determined by simply counting the number of equilibrium positions experienced in one mechanical revolution as rotational steps between equilibrium positions are manually imposed.

Having pre-computed the value of P, and taking H to be some fixed integer, the parameter identification problem considered here involves $6 + H$ unknown parameters. Therefore, if it is determined that six cogging harmonics adequately characterize the system, then there will be 12 unknown parameter values that must be determined using experimental data. Table 7 lists all parameter values describing the experimental system,[1] and the identification procedures used to determine these values are described in the following sections. The table consists of four groups of rows: known parameters determined from the data-sheet; the friction parameters identified using constant-speed experiments; the inertia parameter identified using coast-down experiments; and the cogging parameters identified using cogging-alignment and rotation voltage experiments.

Before accurate experimental data may be measured, it is first essential to perform sensor calibrations. The position sensor must be calibrated so that the magnetic alignment assumptions used throughout the magnetic modeling will be valid; this type of sensor calibration is relatively straightforward, requiring only the application of well-chosen converter voltages to achieve a desired equilibrium orientation between rotor and stator. The calibration of the current sensing system is also necessary for accurate modeling the electromagnetic torque, and is performed following the procedure in §4.3.

[1] The justification for using six cogging harmonics will be provided later in §4.4.4.4.

Table 7: Parameter Values of the AC Motor

Parameter	Units	Value	Comment
P	—	24	obtained from datasheet
K	Nm/A	43.6×10^{-3}	obtained from datasheet
α	Nm s	3.6×10^{-6}	identified using §4.4.4.2 procedure
β_c	Nm	0.00305	identified using §4.4.4.2 procedure
β_s	Nm	0.00844	identified using §4.4.4.2 procedure
ω_s	rad/s	1.64	identified using §4.4.4.2 procedure
J	kg m^2	1.55×10^{-4}	identified using §4.4.4.3 procedure
ϕ	rad	-0.1206	identified using §4.4.4.4 procedure
γ_1	Nm	0.0097	identified using §4.4.4.4 procedure
γ_2	Nm	-0.0031	identified using §4.4.4.4 procedure
γ_3	Nm	0.0015	identified using §4.4.4.4 procedure
γ_4	Nm	-0.0016	identified using §4.4.4.4 procedure
γ_5	Nm	0.0003	identified using §4.4.4.4 procedure
γ_6	Nm	-0.0006	identified using §4.4.4.4 procedure

4.4.4.1 Encoder Initialization

For the AC motor, it is possible to apply constant converter voltages so as to impose the torque-angle characteristic

$$T_e(\theta) = -K_r \frac{V_{\text{init}}}{R_s} \sin(N_r(\theta - \theta_{\text{init}})),$$

in which case the equilibrium value of rotor position θ must satisfy the equilibrium torque constraint

$$0 = -K_r \frac{V_{\text{init}}}{R_s} \sin(N_r(\theta - \theta_{\text{init}})) - T_f(0) - T_c(\theta).$$

Since it is not possible to know the precise value of the terms $T_f(0)$ and $T_c(\theta)$ in this constraint equation, the excitation parameter V_{init} is made large so that the equilibrium value of rotor position will be insensitive to the unknown terms; with sufficiently large V_{init}, it follows that $\theta \approx \theta_{\text{init}}$. The first time this procedure is used, its purpose is to calibrate the position sensor so that its reference angle is consistent with modeling assumptions; to do this, assign $\theta_{\text{init}} = 0$, apply the corresponding constant converter voltages, wait for the rotor to settle into an equilibrium position, and then reset the position sensor output to read $\theta = 0$.

4.4.4.2 Friction

The friction parameters are identified using constant-speed experiments. Constant values of v_q are applied (with $v_d = 0$), resulting in essentially constant electromagnetic torque and speed at steady state. M trials are used to generate the steady-state current-speed pairs $(i_{q,\infty}, \omega_\infty)$ and, according to (10), each of them satisfies

$$T_f(\omega_\infty) \approx T_e(i_{q,\infty})$$

since the average value of $T_c(\theta)$ is zero. According to (11), the following system of M equations involving the unknown friction parameters must be approximately satisfied:

$$\begin{bmatrix} \omega_\infty[1] & \left(1 - e^{-\left(\frac{\omega_\infty[1]}{\omega_s}\right)^2}\right)\operatorname{sgn}(\omega_\infty[1]) & e^{-\left(\frac{\omega_\infty[1]}{\omega_s}\right)^2}\operatorname{sgn}(\omega_\infty[1]) \\ \vdots & \vdots & \vdots \\ \omega_\infty[M] & \left(1 - e^{-\left(\frac{\omega_\infty[M]}{\omega_s}\right)^2}\right)\operatorname{sgn}(\omega_\infty[M]) & e^{-\left(\frac{\omega_\infty[M]}{\omega_s}\right)^2}\operatorname{sgn}(\omega_\infty[M]) \end{bmatrix} \begin{bmatrix} \alpha \\ \beta_c \\ \beta_s \end{bmatrix} = \begin{bmatrix} T_e(i_{q,\infty}[1]) \\ \vdots \\ T_e(i_{q,\infty}[M]) \end{bmatrix}. \tag{13}$$

Note that (13) depends linearly on α, β_c, and β_s, but nonlinearly on ω_s. For any fixed choice of these friction parameters, the residual error between the friction function and measured data is given by

$$E = \sum_{m=1}^{M} \left\{T_f(\omega_\infty[m]) - T_e(i_{q,\infty}[m])\right\}^2. \tag{14}$$

In (13) and (14), current and position are measured, and speed is approximated using discrete-time differentiation. A direct search approach to solving the nonlinear least-squares problem is employed, as outlined by the procedure displayed below.

1. obtain K_r from data-sheet or by measurement
2. collect N values of $\theta[n]$ and $i_q[n]$ for each of M constant-speed trials
3. utilize discrete-time differentiation to approximate $\omega[n]$ from $\theta[n]$
4. determine the limit values for each trial, $\omega_\infty[m]$ and $i_{q,\infty}[m]$
5. for candidate values of ω_s
   (a) solve linear least squares problem (13)
   (b) compute and store residual error using (14)
6. choose α, β_c, β_s and ω_s corresponding to smallest residual error

When applied to the experimental actuator, this procedure resulted in a reasonable agreement between the measured data and the parameterized function $T_f(\omega)$, as shown in

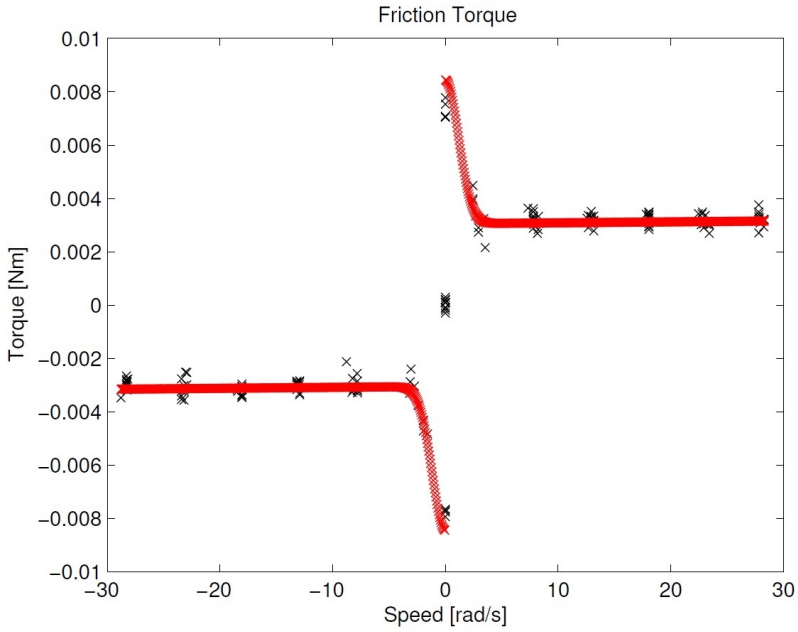

Figure 21: AC motor identification results from constant-speed experiments.

Figure 21; the black symbols represent measured data, whereas the red symbols represent evaluations of $T_f(\omega)$. The identified parameters are reported in Table 7.

4.4.4.3 Inertia

The inertia parameter is identified using coast-down experiments. Constant values of v_q are applied (with $v_d = 0$) in order to reach a high-speed steady-state condition. The coast-down event begins shortly after the converter leg switches are placed into a high-impedance state, once the converter leg currents decay to zero. M trials are used to generate the transient speed-time pairs (ω, t) and, according to (10), the pairs for each trial satisfy

$$J\dot{\omega}(t) \approx -\alpha\,\omega(t) - \beta_c\,\mathrm{sgn}(\omega(t)) \tag{15}$$

since the average value of $T_c(\theta)$ is zero and $\omega \gg 0$. The solution of differential equation (15) is

$$\omega(t) \approx \left(\left(|\omega_0| + \frac{\beta_c}{\alpha}\right) e^{-\frac{\alpha}{J}t} - \frac{\beta_c}{\alpha}\right) \mathrm{sgn}(\omega_0) \tag{16}$$

where ω_0 denotes the initial value of ω. Since there are M trials, each with N data pairs, the residual error generated by a candidate value of J, according to (16), is

$$E = \sum_{m=1}^{M} \sum_{n=1}^{N} \left\{ \omega[m,n] - \left(\left(|\omega[m,1]| + \frac{\beta_c}{\alpha} \right) e^{-\frac{\alpha}{J} t[m,n]} - \frac{\beta_c}{\alpha} \right) \operatorname{sgn}(\omega[m,1]) \right\}^2 . \qquad (17)$$

In (17), time and position are measured, and speed is approximated using discrete-time differentiation. Note that (17) depends nonlinearly on J. A direct search approach to solving the nonlinear least-squares problem is employed, as outlined by the procedure displayed below.

1. given previously identified parameter values: α and β_c
2. collect N values of $\theta[n]$ and $t[n]$ for each of M coast-down trials
3. utilize discrete-time differentiation to approximate $\omega[n]$ from $\theta[n]$
4. for candidate values of J, compute and store residual error using (17)
5. choose J corresponding to smallest residual error

When applied to determine the combined rotor shaft and reaction wheel inertia of the experimental actuator, this procedure resulted in a close agreement between measured behavior and modeled behavior, as shown in Figure 22; the blue symbols represent measured data, whereas the red symbols represent evaluations of the solution formula (16). The identified parameter is reported in Table 7. Since J may be computed directly from a specification of geometry and material, its value was also estimated in this way; the computed value was 1.54×10^{-4} kg m^2, whereas the identified value was 1.53×10^{-4} kg m^2, representing an error of less than 0.7%.

4.4.4.4 Cogging Torque

The cogging parameters are identified using a combination of cogging-alignment experiments and rotation-voltage experiments, as described below. The cogging parameters include the number of harmonics H, the harmonic amplitudes $\gamma_1, \ldots, \gamma_H$, and the phase angle ϕ. Note that the parameter identification method developed here guarantees that the natural physical properties of cogging torque have been properly accounted for.

Cogging-alignment experiments. Constant converter leg voltages are applied, as described in §4.3, in order to drive the rotor to a prescribed initial position $\theta \approx \theta_{\text{init}}$. The cogging-alignment event begins shortly after the converter leg switches are placed into a

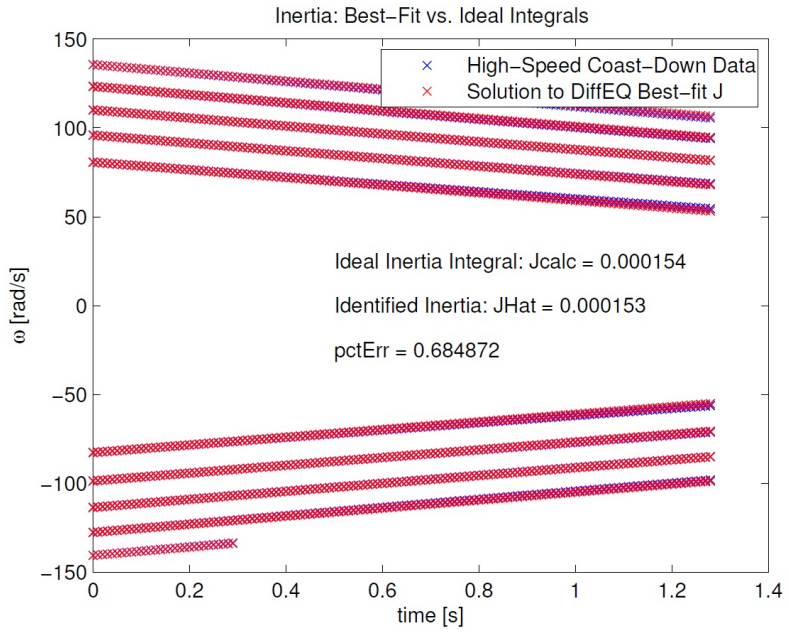

Figure 22: AC motor identification results from coast-down experiments.

high-impedance state, and the converter leg currents have decayed to zero. M trials are used to generate transient response data for θ, ω and $\dot{\omega}$ with various θ_{init} and, according to (10), within each trial these data satisfy

$$T_c(\theta(t)) = -T_f(\omega(t)) - J\dot{\omega}(t) \tag{18}$$

since the electromagnetic torque is zero. According to (12), the following system of H equations involving the unknown cogging parameters must be approximately satisfied:

$$\begin{bmatrix} \sin\left(P\left(\theta[1,1]-\phi\right)\right) & \cdots & \sin\left(HP\left(\theta[1,1]-\phi\right)\right) \\ \vdots & \vdots & \vdots \\ \sin\left(P\left(\theta[M,N]-\phi\right)\right) & \cdots & \sin\left(HP\left(\theta[M,N]-\phi\right)\right) \end{bmatrix} \begin{bmatrix} \gamma_1 \\ \vdots \\ \gamma_H \end{bmatrix} = - \begin{bmatrix} T_f(\omega[1,1]) + J\dot{\omega}[1,1] \\ \vdots \\ T_f(\omega[M,N]) + J\dot{\omega}[M,N] \end{bmatrix}. \tag{19}$$

The phase angle ϕ in (19) represents the value of θ at which the cogging torque is zero and, hence, the steady-state value of θ in the absence of static friction; by proper choice of initial positions, the influence of static friction on the identified ϕ is greatly reduced by averaging the steady-state values of θ. Note that (19) depends linearly on $\gamma_1, \ldots, \gamma_H$. For any fixed choice of these cogging amplitudes, the residual error between the cogging function and

measured data is given by

$$E = \sum_{m=1}^{M} \sum_{n=1}^{N} \left\{ T_c(\theta[m,n]) + T_f(\omega[m,n]) + J\dot{\omega}[m,n] \right\}^2 . \tag{20}$$

In (19) and (20), position is measured, whereas both speed and acceleration are approximated using discrete-time differentiation.

Rotation-voltage experiments. The unforced value of θ (i.e. its equilibrium value due to cogging acting alone) is used as an initial position, and a constant value of v_q is increased (with $v_d = 0$) until the rotor breaks away and begins a sustained rotation.[2] Initially the cogging torque will be zero, so initial breakaway must overcome only static friction torque; once initial breakaway has occurred, friction torque reduces but cogging torque begins to be significant. Hence, the rotation voltage V_r as defined here must simultaneously account for both friction torque and cogging torque, in order to represent the smallest voltage consistent with sustained rotation. Once measured, V_r may serve as an additional constraint on cogging amplitudes; in particular, from (10), (11) and (12), physical considerations require the value of Γ defined as

$$\Gamma = \left\{ \frac{R_s}{K_r} \left| \beta_s + \sum_{n=1}^{H} \gamma_n \sin\left(nP\left(-\phi\right)\right) \right| - V_r \right\}^2 \tag{21}$$

to be as small as possible; Γ is interpreted here to be a function of $\gamma_1, \ldots, \gamma_H$.

A direct search approach to identifying the cogging parameters is employed, as outlined by the procedure displayed below.

1. given previously identified parameter values: α, β_c, β_s, ω_s and J
2. collect N values of $\theta[n]$ for each of M cogging-alignment trials
3. compute ϕ by averaging M steady-state positions modulo $2\pi/P$
4. utilize discrete-time differentiation to approximate $\omega[n]$ and $\dot{\omega}[n]$ from $\theta[n]$
5. for various values of H
   (a) solve linear least squares problem (19)
   (b) compute and store E from (20) and Γ from (21)
6. choose H and $\gamma_1, \ldots, \gamma_H$ corresponding to smallest weighted error $E + \Gamma$

When applied to the experimental actuator, this procedure resulted in a feasible cogging torque characteristic, as shown in Figure 23; the blue symbols represent measured

[2] Since $\beta_s < \gamma_1$ is feasible, and indeed is the case for the experimental actuator, it is possible to experience break away without achieving sustained rotation.

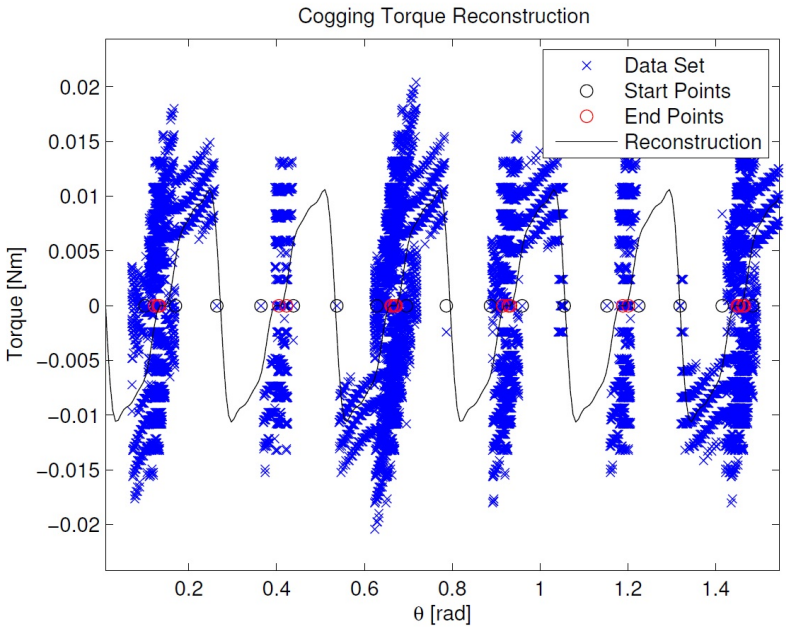

Figure 23: AC motor identification results from cogging-alignment and rotation-voltage experiments.

data processed according to (18), whereas the black curve represents evaluations of $T_c(\theta)$. Though the agreement here between modeled and measured behavior is not as strong as one might hope for, this type of comparison is strongly influenced by two considerations: the measured data come from transient responses; only half of the equilibrium positions (the stable ones) are encountered in practice. The identified parameters are reported in Table 7 for the case when when $H = 6$. There are better fitting cogging torque models ($H = 16$) as seen in Figure 24; however, the inclusion of higher harmonic content means that noise characteristics will be included in the nonlinearity model, and hence we anticipate introducing a modification of the procedures' step 6 in the future.

4.4.4.5 Model Validation

After friction, inertia, and cogging characterizations were obtained, the whole model was compared against ideal simulation behavior. There is good agreement between the characterized model and ideal simulations, as shown in Figure 25. The black symbols represent measured position and speed, and the red symbols represent simulated position and speed using identified parameters. The only major discrepancies present are "missing" the final

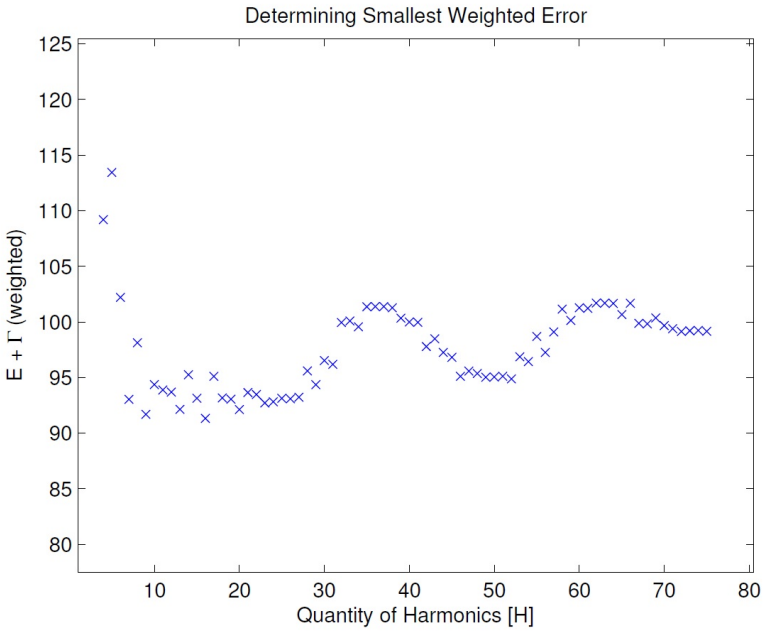

Figure 24: $E + \Gamma$ as a function of number of harmonic terms.

position due to operating outside the speed range of values used to derive the friction model.

4.5 DC Motor Characterization

The DC motor is characterized to provide a simulation model that can accurately predict controller performance in the presence of various imperfections. The torque vs. speed capability of the DC machine is developed from an analysis of the motor dynamics, converter operating limits, and data sheet values. Procedures for identifying the parameters of characteristics such as gear play and higher-order friction effects are developed, implemented, and validated. Information obtained from the torque vs. speed capability analysis indicates what the actuator saturation limits are, and this data can be incorporated during control design to implement integrator anti-windup.

4.5.1 Motor Dynamics

The cross section view of the three-phase motor is depicted in Figure 26 so as to reveal its magnetic geometry. As shown in the magnetic geometry diagram, the mechanical commutator physically switches between the rotor-mounted conductors to enforce an orthogonal

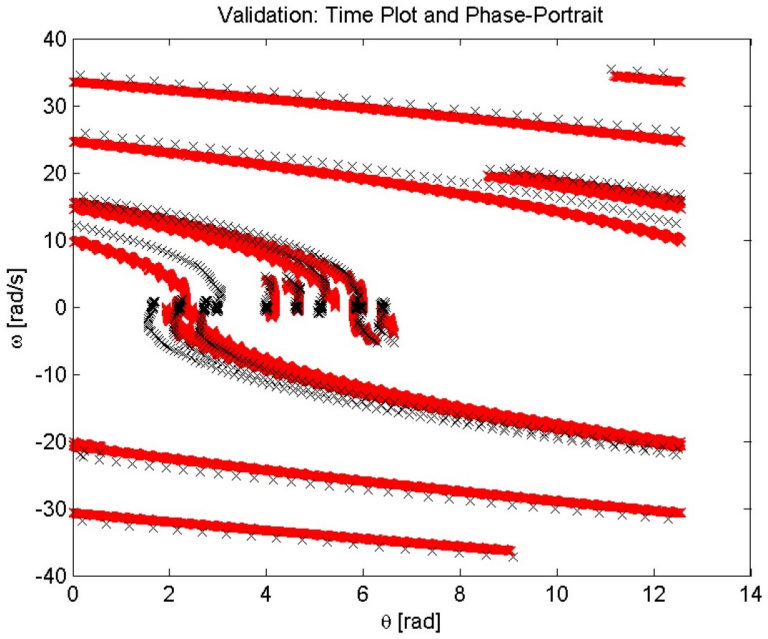

Figure 25: AC motor model validation, using $H = 6$; measurement versus simulation.

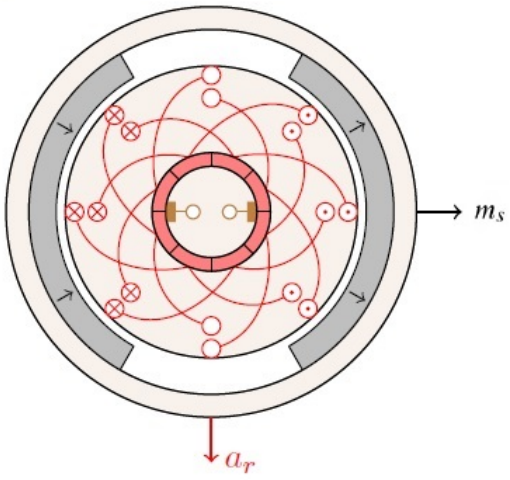

Figure 26: DC motor magnetics.

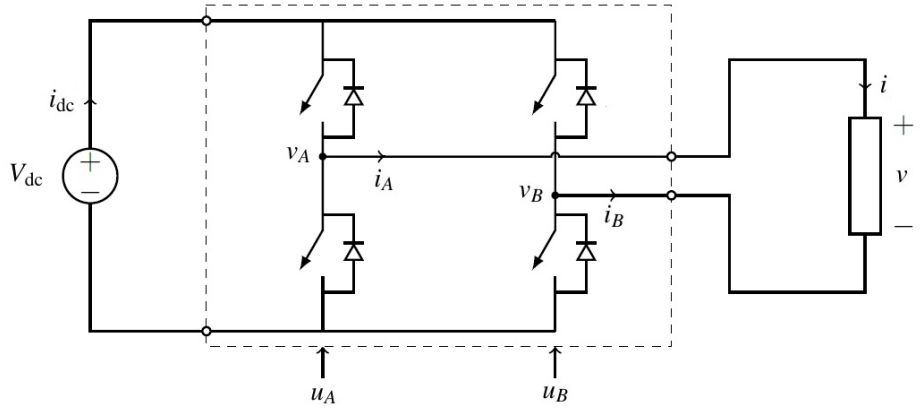

Figure 27: DC motor drive system.

relationship between the magnetic field generated by armature currents (a_r) and the magnetic field generated by the stator-mounted permanent magnets (m_s). The electromagnetic torque generated by the interaction of these magnetic fields is

$$\tau = Ki(t)$$

and the current dynamics are

$$L_s \frac{di}{dt} = v - R_s i - K\omega_r$$

where K is the torque (and back EMF) constant, ω_r is the rotor speed, R_s is the stator resistance and L_s is the stator inductance.

4.5.2 Drive System

The drive system, consisting brushed DC motor, DC-to-DC converter (H-Bridge) and the DC voltage source, is depicted in Figure 27. The legs of the power converter are commanded by pulse-width modulation switching signals u_A and u_B so as to impose a desired average voltage $v = v_A - v_B$.

Due to the physical constraints

$$0 \leq v_A \leq V_{dc}$$

$$0 \leq v_B \leq V_{dc}$$

it is required that

$$-V_{\text{dc}} \leq v \leq V_{\text{dc}}$$

and hence

$$|v| \leq V_{\text{dc}}.$$

Due to the physical constraints

$$|i_A| \leq I_{\max}$$

$$|i_B| \leq I_{\max}$$

it is required that

$$-I_{\max} \leq i \leq I_{\max}$$

and hence

$$|i| \leq I_{\max}.$$

The torque-speed capability of the drive system is limited by the voltage and current limits

$$|v| \leq V_{\text{dc}}, \quad |i| \leq I_{\max}.$$

4.5.3 τ vs. ω Curve

The torque vs. speed capability of the DC machine has been determined by an analysis adopted from [83]. The schematic diagrams, reference manuals, and data sheets of the motor and driver chip were consulted to determine the operational limits of each component. DC motor operation is rated for 24.0V and 4.0A and has a peak current of 24.7A. The driver chip is capable of boosting PWM gating signals anywhere from $6 - 60$V, and the current sense circuitry is designed to measure $\pm$16.4A. In this project, the chosen operation limits are 4.0A and 24.0V, and over-current protection is programmed to disable the driver circuitry if currents in excess of 10.0A are measured. It is assumed that current dynamics are at

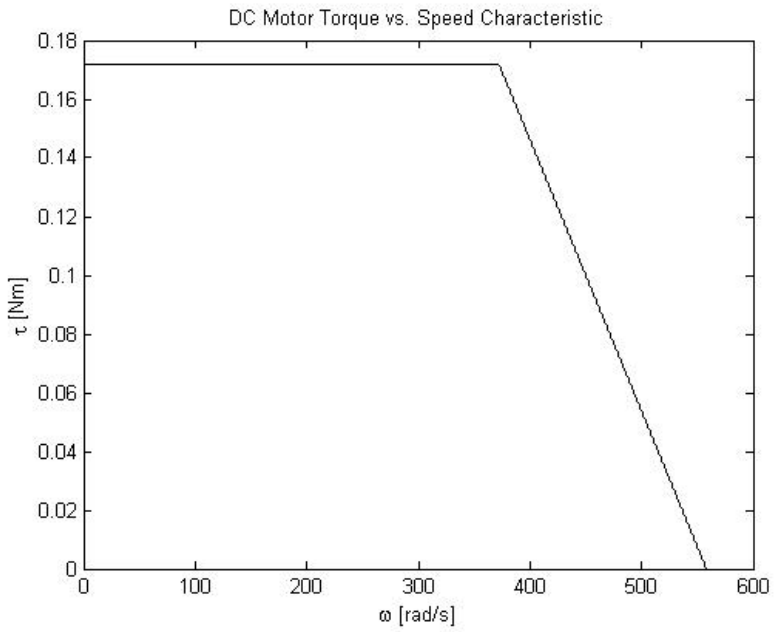

Figure 28: DC motor torque vs. speed characteristic.

steady-state and the maximum current is redefined as the motor limit ($I_{\max} = 4.0\text{A}$). The maximum torque available and maximum achievable speed are

$$T_{\max} = K I_{\max}, \quad \omega_{\max} = \frac{V_{\text{dc}}}{K}.$$

The base speed is by definition the largest speed at which the maximum torque is available,

$$\omega_{\text{base}} = \frac{V_{\text{dc}} - R_s I_{\max}}{K}.$$

Based on the consulted quantities the actuator will operate with a torque-speed characteristic as shown in Figure 28.

4.5.4 Parameter Identification

The parameter identification problem considered here relates to a single-axis rotational motion system, driven by a DC motor, satisfying dynamic equations of the form

$$\begin{aligned} \dot{\theta} &= \omega \\ J\dot{\omega} &= T_e(i) - T_f(\omega) \end{aligned} \tag{22}$$

where θ and ω denote angular position and angular speed, i denotes the motor current, T_e denotes the electromagnetic torque function, T_f denotes the friction torque function, and J

Table 8: Parameter Values of the DC Motors

Motor	Parameter	Units	Value	Comment
Both	K	Nm/A	43.6×10^{-3}	obtained from datasheet
Right	α	Nm s	33.7×10^{-6}	identified using §4.5.4.1 procedure
	β_c	Nm	15.2×10^{-3}	identified using §4.5.4.1 procedure
	J	kg m^2	3.79×10^{-4}	identified using §4.5.4.2 procedure
Left	α	Nm s	32.1×10^{-6}	identified using §4.5.4.1 procedure
	β_c	Nm	13.1×10^{-3}	identified using §4.5.4.1 procedure
	J	kg m^2	3.85×10^{-4}	identified using §4.5.4.2 procedure

denotes the unknown inertia of the rotor. The relationship between electromagnetic torque and motor current is given by

$$T_e(i) = Ki$$

where K is a known constant. Since the data inspected in §4.5.4.1 indicates that the dominant friction effects are Coulomb and viscous friction (no Stribeck), then the relationship between friction torque and speed is given by

$$T_f(\omega) = \alpha\,\omega + \beta_c\ \mathrm{sgn}\,(\omega) \tag{23}$$

where α is the unknown viscous friction coefficient, and β_c is the unknown Coulomb friction value. Table 8 lists all parameter values describing the experimental system, and the following sections describe the procedures used to identify these values. The table consists of three groups of rows: parameters that apply to both motors, parameters that apply to the right motor, and parameters that apply to the left motor. Before accurate experimental data may be measured, however, it is first essential to perform calibration of the current sensing system. To model the electromagnetic torque accurately, the ADC is calibrated following the procedure in §4.3.

4.5.4.1 Friction

The friction parameters are identified using constant-speed experiments. Constant values of v are applied, resulting in essentially constant electromagnetic torque and speed at steady

state. M trials are used to generate the steady-state current-speed pairs $(i_\infty, \omega_\infty)$ and, according to (22), each of them satisfies

$$T_f(\omega_\infty) \approx T_e(i_\infty).$$

According to (23), the following system of M equations involving the unknown friction parameters must be approximately satisfied:

$$\begin{bmatrix} \omega_\infty[1] & \operatorname{sgn}(\omega_\infty[1]) \\ \vdots & \vdots \\ \omega_\infty[M] & \operatorname{sgn}(\omega_\infty[M]) \end{bmatrix} \begin{bmatrix} \alpha \\ \beta_c \end{bmatrix} = \begin{bmatrix} T_e(i_\infty[1]) \\ \vdots \\ T_e(i_\infty[M]) \end{bmatrix}. \tag{24}$$

In (24), current and position are measured, and speed is approximated using discrete-time differentiation. Utilization of the pseudo-inverse is employed to solve the least-squares problem as outlined by the procedure displayed below.

1. obtain K from data-sheet or by measurement
2. collect N values of $\theta[n]$ and $i[n]$ for each of M constant-speed trials
3. utilize discrete-time differentiation to approximate $\omega[n]$ from $\theta[n]$
4. determine the limit values for each trial, $\omega_\infty[m]$ and $i_\infty[m]$
5. solve linear least squares problem (24)

When applied to the experimental actuators, this procedure resulted in a reasonable agreement between the measured data and the parameterized function $T_f(\omega)$, as shown in Figure 29; the dot symbols represent measured data, whereas the solid lines represent evaluations of $T_f(\omega)$. The identified parameters are reported in Table 8.

4.5.4.2 Inertia

The inertia parameter is identified using coast-down experiments. Constant values of v are applied in order to reach a high-speed steady-state condition. The coast-down event begins shortly after the converter leg switches are placed into a high-impedance state, once the converter leg currents decay to zero. M trials are used to generate the transient speed-time pairs (ω, t) and, according to (22), the pairs for each trial satisfy

$$J\dot{\omega}(t) \approx -\alpha\,\omega(t) - \beta_c \operatorname{sgn}(\omega(t)). \tag{25}$$

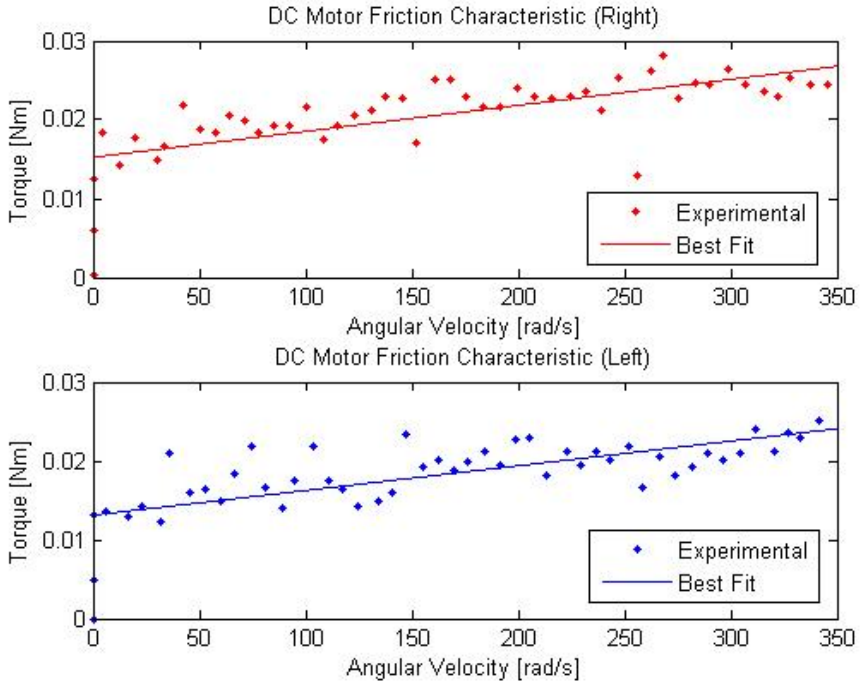

Figure 29: DC motor identification results from constant-speed experiments.

The solution of differential equation (25) is

$$\omega(t) \approx \left(\left(|\omega_0| + \frac{\beta_c}{\alpha} \right) e^{-\frac{\alpha}{J}t} - \frac{\beta_c}{\alpha} \right) \mathrm{sgn}(\omega_0) \tag{26}$$

where ω_0 denotes the initial value of ω. Since there are M trials, each with N data pairs, the residual error generated by a candidate value of J, according to (26), is

$$E = \sum_{m=1}^{M} \sum_{n=1}^{N} \left\{ \omega[m,n] - \left(\left(|\omega[m,1]| + \frac{\beta_c}{\alpha} \right) e^{-\frac{\alpha}{J}t[m,n]} - \frac{\beta_c}{\alpha} \right) \mathrm{sgn}(\omega[m,1]) \right\}^2 . \tag{27}$$

In (27), time and position are measured, and speed is approximated using discrete-time differentiation. Note that (27) depends nonlinearly on J. A direct search approach to solving the nonlinear least-squares problem is employed, as outlined by the procedure displayed below.

1. given previously identified parameter values: α and β_c
2. collect N values of $\theta[n]$ and $t[n]$ for each of M coast-down trials
3. utilize discrete-time differentiation to approximate $\omega[n]$ from $\theta[n]$
4. for candidate values of J, compute and store residual error using (27)
5. choose J corresponding to smallest residual error

When applied to the experimental actuators, this procedure resulted in close agreement between measured behaviors and modeled behaviors, as shown in Figure 30; the black curves

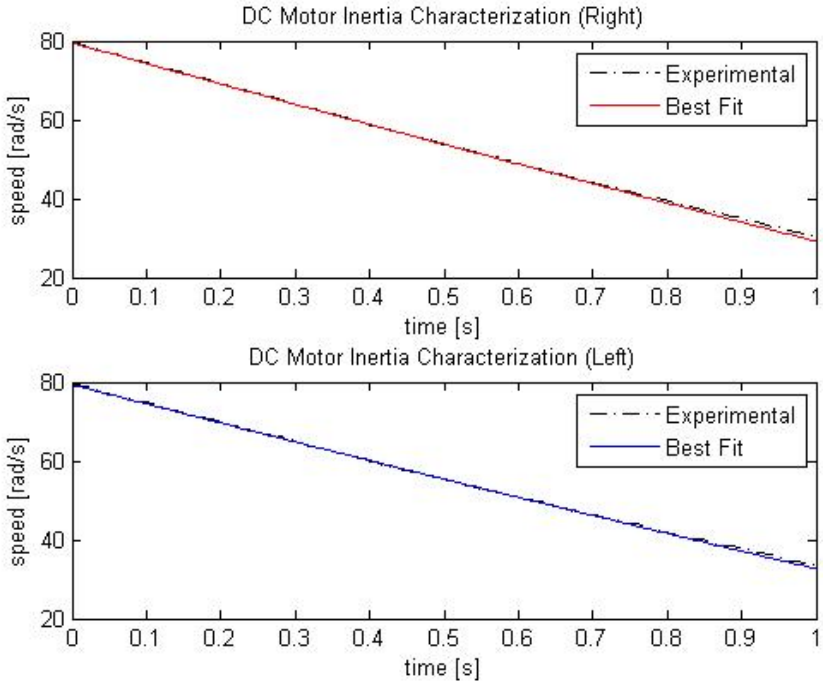

Figure 30: DC motor identification results from coast-down experiments.

represent measured data, whereas the solid curves represent evaluations of the solution formula (26). The identified parameter is reported in Table 8.

4.5.4.3 Model Validation

After friction, and inertia characterizations were obtained, the whole model was compared against ideal simulation behavior. There is good agreement between the characterized model and ideal simulations, as shown in Figure 31. The black dashes represent measured position, and the red and blue curves represent simulated position using identified parameters.

4.5.4.4 Gearbox Backlash

The DC motor position encoders are shaft-mounted and a gearbox connects each motor to a drive wheel. If the drive wheels are locked firmly in place, then any motion measured on the motor shaft represents null space values of the gear play. A sinusoidal torque command large enough to bi-directionally reach the gearbox limits is imposed and the small position deviations on the motor shaft are measured. The effects of backlash and gear deformation are clearly visible in Figure 32. The gear play characteristics for each motor are tabulated

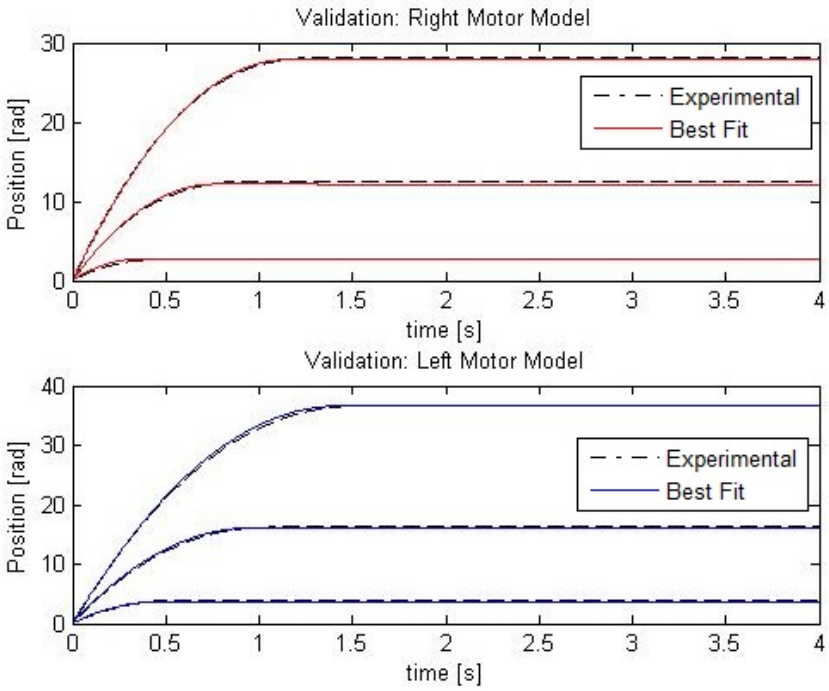

Figure 31: DC motor model validation; measurement versus simulation.

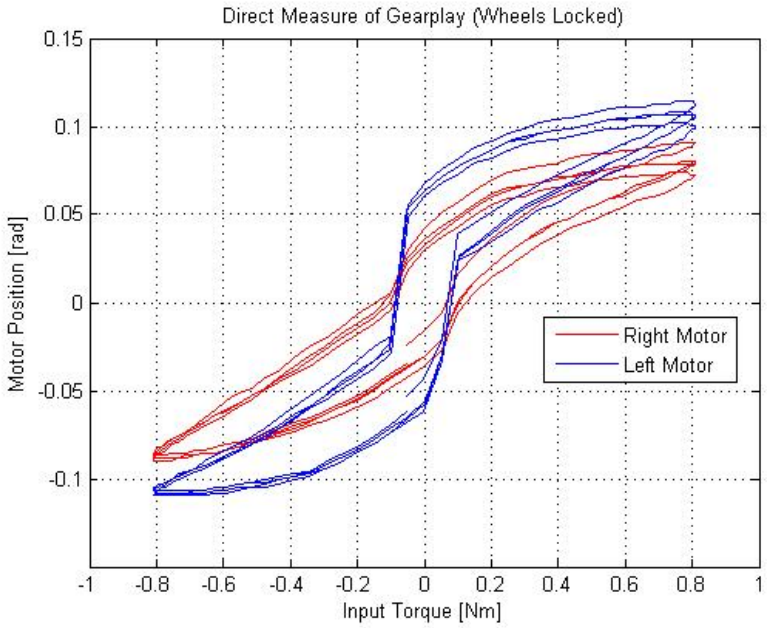

Figure 32: Experimental gear play measurements.

Table 9: DC Motor Gear Play Characteristics

Source	Left	Right	Unit
Backlash	0.109	0.056	rad
Deformation	0.048	0.063	rad
Gear Ratio	6.75	6.75	rad/rad

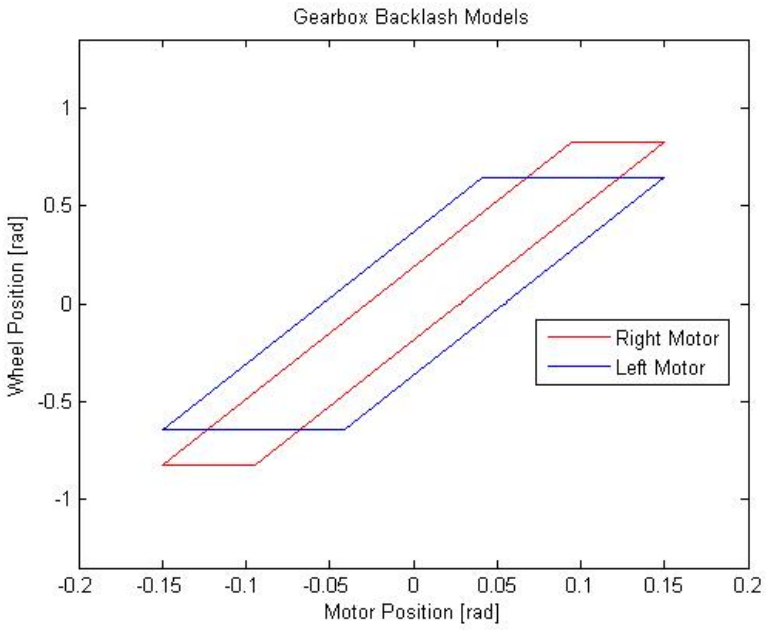

Figure 33: DC motor gearbox backlash models.

in Table 9. If we neglect the deformation since the wheel motion in this region is not completely null, then the gear play can be approximated by the backlash and gearing ratio. The gear play characteristics for both gearboxes are seen in Figure 33

CHAPTER V

CONTROL

Two common implementation flaws affecting experimental results are parameter mismatch and model error. Robust controller design is implemented in two-time scales (fast electrical loop and slow mechanical loop) to overcome parameter imprecision and reject unwanted disturbances. System stability and equilibrium are investigated while under the influence of sensor bias, torque disturbances, and switched mode reference tracking. After completing feedback controller design, a simulation environment is constructed to predict system performance before implementation.

5.1 Reaction Wheel Pendulum

The RWP controller design goal is to keep the pendulum arm upright and point the inertia wheel towards a specified reference. An equilibrium analysis is performed on the mechanical subsystem to determine valid reference signals. Integral control is implemented on the slow (mechanical) and fast (electrical) subsystems to track ideal torque inputs and to provide ideal torque generating currents. A disturbance rejection analysis shows that the developed strategy is immune to cogging torque, Stribeck friction, and sensor bias effects; and that the design goal is unaffected by operating on uneven terrain. Practical considerations are implemented such as actuator saturation, integrator anti-windup, and digital controller design. Experimental measurements are reported and demonstrate a strong agreement with simulated predictions.

5.1.1 Equilibrium Analysis

The RWP equations of motion were derived in §3.2

$$J_1\ddot{\theta}_1 + J_2\ddot{\theta}_2 = (m_1 d_1 + m_2 d_2) g \sin\theta_1$$

$$J_2\ddot{\theta}_2 + J_2\ddot{\theta}_1 = \tau - k_v\dot{\theta}_2$$

where

$$J_1 = I_{1\text{com}} + m_1 {d_1}^2 + I_{2\text{com}} + m_2 d_2^2 \quad \text{and} \quad J_2 = I_{2\text{com}}.$$

All candidate equilibria are determined by analyzing the dynamic equations at steady-state,

$$0 = (m_1 d_1 + m_2 d_2) g \sin\theta_1$$
$$0 = \tau - k_v \dot{\theta}_2.$$

Maintaining equilibrium implies the pendulum must be upright (or hanging downward), and a constant torque must be applied to offset friction effects:

$$\theta_1 = 0$$
$$\tau = k_v \dot{\theta}_2.$$

Since the design goal is to maintain a constant wheel position, all candidate equilibria and the torques required to maintain balance are

$$\bar{\theta}_1 = 0,\ \bar{\dot{\theta}}_1 = 0,\ \bar{\theta}_2 \in \mathcal{R},\ \bar{\dot{\theta}}_2 = 0,\ \text{and}\ \bar{\tau} = 0.$$

5.1.2 Controller Design

Integral control is implemented on the mechanical subsystem to track the ideal torques required to maintain equilibrium. The electrical subsystem receives these ideal torques as a reference, and integral control is implemented to generate them robustly. Output feedback is implemented on the slow subsystem to provide estimates of unmeasured mechanical states, and state feedback is implemented on the fast subsystem since all currents are directly measured. The eigenvalue locations for each subsystem are designed to provide two-time scale operation of a fast inner current loop and a slow outer mechanical loop.

5.1.2.1 Slow Subsystem

The slow subsystem state and input vectors are

$$x = [\theta_1,\ \dot{\theta}_1,\ \theta_2,\ \dot{\theta}_2]^T$$
$$u = \tau.$$

A state-space integral controller is designed to estimate x using measurement of y_m, and regulate y_r using measurement of y_r,

$$\dot{x} = f_m(x,u) \approx A_m x + B_m u$$

$$y_r = C_r x$$

$$y_m = C_m x$$

where

$$f_m(x,u) = \begin{bmatrix} x_2 \\ a_1 \sin x_1 + a_2 x_4 \\ x_4 \\ -a_1 \sin x_1 - \rho a_2 x_4 \end{bmatrix} + \begin{bmatrix} 0 \\ -b \\ 0 \\ \rho b \end{bmatrix} u$$

$$C_r = \begin{bmatrix} 0 & 0 & 1 & 0 \end{bmatrix}$$

$$C_m = \begin{bmatrix} 1 & 0 & 0 & 0 \\ 0 & 0 & 1 & 0 \end{bmatrix}$$

and the design goal with reference $r_s = \bar{\theta}_2$ is

$$\lim_{t\to\infty} y_r = r_s.$$

The design model is obtained by linearization,

$$A_m = \left.\frac{\partial f_m}{\partial x}\right|_{(\bar{x},\ \bar{u})} = \begin{bmatrix} 0 & 1 & 0 & 0 \\ a_1 & 0 & 0 & a_2 \\ 0 & 0 & 0 & 1 \\ -a_1 & 0 & 0 & -\rho\, a_2 \end{bmatrix}$$

$$B_m = \left.\frac{\partial f_m}{\partial u}\right|_{(\bar{x},\ \bar{u})} = \begin{bmatrix} 0 & -b & 0 & \rho b \end{bmatrix}^T$$

where

$$a_1 = \frac{(m_1 d_1 + m_2 d_2) g}{J_1 - J_2}, \quad a_2 = \frac{k_v}{J_1 - J_2}, \quad b = \frac{1}{J_1 - J_2}, \quad \rho = \frac{J_1}{J_2}.$$

The integral controller is implemented by

$$u = -K_{s_1}\hat{x} - K_{s_2}\sigma$$

$$\dot{\hat{x}} = A_m\hat{x} + B_m u - L_s(C_m\hat{x} - y_m)$$

$$\dot{\sigma} = y_r - r_s$$

under the requirements that

$$(A_m,\ B_m) \sim \text{controllable}$$

$$(A_m,\ C_m) \sim \text{observable}$$

and

$$\det \begin{bmatrix} A_m & B_m \\ C_r & 0 \end{bmatrix} \neq 0.$$

The linearized dynamics are rewritten

$$\begin{bmatrix} \dot{x} \\ \dot{\sigma} \\ \dot{\epsilon} \end{bmatrix} = \begin{bmatrix} A_m - B_m K_{s_1} & -B_m K_{s_2} & -B_m K_{s_1} \\ C_r & 0 & 0 \\ 0 & 0 & A_m - L_s C_m \end{bmatrix} \begin{bmatrix} x \\ \sigma \\ \epsilon \end{bmatrix} + \begin{bmatrix} 0 \\ -1 \\ 0 \end{bmatrix} r_s$$

where

$$\epsilon = \hat{x} - x.$$

The following notations are defined to assist with gain evaluation:

$$A_s = \begin{bmatrix} A_m & 0 \\ C_r & 0 \end{bmatrix} \quad B_s = \begin{bmatrix} B_m \\ 0 \end{bmatrix} \quad K_s = \begin{bmatrix} K_{s_1} & K_{s_2} \end{bmatrix}.$$

The gain matrix K_s is chosen to minimize

$$\int_0^\infty (x^T Q x + R u^2)\ dt$$

subject to the diagonal weights

$$Q_{ii} = x_{i,\max}^{-2}, \qquad R = u_{\max}^{-2}.$$

The optimal choice of K_s is given by

$$K_s = R^{-1}B_m^T X$$

where X is the unique positive-semidefinite solution of

$$A_s^T X + X A_s - X B_s R^{-1} B_s^T X + Q = 0.$$

L_s is designed by employing a loop transfer recovery procedure that utilizes the weighting matrices

$$W = qB_m B_m^T, \quad V = I.$$

The desired choice of L_s is given by

$$L_s = Y C_m^T V^{-1}$$

where Y is the unique positive-semidefinite solution of

$$A_m Y + Y A_m^T - Y C_m^T V^{-1} C_m Y + W = 0.$$

5.1.2.2 Fast Subsystem

The fast subsystem tracks the ideal torque reference (u) by actuating an AC motor with the currents (i_d, i_q) induced by imposing voltages (v_d, v_q) on the stator. The state and input vectors are

$$z = [i_d,\ i_q]^T$$

$$v = [v_d,\ v_q]^T.$$

A state-space integral controller is designed to regulate z using the electrical dynamics

$$\dot{z} = f_e(z, v, w) \approx A_e z + B_e v + D_e w$$

$$y_e = C_e z$$

where $w = \dot{\theta}_2$ is the parameter associated with a disturbance on speed and

$$f_e(z, v, w) = \begin{bmatrix} -\frac{R_m}{L_m} & N_m w \\ -N_m w & -\frac{R_m}{L_m} \end{bmatrix} z + \begin{bmatrix} \frac{1}{L_m} & 0 \\ 0 & \frac{1}{L_m} \end{bmatrix} v + \begin{bmatrix} 0 \\ -\frac{\Lambda_m N_m}{L_m} \end{bmatrix} w$$

$$C_e = \begin{bmatrix} 1 & 0 \\ 0 & 1 \end{bmatrix}.$$

The design goal is to generate currents that will track the slow subsystem torque requests

$$r_f = \begin{bmatrix} 0 & \frac{u}{N_m \Lambda_m} \end{bmatrix}^T$$

$$\lim_{t \to \infty} z = r_f.$$

The design model is obtained by linearization with $w = 0$ inherited from equilibrium of the slow subsystem:

$$A_e = \left. \frac{\partial f_e}{\partial z} \right|_{(\bar{z},\ \bar{v},\ \bar{w})} = \begin{bmatrix} -\frac{R_m}{L_m} & 0 \\ 0 & -\frac{R_m}{L_m} \end{bmatrix}$$

$$B_e = \left. \frac{\partial f_e}{\partial v} \right|_{(\bar{z},\ \bar{v},\ \bar{w})} = \begin{bmatrix} \frac{1}{L_m} & 0 \\ 0 & \frac{1}{L_m} \end{bmatrix}.$$

The integral controller is implemented by

$$v = -K_{f_1} z - K_{f_2} \xi$$

$$\dot{\xi} = y_e - r_f$$

under the requirements that

$$(A_e,\ B_e) \sim \text{controllable}$$

and

$$\det \begin{bmatrix} A_e & B_e \\ C_e & 0 \end{bmatrix} \neq 0.$$

The linearized fast subsystem dynamics are rewritten

$$\begin{bmatrix} \dot{z} \\ \dot{\xi} \end{bmatrix} = \begin{bmatrix} A_e - B_e K_{f_1} & -B_e K_{f_2} \\ C_e & 0 \end{bmatrix} \begin{bmatrix} z \\ \xi \end{bmatrix} + \begin{bmatrix} 0 \\ -I \end{bmatrix} r_f$$

where I is the identity matrix and the following notations are defined to assist with gain evaluation:

$$A_f = \begin{bmatrix} A_e & 0 \\ C_e & 0 \end{bmatrix} \quad B_f = \begin{bmatrix} B_e \\ 0 \end{bmatrix} \quad K_f = \begin{bmatrix} K_{f_1} & K_{f_2} \end{bmatrix}.$$

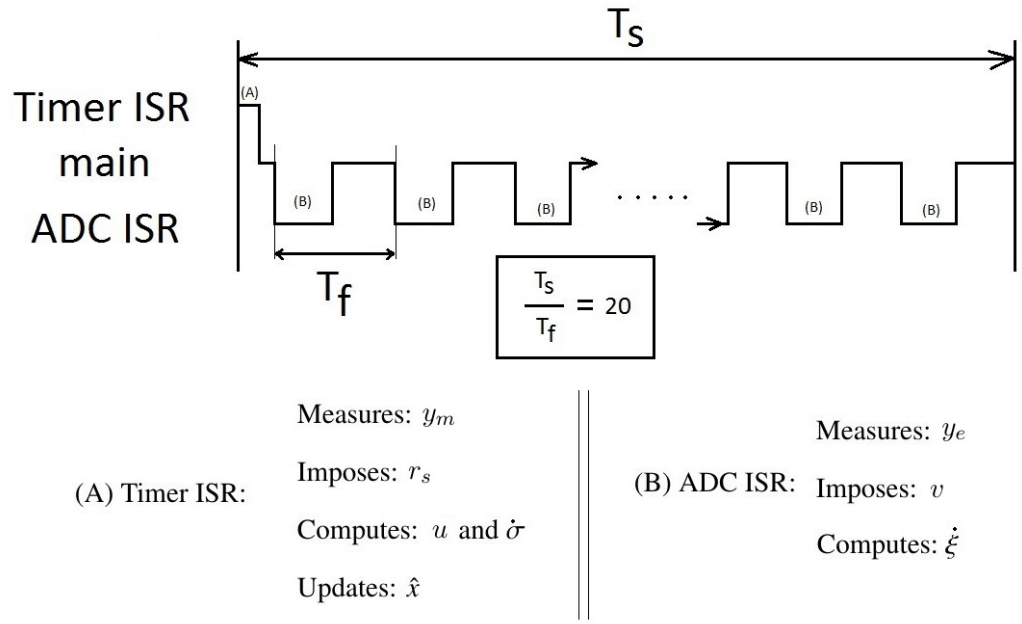

Figure 34: RWP digital implementation timing diagram.

After determining the location of slow subsystem eigenvalues, pole placement is utilized to design the gain matrix K_f so that the fast eigenvalues are located by a factor of 20 (or farther) into the left hand plane:

$$\text{eig}(A_f - B_f K_f) \quad \ll \quad \text{eig}(A_s - B_s K_s).$$

5.1.3 Implementation

A simulation study was conducted before experimental implementation to predict a successful performance while accounting for the effects of actuator saturation, integrator anti-windup, digital controller design, and parameter mismatch. In Appendix B, the mathematical descriptions of saturation, anti-windup, and the Forward Euler discretization method are found. An interrupt service routine (ISR) is triggered when some action needs to be mitigated or imposed, and in this case, a timer ISR and an ADC ISR are periodically triggered (every T_s and T_f seconds) to close the slow and fast control loops respectively. The timing diagram in Figure 34 shows when the slow and fast variables are measured, imposed, and updated during the discrete implementation.

5.1.3.1 Disturbance Rejection

A disturbance rejection study shows that we can expect to achieve the design goal independent of physical platform rotation while acting under the influence of cogging, higher-order friction, and sensor bias effects. In §4.4.4.2 and §4.4.4.4 the cogging torque and friction models are identified and parameterized:

$$T_c(\theta_2) = \sum_{n=1}^{H} \gamma_n \sin\left(nP\left(\theta - \phi\right)\right)$$

$$T_f(\dot{\theta}_2) = \alpha\,\dot{\theta}_2 + \left(\beta_c + \left(\beta_s - \beta_c\right) e^{-\left(\frac{\dot{\theta}_2}{\omega_s}\right)^2}\right) \operatorname{sgn}\left(\dot{\theta}_2\right).$$

The platform shift θ_Δ (depicted in Figure 28) has a translation effect on θ_1 such that

$$\theta_1^* = \theta_1 + \theta_\Delta \tag{28}$$

where the ideal controller is designed while assuming $\theta_\Delta = 0$. The effects of T_c and T_f enter at the slow subsystem input as torque disturbances, and the true dynamics are

$$f_m(x,u) = \begin{bmatrix} x_2 \\ a_1 \sin(x_1 + \theta_\Delta) + a_2 x_4 \\ x_4 \\ -a_1 \sin(x_1 + \theta_\Delta) - \rho a_2 x_4 \end{bmatrix} + \begin{bmatrix} 0 \\ -b \\ 0 \\ \rho b \end{bmatrix} \left(u - T_c(\theta_2) - T_f(\dot{\theta}_2)\right)$$

where the effect of sensor bias (s_b) enters through the output equation

$$y_r = C_r x$$

$$y_e = C_e x + D s_b.$$

An equilibrium analysis predicts the plant and measured output values at steady-state

$$\bar{x} = \begin{bmatrix} -\theta_\Delta & 0 & r_s & 0 \end{bmatrix}^T$$

$$\bar{y}_r = r_s$$

$$\bar{y}_e = \begin{bmatrix} -\theta_\Delta + s_b & r_s \end{bmatrix}^T$$

which are validated during implementation.

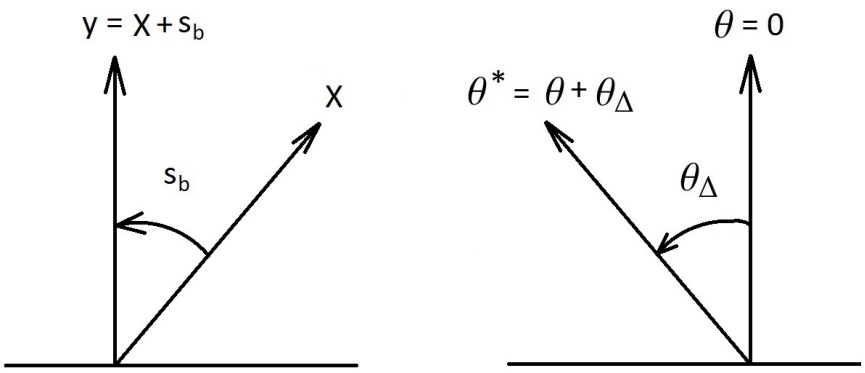

Figure 35: (Left) Sensor bias and (Right) platform rotation defects.

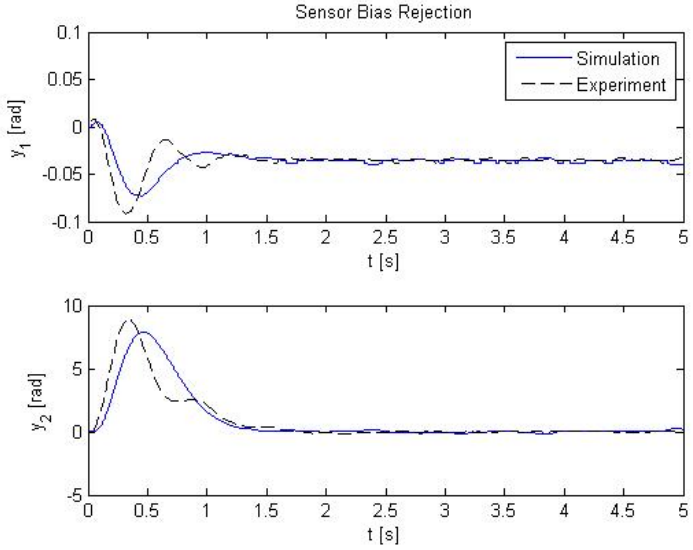

Figure 36: RWP sensor bias rejection.

5.1.3.2 Experimental Results

Since it is not possible to perform swing-up control on all systems, initialization depends on how close to perfectly upright the user can place the pendulum. Sensor bias will always be present in the system if the location of 'perfectly upright' is not known apriori. During implementation, the presented controller development successfully rejects the effects of sensor bias. The measured output at steady-state is used to infer what the sensor bias was, and simulated predictions match experimental measurements. There is a strong correlation between sensor bias rejection in simulation and experiment as confirmed in Figure 36.

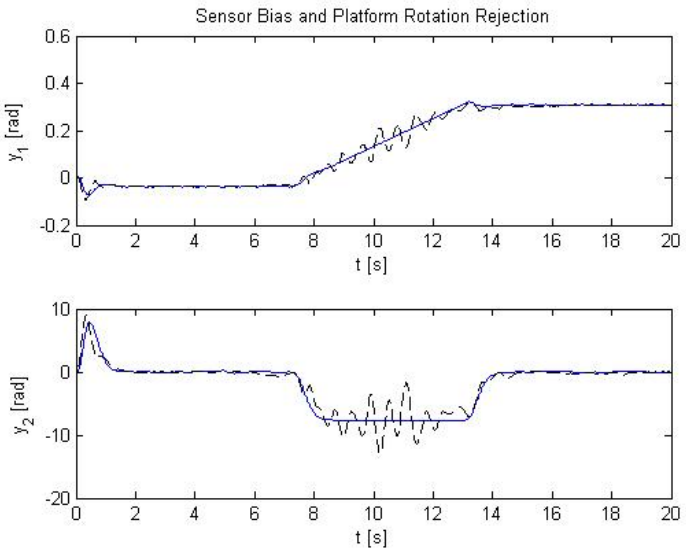

Figure 37: Experimental RWP sensor bias and platform rotation compensation.

If the ground were to shift under the pendulum or if the platform is physically rotated then θ_Δ would alter steady-state equilibrium. During the experiment, the pendulum base is physically rotated by an amount approximately measured with a protractor. Since it is not possible to mathematically represent a perfect model of how the platform is rotated (by hand), an ideal platform shift was programmed into the simulator, and the measured output at steady-state is used to infer what the sensor bias was. Simulated predictions match experimental measurements as seen in Figure 37, and a depiction of the actual system rejecting sensor bias in the presence of platform shift is seen in Figure 38.

5.2 Wheeled Inverted Pendulum

The WIP controller design goal is to maintain balance while translating, rotating, or both. An equilibrium analysis is performed on the mechanical subsystem to determine valid reference signals. Integral control is implemented on the slow (mechanical) and fast (electrical) subsystems to track ideal torque inputs and to provide ideal torque generating currents. A disturbance rejection analysis shows that the developed strategy is immune to higher-order friction and sensor bias, and stability is maintained while operating on an inclined surface. The digital controller implementation accounts for practical considerations such as actuator saturation and integrator anti-windup, and simulated performance demonstrates strong

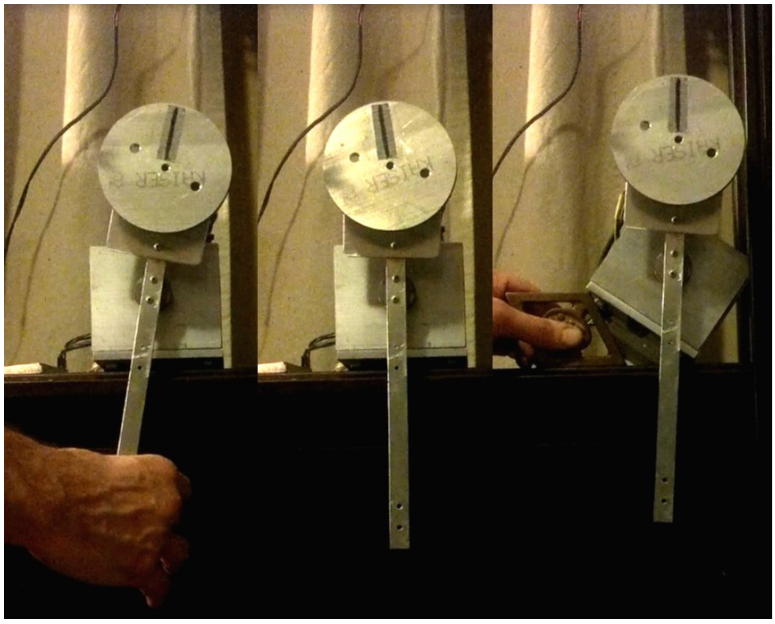

Figure 38: RWP prototype expeiencing intentional sensor bias and platform shift.

agreement with experimental measurements.

5.2.1 Equilibrium Analysis

The WIP equations of motion were derived in §3.4:

$$\begin{aligned}
\big(m_1 + 2m_w + \frac{2I_{wx}}{r^2}\big)\dot{v} - m_1 d\big(\cos\theta(\dot{\phi}^2 + \dot{\theta}^2) + \ddot{\theta}\sin\theta\big) &= \frac{1}{r}(\tau_R + \tau_L) - \frac{2k_v}{r^2}v \\
\ddot{\phi}\alpha + (I_{1y} - I_{1z})\dot{\phi}\dot{\theta}\sin(2\theta) + m_1 d\dot{\phi}v\cos\theta &= \frac{L}{2r}(\tau_R - \tau_L) - \frac{L^2 k_v}{2r^2}\dot{\phi} \\
I_{1x}\ddot{\theta} + \frac{I_{1z} - I_{1y}}{2}\dot{\phi}^2\sin(2\theta) - m_1 d\dot{v}\sin\theta &= \tau_L + \tau_R - \frac{2k_v}{r}v - dgm_1\cos\theta
\end{aligned}$$

where

$$\alpha = I_{1y}\sin^2\theta + I_{1z}\cos^2\theta + 2I_{wz} + \frac{I_{wx}L^2}{2r^2} + \frac{m_w L^2}{2}.$$

The four possible types of equilibrium are

1. standing upright
2. constant linear translation
3. constant upright rotation
4. linear translation combined with rotation (both constant)

where item 4 is a superset of items 1, 2, and 3.

All candidate equilibria are determined by first assuming

$$v = \text{constant},\ \dot{\phi} = \text{constant},\ \theta = \text{constant},\ \text{and}\ \dot{\theta} = 0, \tag{29}$$

and then analyzing the dynamic equations at steady-state, which yields

$$-m_1 d\dot{\phi}^2 \cos(\theta) = \frac{1}{r}(\tau_R + \tau_L) - \frac{2k_v}{r^2} v \tag{30}$$

$$m_1 dv\dot{\phi} \cos(\theta) = \frac{L}{2r}(\tau_R - \tau_L) - \frac{L^2 k_v}{2r^2}\dot{\phi} \tag{31}$$

$$\frac{I_{1z} - I_{1y}}{2}\dot{\phi}^2 \sin(2\theta) = \tau_L + \tau_R - \frac{2k_v}{r} v - m_1 gd\cos(\theta). \tag{32}$$

Since τ_R and τ_L are linearly independent in (30) and (31), a simple matrix equation is solved to determine the equilibrium torques

$$\tau_R = \frac{k_v}{r}\Big(v + \frac{L}{2}\dot{\phi}\Big) + \frac{m_1 dr}{L}\dot{\phi}\Big(v - \frac{L}{2}\dot{\phi}\Big)\cos(\theta)$$
$$\tau_L = \frac{k_v}{r}\Big(v - \frac{L}{2}\dot{\phi}\Big) - \frac{m_1 dr}{L}\dot{\phi}\Big(v + \frac{L}{2}\dot{\phi}\Big)\cos(\theta)$$

which upon substitution into (32) provides the constraint

$$0 = \Bigg(\underbrace{\dot{\phi}^2(I_{1z} - I_{1y})\sin(\theta) + dm_1(r\dot{\phi}^2 + g)}_{\beta}\Bigg)\cos(\theta).$$

Since d, m_1, r, $\dot{\phi}^2$, and g are all strictly positive numbers, and because it is seen in Table 2 that $I_{1z} > I_{1y}$ (listed there as I_{cz} and I_{cy}),

$$\beta = 0 \implies \sin(\theta) = -\frac{dm_1(r\dot{\phi}^2 + g)}{\dot{\phi}^2(I_{1z} - I_{1y})}$$

would require that

$$\theta \in [Q_{\mathrm{III}},\ Q_{\mathrm{IV}}]$$

however, this would mean the WIP is operating upside-down. Therefore, the only practical pendulum equilibrium position is defined by

$$\cos(\theta) = 0 \implies \theta = \frac{\pi}{2}$$

and the torques required to maintain equilibrium subject to this constraint are

$$\tau_R = \frac{k_v}{r}\Big(v + \frac{L}{2}\dot{\phi}\Big) \tag{33}$$

$$\tau_L = \frac{k_v}{r}\Big(v - \frac{L}{2}\dot{\phi}\Big). \tag{34}$$

Table 10 provides the recipe for determining any specific WIP equilibrium of interest.

Table 10: Determination of WIP Equilibria

Condition	$\bar{v}$	$\bar{\dot{\phi}}$	$\bar{\theta}$	$\bar{\dot{\theta}}$	$\bar{\tau}_R$	$\bar{\tau}_L$
Maintaining Upright Balance	0	0	$\frac{\pi}{2}$	0	0	0
Constant Linear Translation	Chosen	0	$\frac{\pi}{2}$	0	Eqn. 33	Eqn. 34
Constant Upright Rotation	0	Chosen	$\frac{\pi}{2}$	0	Eqn. 33	Eqn. 34
Constant Speed and Rotation	Chosen	Chosen	$\frac{\pi}{2}$	0	Eqn. 33	Eqn. 34

5.2.2 Controller Design

Integral control is implemented on the mechanical subsystem to track the ideal torques required to maintain equilibrium. The electrical subsystem receives these ideal torques as a reference, and integral control is implemented to generate them robustly. Output feedback is implemented on the slow subsystem to provide estimates of unmeasured mechanical states, and state feedback is implemented on the fast subsystem since all currents are directly measured. The eigenvalue locations for each subsystem are designed to provide two-time scale operation of a fast inner current loop and a slow outer mechanical loop.

5.2.2.1 Slow Subsystem

Since the wheel speeds $(\dot{\Theta}_R,\ \dot{\Theta}_L)$ are implicitly known through v and $\dot{\phi}$ under the no-slip assumption

$$\begin{aligned} \dot{\Theta}_R &= \frac{v}{r} + \frac{L}{2r}\dot{\phi} \\ \dot{\Theta}_L &= \frac{v}{r} - \frac{L}{2r}\dot{\phi}, \end{aligned} \tag{35}$$

the chosen state and input vectors are

$$\begin{aligned} x &= [v,\ \dot{\phi},\ \theta,\ \dot{\theta},\ \Theta_R,\ \Theta_L]^T \\ u &= [\tau_R,\ \tau_L]^T. \end{aligned}$$

A MIMO state-space integral controller is designed to estimate x using measurement of y_e, and regulate y_r using measurement of y_r

$$\dot{x} = f_m(x,u) \approx A_m x + B_m u$$

$$y_r = C_r x$$

$$y_m = C_m x$$

where

$$f_m(x,u) = \mathcal{M}^{-1} \begin{bmatrix} \frac{1}{r}(u_1+u_2) - \frac{2k_v}{r^2}x_1 + m_1 d\cos(x_3)({x_2}^2 + {x_4}^2) \\ \frac{L}{2r}(u_1-u_2) - \frac{L^2 k_v}{2r^2}x_2 - (I_{yy}-I_{zz})x_2 x_4 \sin(2x_3) - m_1 d x_1 x_2 \cos(x_3) \\ x_4 \\ u_1+u_2 - \frac{2k_v}{r}x_1 - dgm_1\cos(x_3) - \frac{I_{zz}-I_{yy}}{2}{x_2}^2\sin(2x_3) \\ \frac{1}{r}x_1 + \frac{L}{2r}x_2 \\ \frac{1}{r}x_1 - \frac{L}{2r}x_2 \end{bmatrix} \tag{36}$$

$$\mathcal{M} = \begin{bmatrix} a_{11} & 0 & 0 & -a_{14} & 0 & 0 \\ 0 & \alpha & 0 & 0 & 0 & 0 \\ 0 & 0 & 1 & 0 & 0 & 0 \\ -a_{41} & 0 & 0 & I_{xx} & 0 & 0 \\ 0 & 0 & 0 & 0 & 1 & 0 \\ 0 & 0 & 0 & 0 & 0 & 1 \end{bmatrix} \qquad \begin{aligned} a_{11} &= m_1 + 2m_w + \tfrac{2I_{wx}}{r^2} \\ a_{14} &= a_{41} = m_1 d\sin(x_3) \end{aligned}$$

$$C_r = \begin{bmatrix} 0 & 0 & 0 & 0 & 1 & 0 \\ 0 & 0 & 0 & 0 & 0 & 1 \end{bmatrix} \qquad C_m = \begin{bmatrix} 0 & 1 & 0 & 0 & 0 & 0 \\ 0 & 0 & 0 & 1 & 0 & 0 \\ 0 & 0 & 0 & 0 & 1 & 0 \\ 0 & 0 & 0 & 0 & 0 & 1 \end{bmatrix}. \tag{37}$$

The design goal with reference $r_s = \begin{bmatrix} \bar{\Theta}_R & \bar{\Theta}_L \end{bmatrix}^T$ is

$$\lim_{t\to\infty} y_r = r_s.$$

The design model is obtained by linearization,

$$A_m = \left.\frac{\partial f_m}{\partial x}\right|_{(\bar{x},\ \bar{u})} \quad \text{and} \quad B_m = \left.\frac{\partial f_m}{\partial u}\right|_{(\bar{x},\ \bar{u})}$$

where the coefficients cannot be written concisely; however, Appendix C demonstrates how symbolic computations can be relied upon to determine this linearization for the upright stabilization case.

The integral controller is implemented by

$$\begin{aligned} u &= -K_{s_1}\hat{x} - K_{s_2}\sigma \\ \dot{\hat{x}} &= A_m\hat{x} + B_m u - L_s(C_m\hat{x} - y_m) \\ \dot{\sigma} &= y_r - r_s \end{aligned}$$

under the requirements that

$$\begin{aligned} (A_m,\ B_m) &\sim \text{controllable} \\ (A_m,\ C_m) &\sim \text{observable} \end{aligned}$$

and

$$\det \begin{bmatrix} A_m & B_m \\ C_r & 0 \end{bmatrix} \neq 0.$$

The linearized dynamics are rewritten

$$\begin{bmatrix} \dot{x} \\ \dot{\sigma} \\ \dot{\epsilon} \end{bmatrix} = \begin{bmatrix} A_m - B_m K_{s_1} & -B_m K_{s_2} & -B_m K_{s_1} \\ C_r & 0 & 0 \\ 0 & 0 & A_m - L_s C_m \end{bmatrix} \begin{bmatrix} x \\ \sigma \\ \epsilon \end{bmatrix} + \begin{bmatrix} 0 \\ -1 \\ 0 \end{bmatrix} r_s$$

where

$$\epsilon = \hat{x} - x.$$

The following notations are defined to assist with gain evaluation:

$$A_s = \begin{bmatrix} A_m & 0 \\ C_r & 0 \end{bmatrix} \quad B_s = \begin{bmatrix} B_m \\ 0 \end{bmatrix} \quad K_s = \begin{bmatrix} K_{s_1} & K_{s_2} \end{bmatrix}.$$

The gain matrix K_s is chosen to minimize

$$\int_0^\infty (x^T Q x + u^T R u)\ dt$$

subject to the diagonal weights

$$Q_{ii} = x_{i,\max}^{-2}, \quad R_{ii} = u_{i,\max}^{-2}$$

The optimal choice of K_s is given by

$$K_s = R^{-1} B_m^T X$$

where X is the unique positive-semidefinite solution of

$$A_s^T X + X A_s - X B_s R^{-1} B_s^T X + Q = 0.$$

L_s is designed by employing a loop transfer recovery procedure that utilizes the weighting matrices

$$W = q B_m B_m^T, \quad V = I.$$

The desired choice of L_s is given by

$$L_s = Y C_m^T V^{-1}$$

where Y is the unique positive-semidefinite solution of

$$A_m Y + Y A_m^T - Y C_m^T V^{-1} C_m Y + W = 0.$$

5.2.2.2 Fast Subsystem

Since two DC motors are independently actuated to track different reference torques (u_1 and u_2), the fast subsystem design is only shown once for a general reference u corresponding to the general wheel speed $\dot{\Theta}$ of either motor ($\dot{\Theta}_L$ or $\dot{\Theta}_R$). During implementation, the design is applied to each motor which actuates due to the current flow (i) induced by imposing voltage inputs (v) on the stator. The scalar state is defined by

$$z = i.$$

A state-space integral controller is designed to regulate z using the electrical dynamics

$$\dot{z} = f_e(z, v, w) \approx A_e z + B_e v + D_e w$$

where $w = \dot{\Theta}$ contributes a torque disturbance to the fast subsystem (scaled by $D_e = \frac{K_m}{L_m}$) due to back-emf in the motor and

$$f_e(z, v, w) = -\frac{R_m}{L_m} z + \frac{1}{L_m} v - \frac{K_m}{L_m} w.$$

The design goal is to track currents that generate the torques requested (by each motor) from the slow subsystem

$$r_f = \frac{u}{K_m}$$

$$\lim_{t \to \infty} z = r_f.$$

The closed loop poles of this design are independent of w and the design model is obtained by linearization

$$A_e = \left. \frac{\partial f_e}{\partial z} \right|_{(\bar{z},\ \bar{v})} = -\frac{R_m}{L_m}$$

$$B_e = \left. \frac{\partial f_e}{\partial v} \right|_{(\bar{z},\ \bar{v})} = \frac{1}{L_m}.$$

The integral controller is implemented by

$$v = -K_{f_1} z - K_{f_2} \xi$$

$$\dot{\xi} = z - r_f$$

under the requirements that

$$\left(\frac{-R_m}{L_m},\ \frac{1}{L_m} \right) \sim \text{Controllable}$$

and

$$\det \begin{bmatrix} -\frac{R_m}{L_m} & \frac{1}{L_m} \\ 1 & 0 \end{bmatrix} = -\frac{1}{L_m} \neq 0.$$

The linearized fast subsystem dynamics are rewritten

$$\begin{bmatrix} \dot{z} \\ \dot{\xi} \end{bmatrix} = \begin{bmatrix} A_e - B_e K_{f_1} & -B_e K_{f_2} \\ 1 & 0 \end{bmatrix} \begin{bmatrix} z \\ \xi \end{bmatrix} + \begin{bmatrix} 0 \\ -1 \end{bmatrix} r_f$$

and

$$A_f = \begin{bmatrix} A_e & 0 \\ 1 & 0 \end{bmatrix} \quad B_f = \begin{bmatrix} B_e \\ 0 \end{bmatrix} \quad K_f = \begin{bmatrix} K_{f_1} & K_{f_2} \end{bmatrix}.$$

After assigning the location of slow subsystem eigenvalues, the eigenvalue locations of an LQR gain assignment are inspected to confirm that the fast eigenvalues are located by a factor of 20 (or further) into the left-hand plane:

$$\text{eig}(A_f - B_f K_f) \quad \ll \quad \text{eig}(A_s - B_s K_s).$$

5.2.2.3 Reference Tracking

There are four main families of equilibria, and the possibility exists that a designer may want to switch between these modes during implementation. The two matters to consider when switching between operating modes are: stability and reference signal generation. The equilibrium determination recipe found in Table 10 accounts for any combination of $\bar{v}$ and $\bar{\dot{\phi}}$; however, each resulting design model is slightly different. After choosing one particular gain assignment, the entire family of candidate equilibria is tested for stability by inspecting the regulator and estimator eigenvalue locations. To determine the stability of all equilibrium candidates, a grid of $(\bar{v},\ \bar{\dot{\phi}})$ ordered pairs representing the candidates is generated, the linearized design model corresponding to each candidate is determined, and the subsequent eigenvalue locations are recorded in Figures 39 and 40. Since there is some assurance that the system will remain stable when switching between operating modes, we can turn our attention towards the generation of a proper reference signal.

Under the no slip-assumption (35) the assumed steady-state wheel speeds are

$$\bar{\dot{\Theta}}_R = \frac{\bar{v}}{r} + \frac{L}{2r}\bar{\dot{\phi}}$$
$$\bar{\dot{\Theta}}_L = \frac{\bar{v}}{r} - \frac{L}{2r}\bar{\dot{\phi}},$$

which are used to update the position reference during any mode of operation by

$$r_s[k+1] = r_s[k] + T_s \begin{bmatrix} \bar{\dot{\Theta}}_R \\ \bar{\dot{\Theta}}_L \end{bmatrix}.$$

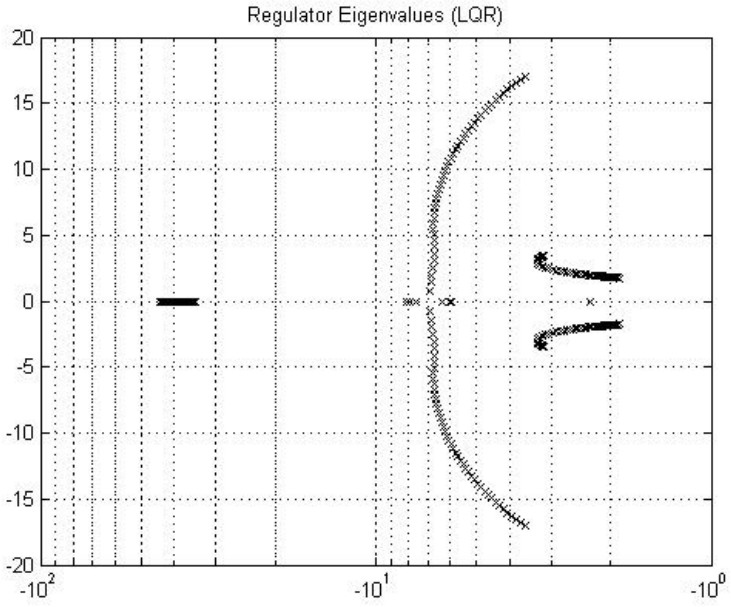

Figure 39: WIP regulator eigenvalue test: $\bar{v} \in [-10, 10]$, $\bar{\dot{\phi}} \in [-6.28, 6.28]$.

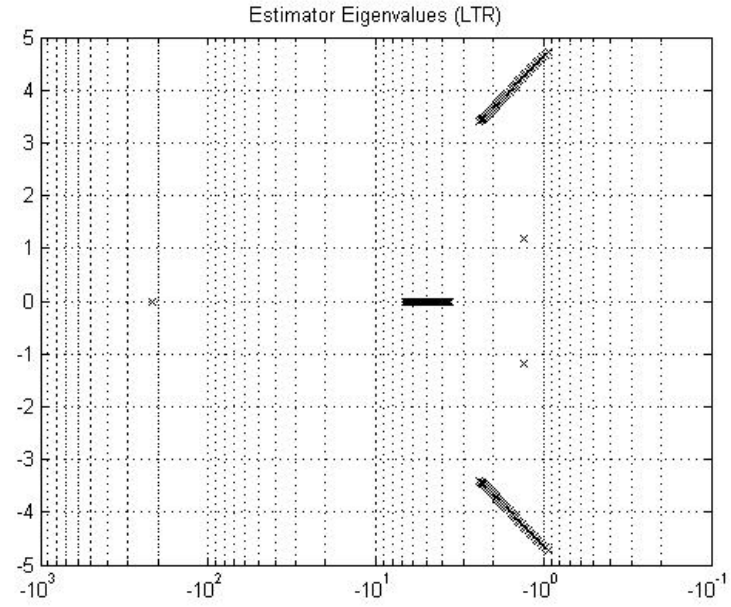

Figure 40: WIP estimator eigenvalue test: $\bar{v} \in [-10, 10]$, $\bar{\dot{\phi}} \in [-6.28, 6.28]$.

Based on the slowest eigenvalues located in Figure 39 (slightly to the left of -1), we should expect a settling time of approximately 5s, which is consistent with simulated predictions and experimental measurements.

5.2.3 Implementation

A simulation study was conducted before experimental implementation to predict a successful performance while accounting for the effects of actuator saturation, integrator anti-windup, and digital controller design. In Appendix B, the mathematical descriptions of saturation, anti-windup, and the Forward Euler discretization method are found. The disturbance rejection study in §5.2.3.2 shows that we can expect to achieve the design goal while acting under the influence of higher-order friction, and sensor bias effects. During implementation, the destabilizing effects of gearbox backlash are encountered; however, friction effects are more significant, and position reference tracking is successful.

An interrupt service routine (ISR) is triggered when some action needs to be mitigated or imposed, and in this case, a timer ISR and an ADC ISR are periodically triggered (every T_s and T_f seconds) to close the slow and fast control loops respectively. The timing diagram in Figure 41 shows when the slow and fast variables are measured, imposed, and updated during the discrete implementation. A 16-bit signed integer format is used to represent the raw inertial sensing data; however, this information is stored in two registers (8 MSBs and 8 LSBs) and can only be accessed 8-bits at a time along the I^2C data bus. The timing diagram shows how six gyroscope measurements and four accelerometer measurements are acquired while maintaining a significant time scale separation. In the timing diagram, the following terminology is used: H and L refer to the 8 MSBs or 8 LSBs transferred from the X, Y, and Z axes of the accelerometer (Accel) or gyroscope (Gyro).

5.2.3.1 Sensor Kinematics

In the output matrices (37) the four variables assumed to be measured variables are $\dot{\phi}$, $\dot{\theta}$, Θ_R and Θ_L; however, two of these ($\dot{\phi}$ and $\dot{\theta}$) are measured indirectly through kinematic relationships. In the kinematic relationships that follow, the negative signs (on a_x and a_y) and specific axis labels (x, y, z) are dependent on how the sensor is physically mounted to

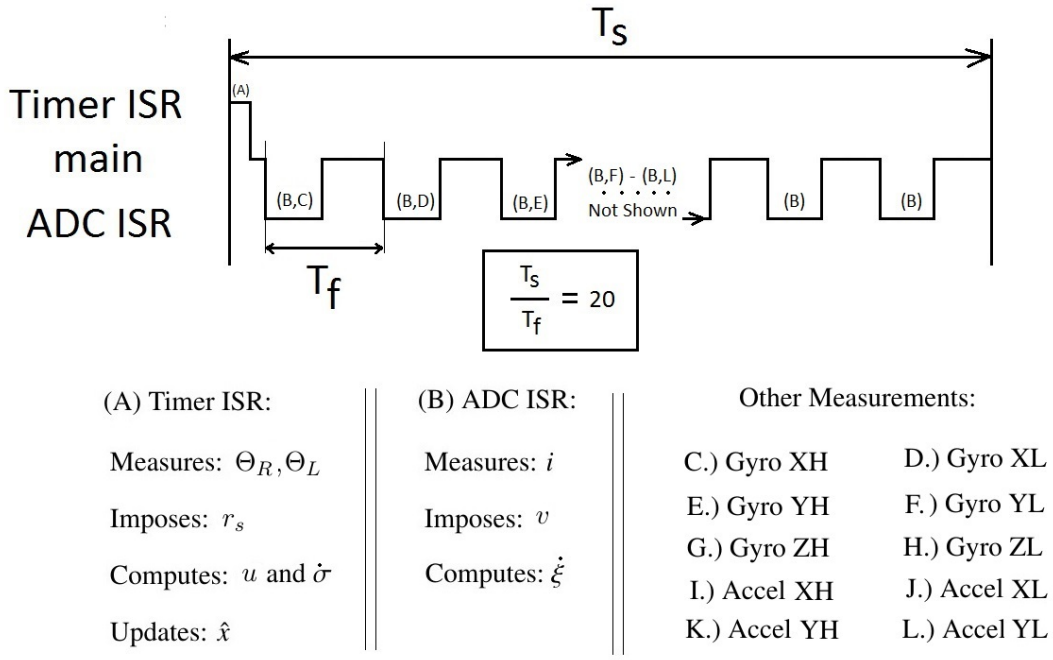

Figure 41: WBS digital implementation timing diagram.

the actual prototype and requires derivation on a project-by-project basis. After physically mounting the sensor on the prototype, these relationships are determined by comparing the dynamic model axis convention (Figure 7) against the manufacturer assigned axes found in the sensor data sheet.

Let the gyroscope measure ω_x, ω_y and ω_z, and let the accelerometer measure a_x and a_y. The pitch rate is directly obtained

$$\dot{\theta} = \omega_z.$$

The yaw rate has a nonlinear dependence on the chassis body orientation,

$$\dot{\phi} = -\omega_x \sin\theta - \omega_y \cos\theta.$$

The pitch angle is approximately measured with the accelerometer assuming that only gravity is influencing the sensor

$$\theta = \text{atan2}(\ -a_x,\ -a_y\ ).$$

Incremental encoders measure the angular rotation of both motor rotors (Θ_R and Θ_L); however, the wheels are driven by each rotor through a gearbox, so there is a scale factor difference in angular rates. The actual position of both drive wheels ($\Theta = [\Theta_R,\ \Theta_L]^T$) is

$$\Theta = \frac{\Theta_{\text{meas}}}{G_b}$$

where G_b is the gear ratio, and Θ_{meas} represents the measured values from both encoders.

5.2.3.2 Disturbance Rejection

It is an idealization to assume the WIP operates on a perfectly level surface with perfect sensor measurements, or that friction is negligible. The effects of several practical imperfections such as higher-order friction, sensor bias, and disturbances due to operating on uneven terrain are considered.

In §4.5.4.1 the friction models for both motors are identified and parameterized by

$$T_f(\dot{\Theta}) = \begin{bmatrix} \alpha_R & 0 \\ 0 & \alpha_L \end{bmatrix} \dot{\Theta} + \begin{bmatrix} \beta_{cR} & 0 \\ 0 & \beta_{cL} \end{bmatrix} \text{sgn}(\dot{\Theta}),$$

where $\dot{\Theta} = [\dot{\Theta}_R,\ \dot{\Theta}_L]^T$ and the effects of T_f enter at the slow subsystem input as a torque disturbance before gearing.

The effect of sensor bias ($s_b = [b_{\dot{\phi}},\ b_{\dot{\theta}}]^T$) is included to account for gyroscope drift or imperfect sensor placement and enters through the output equation

$$y_m = C_m x + D s_b.$$

When operating along the inclined surface, a force disturbance acting on the chassis (F_Δ) is introduced that alters both the pitch equilibrium ($\bar{\theta}$) and the torques required to maintain equilibrium. By inspecting Figure 42, the force disturbance acting on the chassis is a function of the incline angle (θ_Δ)

$$F_\Delta = (m_1 + 2m_w) g \sin(\theta_\Delta).$$

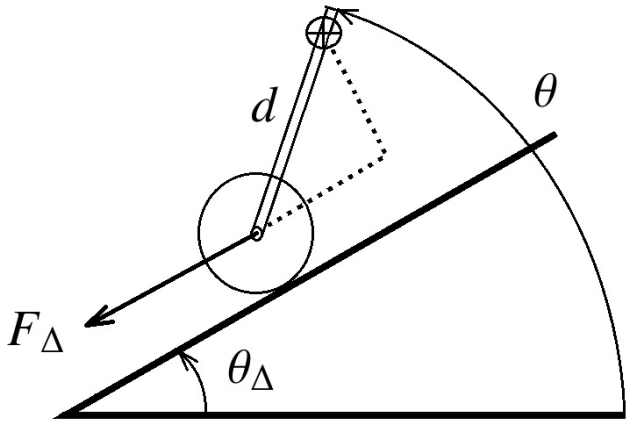

Figure 42: WIP static analysis on incline.

5.2.3.3 Equilibrium on Flat Ground

When operating on flat ground or perpendicular to an inclined surface

$$\theta_\Delta = 0, \quad F_\Delta = 0$$

and the steady-state plant and output values while either standing or experiencing constant velocities are

$$\bar{x} = \begin{bmatrix} \bar{v} \\ \bar{\dot{\phi}} \\ \bar{\theta} \\ 0 \\ r_s \end{bmatrix} \qquad \bar{y}_r = r_s$$

$$\bar{y}_m = \begin{bmatrix} \bar{\dot{\phi}} + b_{\dot{\phi}} \\ b_{\dot{\theta}} \\ r_s \end{bmatrix}$$

where v and $\dot{\phi}$ are their respective desired values, τ_R and τ_L are determined from (33) and (34), and $\bar{\theta} = \frac{\pi}{2}$.

5.2.3.4 Equilibrium on Inclined Plane

An experiment was conducted to determine the relationship between inclined surface angle and pitch equilibrium. During the experiment, the incline is manually raised and approximately measured with a protractor while the WIP is commanded to maintain upright

Figure 43: (Top) WIP standing on an incline. (Bottom) Illustrating the effect of operating on a variable incline.

balance ($v = 0$ and $\dot{\phi} = 0$), as illustrated in Figure 43. Motor currents are also measured (and scaled by the torque constant K_{DC}) to determine the torques required for maintaining equilibrium. Lagrange's method was used to derive the WIP dynamics on an incline assuming only linear motion along the inclined surface ($\dot{\phi} = 0$), which yields

$$\left(a_\Delta + 2\frac{I_w}{r^2}\right)\dot{v} - m_p d\ddot{\theta}\sin(\theta - \theta_\Delta) - m_p d\dot{\theta}^2\cos(\theta - \theta_\Delta) + a_\Delta g\sin(\theta_\Delta) = \frac{1}{r}(\tau_R + \tau_L)$$

$$(I_p + m_p d^2)\ddot{\theta} - m_p d\dot{v}\sin(\theta - \theta_\Delta) + m_p g d\cos(\theta) = \tau_R + \tau_L$$

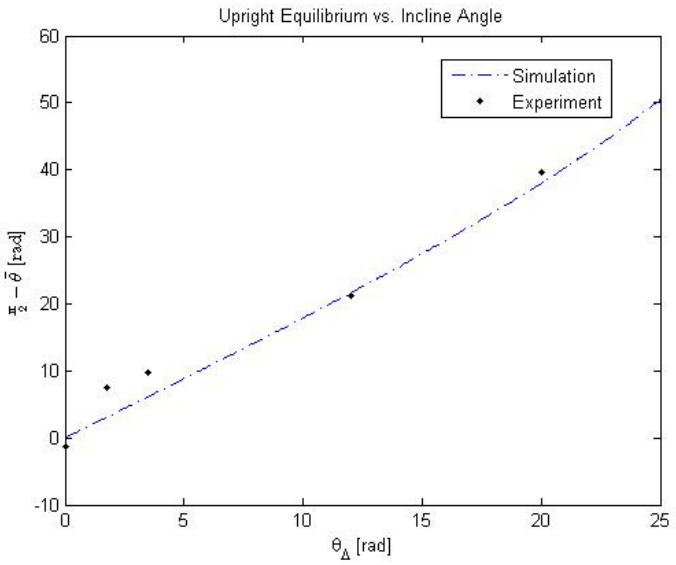

Figure 44: WIP pitch equilibrium deviation as a function of incline angle.

where $a_\Delta = m_p + 2m_w$, m_p is the chassis/pendulum mass, and m_w is the mass of each wheel. An equilibrium analysis was performed to determine formulas for equilibrium pitch,

$$\bar{\theta} = \cos^{-1}\left(\frac{r(m_p + 2m_w)\sin(\theta_\Delta)}{m_1 d}\right)$$

and two different formulas could be used to obtain the corresponding equilibrium torques,

$$\bar{\tau}_R + \bar{\tau}_L = r(m_p + 2m_w)g\sin(\theta_\Delta)$$

or

$$\bar{\tau}_R + \bar{\tau}_L = m_p dg\cos(\bar{\theta}).$$

A comparison between the computed equilibrium values and measured experimental data demonstrates a strong agreement as shown in Figures 44 and 45.

5.2.3.5 Experimental Results

During implementation, the presented controller development successfully rejects the effects of sensor bias, overcomes gearbox backlash, and demonstrates a strong agreement with simulated predictions. A picture of the WIP prototype performing upright balance is shown in Figure 46. The system successfully maintained balance in response to basic motion requests while on a flat surface or inclined plane as shown in Figures 47 and 48. Except for

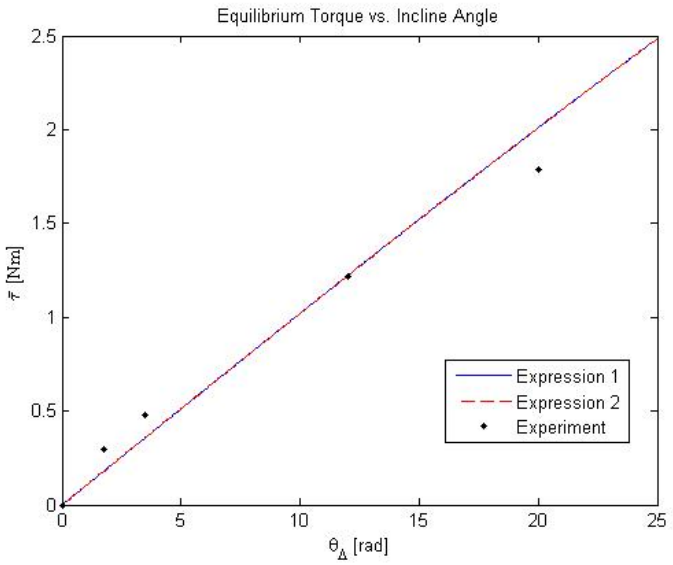

Figure 45: WIP torque equilibrium as a function of incline angle.

the accelerometer noise present in the pitch angle measurement, simulation and experiment agree very strongly.

5.3 Wheeled Balancing System

The primary WBS controller design goal is to stabilize chassis pitch while translating, rotating, or both, and to stabilize the pendulum payload at a roll angle that counteracts the effect of centripetal acceleration. The secondary controller design goal is to show that this concept works while the WBS goes over a speed bump or falls in a pothole. An equilibrium analysis is performed on the mechanical subsystem to determine valid reference signals. Integral control is simulated on the slow (mechanical) subsystem while assuming the fast (electrical) subsystem is ideal. The WBS is studied in simulation using the ideal chassis body shape shown in Figure 13 with the physical parameters listed in Table 4. Simulation trials consider the effects of cogging torque, higher-order friction effects, saturation, anti-windup, discrete control law updates, parameter mismatch, and disturbances due to operating on uneven terrain.

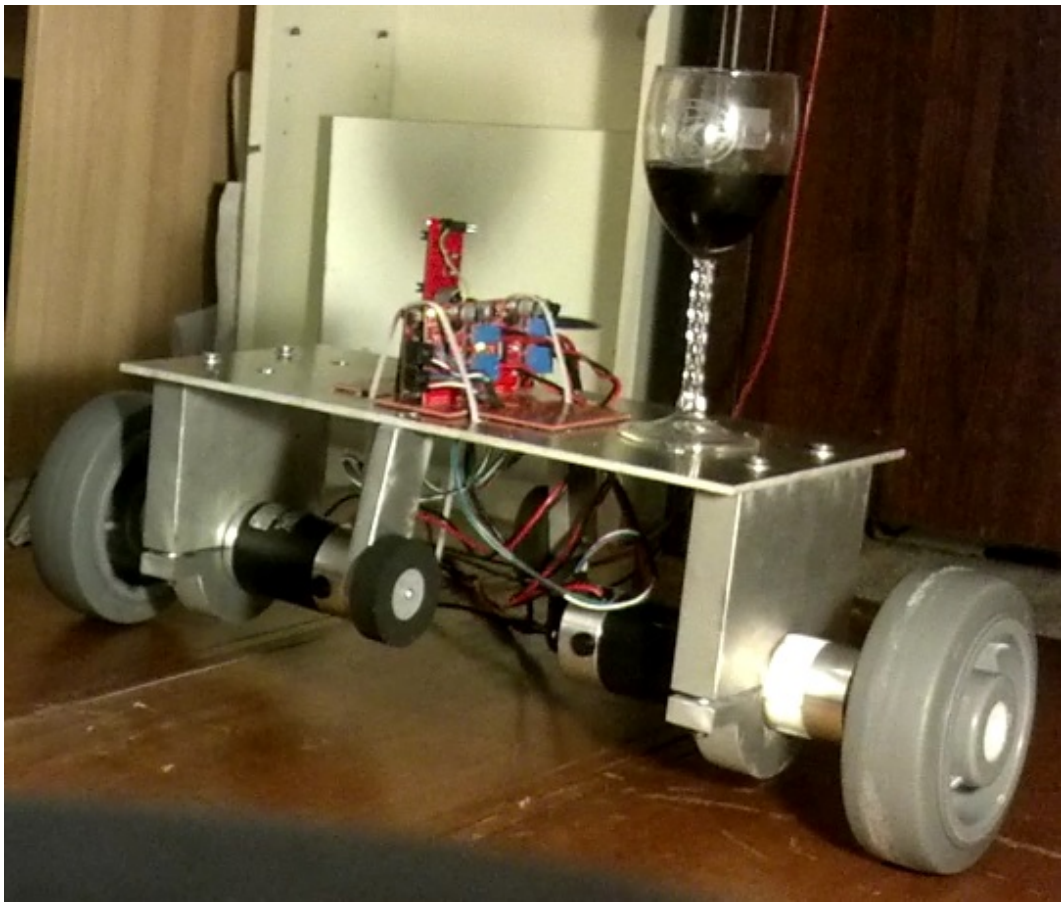

Figure 46: WIP standing upright while balancing a glass of wine.

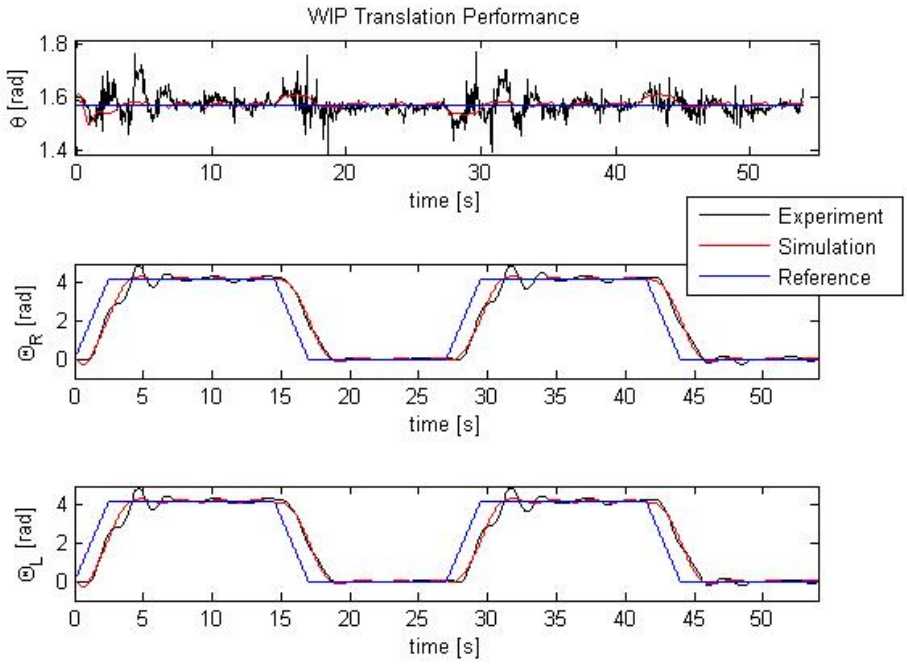

Figure 47: WIP on flat ground responding to translation commands.

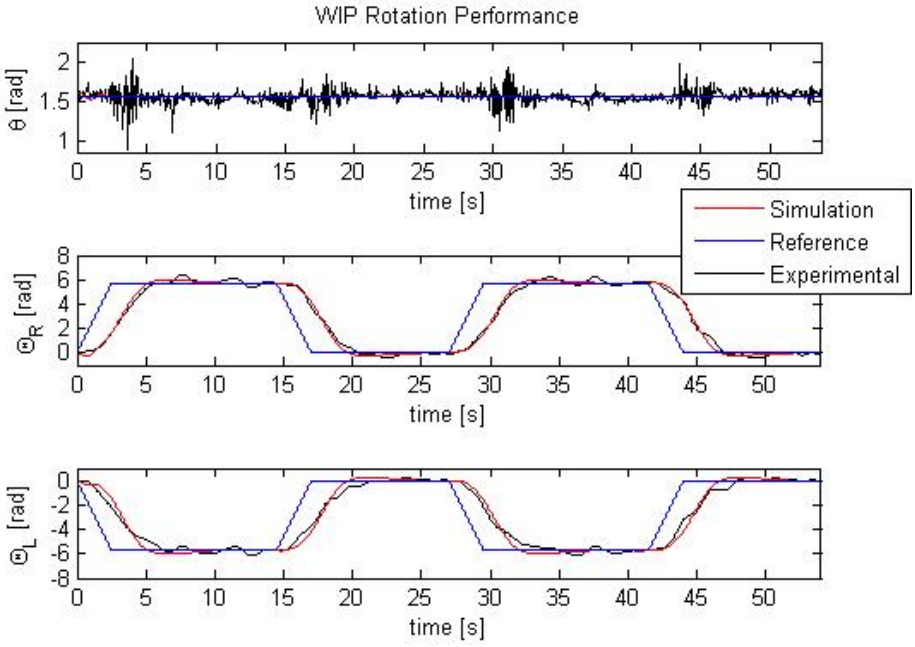

Figure 48: WIP on flat ground responding to rotation commands.

5.3.1 Equilibrium Analysis

In §3.5 the process for obtaining the WBS dynamics is detailed; however, a concise representation of the result cannot be conveyed using typeset (due to complexity) and the interested reader may see the lengthly dynamics provided in Appendix A. Since the WBS represents a mechanical superposition of the RWP and WIP, the WBS is expected to have more degrees of freedom and equilibria; however, only a few of these equilibria possess practical interest. The four modes of operation considered are

1. chassis upright and pendulum upright
2. constant chassis translation with pendulum upright
3. constant chassis rotation with pendulum upright
4. constant chassis translation and rotation with pendulum leaning

where item 4 represents a superset of items 1, 2 and 3. Intuitively speaking, item 4 is of the most interest because the WBS is capable of providing a corrective action to centripetal acceleration that the WIP alone cannot produce; much like when a runner leans into a turn with their body, instead of attempting to corner while remaining perfectly upright.

All candidate equilibria are determined by first assuming

$$v = \text{constant},\ \dot{\phi} = \text{constant},\ \theta = \text{constant},\ \psi = \text{constant},\ \text{and}\ \delta = \text{constant}$$

and then analyzing the dynamic equations at steady-state, which yields

$$-\gamma\dot{\phi}^2\cos(\theta) = \frac{1}{r}(\tau_R + \tau_L) - \frac{2k_{vw}}{r^2}v \tag{38}$$

$$\gamma\dot{\phi}v\cos(\theta) = \gamma g\cos(\theta)\sin(\psi)\sin(\theta) - \frac{L}{2r}(\tau_L - \tau_R) + \frac{L^2k_{vw}}{2r^2}\dot{\phi} \tag{39}$$

$$\frac{\beta}{2}\dot{\phi}^2\sin(2\theta) = \tau_L + \tau_R - \frac{2k_{vw}}{r}v - \gamma g\cos(\psi)\cos(\theta) \tag{40}$$

$$\dot{\phi}v = g\sin(\psi)\sin(\theta) \tag{41}$$

$$0 = \tau \tag{42}$$

where

$$\beta = m_5{d_5}^2 - I_{1y} + I_{1z} - I_{4y} + I_{4z} - I_{5y} + I_{5z}$$

$$\gamma = d_4m_4 + d_5m_5.$$

Since τ_R and τ_L are linearly independent in (38) and (39) a matrix equation is solved, and the applied torques required for all candidate equilibria are

$$\tau_R = \frac{k_{vw}}{r}(v + \frac{L}{2}\dot{\phi}) + \frac{\gamma r}{L}\Big(\dot{\phi}(v - \frac{L}{2}\dot{\phi}) - g\sin(\theta)\sin(\psi)\Big)\cos(\theta)$$
$$\tau_L = \frac{k_{vw}}{r}(v - \frac{L}{2}\dot{\phi}) - \frac{\gamma r}{L}\Big(\dot{\phi}(v + \frac{L}{2}\dot{\phi}) - g\sin(\theta)\sin(\psi)\Big)\cos(\theta)$$

which upon substitution into (40) provides the constraint

$$0 = \Bigg(\underbrace{g\cos(\psi) + \Big(\frac{\beta}{\gamma}\sin(\theta) + r\Big)\dot{\phi}^2}_{\rho}\Bigg)\cos(\theta).$$

Since d_4, d_5, m_4, m_5, r, $\dot{\phi}^2$ and g are all strictly positive numbers, and because it is shown in Table 4 that $I_{1y} = I_{1z}$, $I_{4z} > I_{4y}$, and $I_{5z} > I_{5y}$ (listed there as I_{cy}, I_{cz}, I_{pz}, I_{py}, I_{rz}, and I_{ry} respectively); then β and γ are both positive numbers.

By knowing the signs of β and γ

$$\rho = 0 \implies \cos(\psi) = -\frac{\dot{\phi}^2}{g}\Big(r + \frac{\beta}{\gamma}\sin(\theta)\Big),$$

and any solution to this constraint requires

$$\psi \in [Q_{\mathrm{II}},\ Q_{\mathrm{III}}].$$

However, since $\psi = 0$ is directed upward, this means the pendulum would need to operate upside-down. Therefore, the only practical solution is defined by

$$\cos(\theta) = 0 \implies \theta = \frac{\pi}{2}.$$

By substituting $\theta = \frac{\pi}{2}$ into (41) a constraint on the pendulum angle is determined,

$$\dot{\phi}v = g\sin(\psi) \tag{43}$$

and the torques required to maintain equilibrium are

$$\tau_R = \frac{k_{vw}}{r}\Big(v + \frac{L}{2}\dot{\phi}\Big) \tag{44}$$
$$\tau_L = \frac{k_{vw}}{r}\Big(v - \frac{L}{2}\dot{\phi}\Big). \tag{45}$$

Table 11 provides the recipe for determining any specific WBS equilibrium of interest.

Table 11: Determination of WBS Equilibria

Condition	$\bar{v}$	$\bar{\dot{\phi}}$	$\bar{\theta}$	$\bar{\psi}$	$\bar{\delta}$	$\bar{\tau}_R$	$\bar{\tau}_L$
Maintaining Upright Balance	0	0	$\frac{\pi}{2}$	0	x	0	0
Constant Linear Translation	Chosen	0	$\frac{\pi}{2}$	Eqn. 43	x	Eqn. 44	Eqn. 45
Constant Upright Rotation	0	Chosen	$\frac{\pi}{2}$	Eqn. 43	x	Eqn. 44	Eqn. 45
Constant Speed and Rotation	Chosen	Chosen	$\frac{\pi}{2}$	Eqn. 43	x	Eqn. 44	Eqn. 45

x = don't care

5.3.2 Controller Design

Simulation trials are conducted to investigate WBS performance, and since we assume that sensors can be placed everywhere to measure any state, output feedback is not required. Integral control using full-state feedback is implemented on the mechanical subsystem to track the ideal torques required to maintain equilibrium. The current dynamics are assumed to act sufficiently fast to make the actuator performance appear ideal, which is a valid assumption when current feedback loops are closed using high-gain (as demonstrated during the RWP and WIP experiments).

5.3.2.1 Slow Subsystem

Since the wheel speeds ($\dot{\Theta}_R,\ \dot{\Theta}_L$) are implicitly known through v and $\dot{\phi}$ under the no-slip assumption

$$\begin{aligned} \dot{\Theta}_R &= \frac{v}{r} + \frac{L}{2r}\dot{\phi} \\ \dot{\Theta}_L &= \frac{v}{r} - \frac{L}{2r}\dot{\phi}, \end{aligned} \tag{46}$$

the chosen state and input vectors are

$$x = [v,\ \dot{\phi},\ \theta,\ \dot{\theta},\ \psi,\ \dot{\psi},\ \dot{\delta},\ \Theta_R,\ \Theta_L]^T$$

$$u = [\tau_R,\ \tau_L,\ \tau]^T.$$

A state-space integral controller is designed to regulate y_r using measurement of y_r,

$$\dot{x} = f_m(x,u) \approx A_m x + B_m u$$

$$y_r = C_r x$$

where f_m is symbolically computed

$$A_m = \left.\frac{\partial f_m}{\partial x}\right|_{(\bar{x},\ \bar{u})} \quad \text{and} \quad B_m = \left.\frac{\partial f_m}{\partial u}\right|_{(\bar{x},\ \bar{u})}$$

with

$$C_r = \begin{bmatrix} 0 & 0 & 0 & 0 & 0 & 0 & 1 & 0 & 0 \\ 0 & 0 & 0 & 0 & 0 & 0 & 0 & 1 & 0 \\ 0 & 0 & 0 & 0 & 0 & 0 & 0 & 0 & 1 \end{bmatrix}. \tag{47}$$

The design goal with reference $r_s = \begin{bmatrix} \bar{\dot{\delta}} & \bar{\Theta}_R & \bar{\Theta}_L \end{bmatrix}^T$ is

$$\lim_{t\to\infty} y_r = r_s.$$

The integral controller is implemented by

$$u = -K_{s_1} x - K_{s_2} \sigma$$

$$\dot{\sigma} = y_r - r_s$$

under the requirements that

$$(A_m,\ B_m) \sim \text{controllable}$$

and

$$\det \begin{bmatrix} A_m & B_m \\ C_r & 0 \end{bmatrix} \neq 0.$$

The linearized dynamics are rewritten

$$\begin{bmatrix} \dot{x} \\ \dot{\sigma} \end{bmatrix} = \begin{bmatrix} A_m - B_m K_{s_1} & -B_m K_{s_2} \\ C_r & 0 \end{bmatrix} \begin{bmatrix} x \\ \sigma \end{bmatrix} + \begin{bmatrix} 0 \\ -1 \end{bmatrix} r_s.$$

The following notations are defined to assist with gain evaluation:

$$A_s = \begin{bmatrix} A_m & 0 \\ C_r & 0 \end{bmatrix} \quad B_s = \begin{bmatrix} B_m \\ 0 \end{bmatrix} \quad K_s = \begin{bmatrix} K_{s_1} & K_{s_2} \end{bmatrix}.$$

The gain matrix K_s is chosen to minimize

$$\int_0^\infty (x^T Q x + u^T R u)\ dt$$

subject to the diagonal weights

$$Q_{ii} = x_{i,\max}^{-2}, \qquad R_{ii} = u_{i,\max}^{-2}.$$

The optimal choice of K_s is given by

$$K_s = R^{-1} B_m^T X$$

where X is the unique positive-semidefinite solution of

$$A_s^T X + X A_s - X B_s R^{-1} B_s^T X + Q = 0.$$

5.3.2.2 Reference Tracking

There are four main families of equilibria, and the possibility exists that a designer may want to switch between these modes during implementation. The two matters to consider when switching between operating modes are: stability and reference signal generation. The equilibrium determination recipe found in Table 11 accounts for any combination of $\bar{v}$ and $\bar{\dot{\phi}}$; however, each resulting design model is slightly different. After choosing one particular gain assignment, the entire family of candidate equilibria is tested for stability by inspecting the regulator eigenvalue locations. To determine the stability of all equilibrium candidates, a grid of $(\bar{v}, \bar{\dot{\phi}}, \bar{\dot{\delta}})$ ordered triples representing the candidates is generated (with $\bar{\dot{\delta}} = 0$), the linearized design model corresponding to each candidate is determined, and the subsequent eigenvalue locations are recorded in Figure 49. Since there is some assurance that the system will remain stable when switching between operating modes, we can turn our attention towards the generation of a proper reference signal.

Under the no slip-assumption (46) the assumed steady-state wheel speeds are

$$\bar{\dot{\Theta}}_R = \frac{\bar{v}}{r} + \frac{L}{2r}\bar{\dot{\phi}}$$
$$\bar{\dot{\Theta}}_L = \frac{\bar{v}}{r} - \frac{L}{2r}\bar{\dot{\phi}},$$

and upon switching modes these desired speeds (with $\bar{\dot{\delta}} = 0$) are used to update the position reference

$$r_s[k+1] = r_s[k] + T_s \begin{bmatrix} 0 & \bar{\dot{\Theta}}_R & \bar{\dot{\Theta}}_L \end{bmatrix}^T.$$

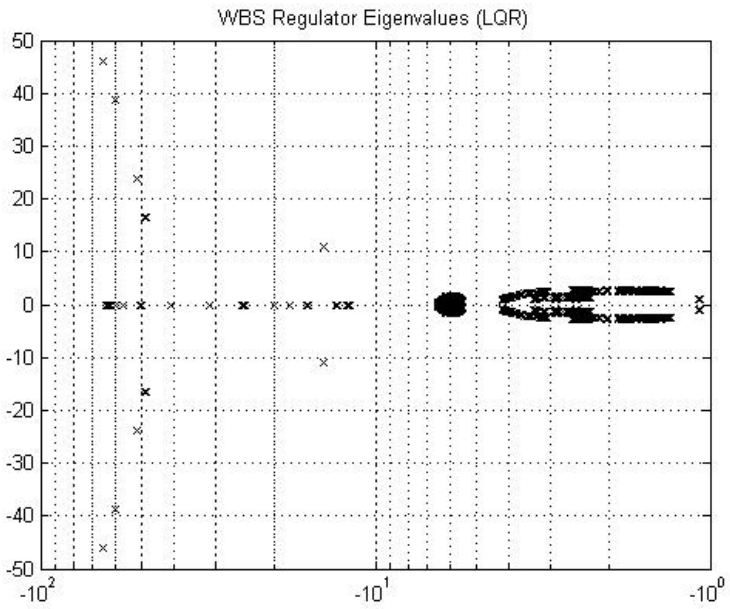

Figure 49: WBS regulator eigenvalue test: $\bar{v} \in [-10, 10]$, $\bar{\dot{\phi}} \in [-6.28, 6.28]$, $\bar{\dot{\delta}} = 0$.

Based on the slowest eigenvalues located in Figure 49 (slightly to the left of -1), we should expect a settling time of approximately 5s, which is consistent with simulated predictions.

5.3.3 Simulation Results

During simulation, the presented controller development successfully rejects the effects of higher-order friction, cogging torque, and parameter mismatch. The two complex motion references created to test the WBS performance response are an obstacle slalom and traversal over a speed bump (or pothole), as seen in Figure 50.

First, the WBS response to an S-curve trajectory (or obstacle slalom) over a flat surface is shown in Figures 51 - 53. In Figure 51 a critical observation is made along the time intervals $t \in \{[25, 30]\text{s} \cup [45, 50]\text{s}\}$ (corresponding to the times marked in Figure 50), where the WBS pendulum angle response (ψ) demonstrates static stability at angles that cancel out the effects of centripetal acceleration.

Second, the WBS response to asymmetrical wheel lift (or decline into a pothole) with a forward velocity is shown in Figures 54 - 55. The wheel lift angle (ψ_Δ) alters the WBS dynamics in the same way that the platform base roll angle altered the RWP dynamics in

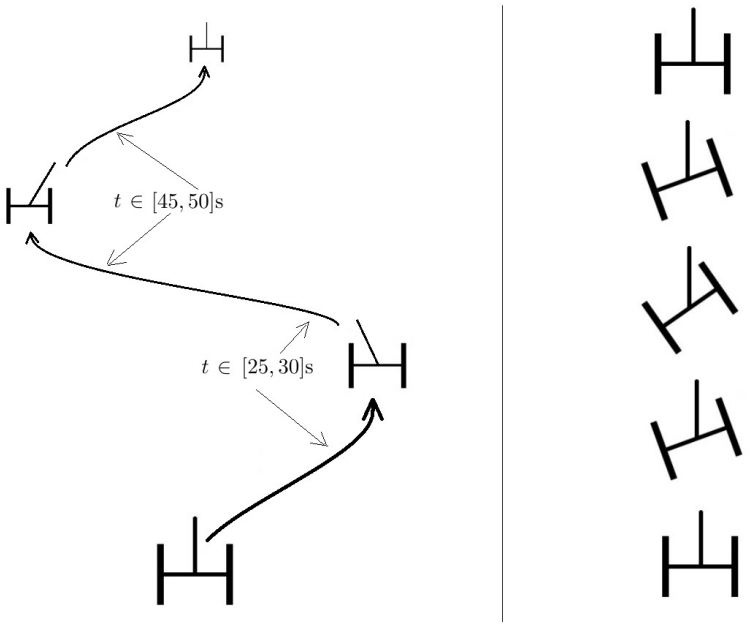

Figure 50: (Left) WBS navigating an S-curve slalom, and (Right) one wheel going over a speed bump.

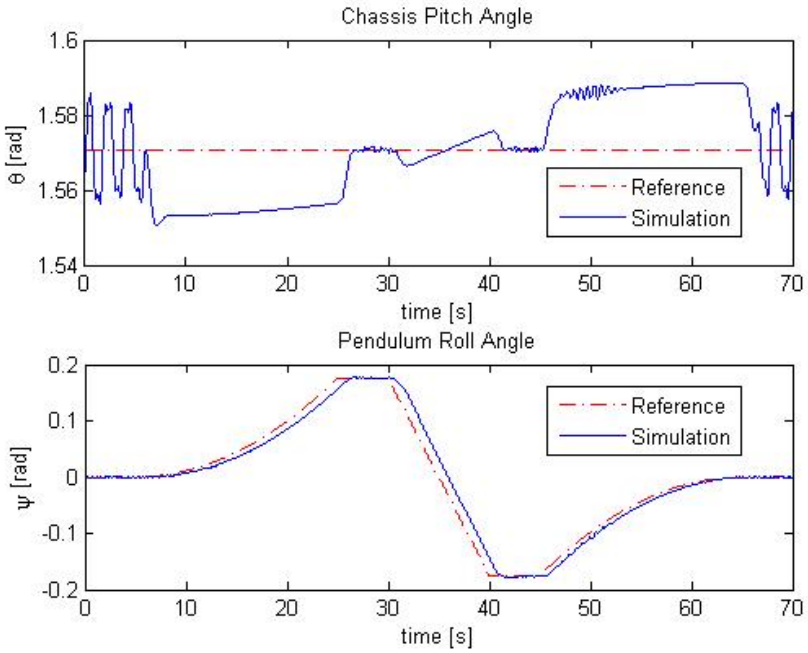

Figure 51: WBS angle responses to an S-curve trajectory.

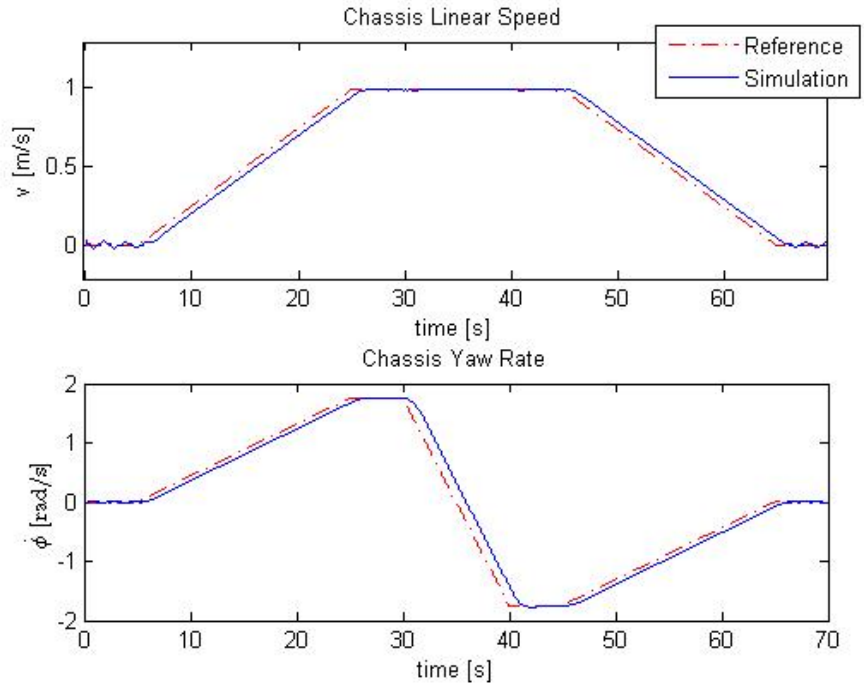

Figure 52: WBS velocity responses to an S-curve trajectory.

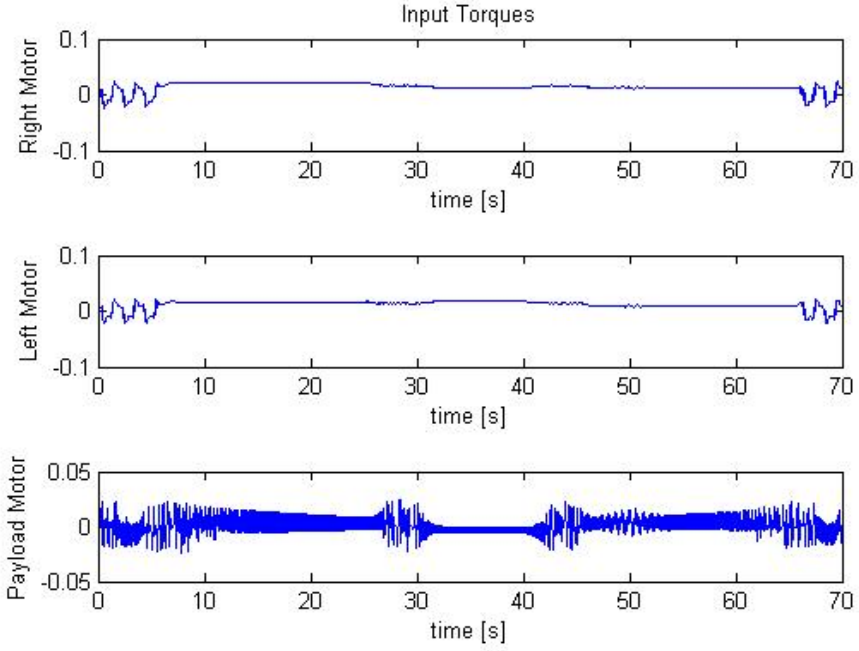

Figure 53: WBS commanded inputs for an S-curve trajectory.

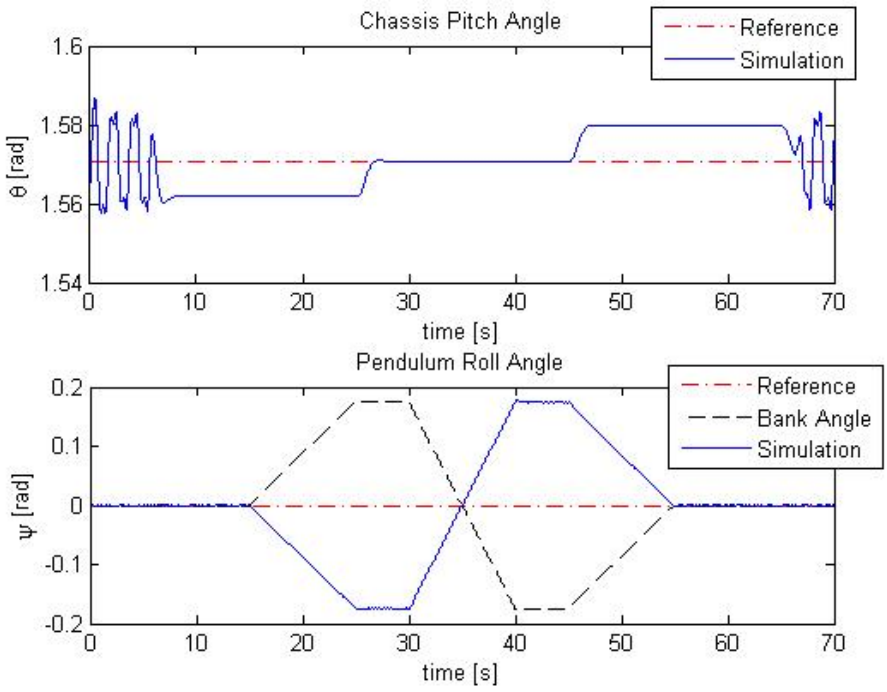

Figure 54: WBS angle responses to asymmetrical wheel lift.

(28), and the true WBS dynamics become

$$\dot{x} = f_m(x + x_\Delta, u) \tag{48}$$

where $x_\Delta = [0,\ 0,\ 0,\ 0,\ \psi_\Delta,\ 0,\ 0,\ 0,\ 0]^T$. The WBS responds to stay upright exactly like the RWP prototype did in Figure 38, except with the added complexity of doing so on wheels. As observed in Figure 54 along the time interval $t \in [15, 55]$s, the WBS pendulum angle response (ψ) is diametrically opposed to ψ_Δ. Conceptually, this means that if only one wheel hit a speed bump or fell into a hole, then the pendulum would take corrective action to remain upright.

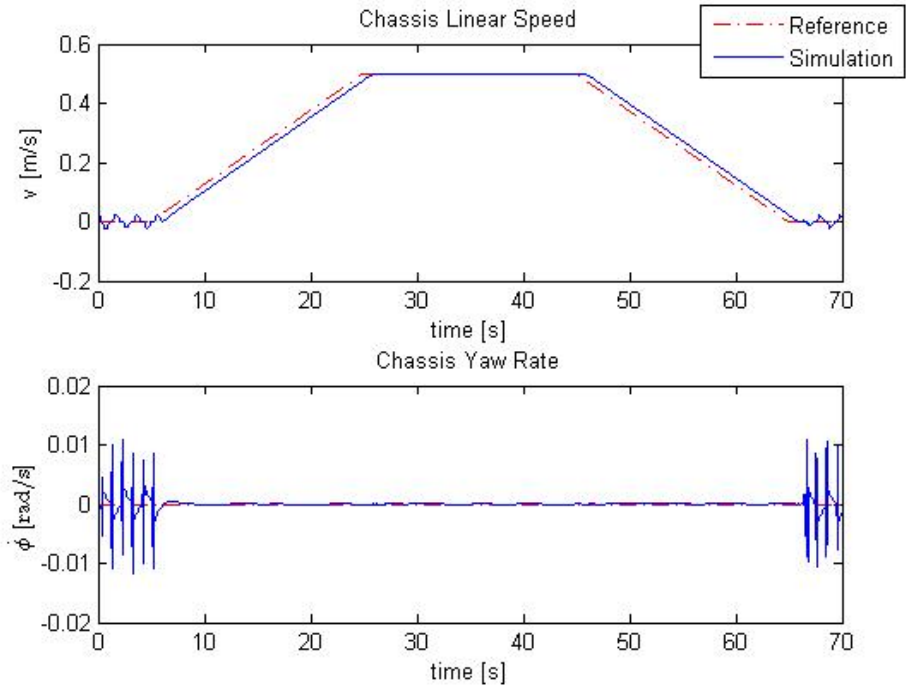

Figure 55: WBS velocity responses to asymmetrical wheel lift.

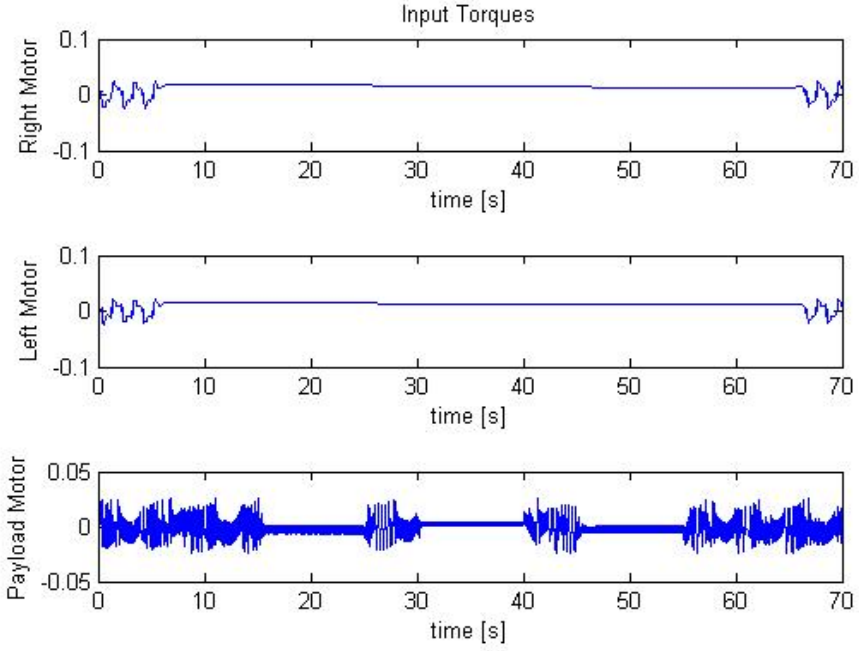

Figure 56: WBS commanded inputs for asymmetrical wheel lift.

CHAPTER VI

CONCLUSION

This dissertation provided a comprehensive modeling, identification, and control methodology for several inverted balancing systems. Symbolic software tools were created based on the general dynamic equation to derive the equations of motion for each system. Embedded programming techniques were designed and implemented to acquire data, perform sensor calibration, and impose actuator voltages. Actuator nonlinearities were characterized using only the hardware intended for implementation by processing the measured responses to specific embedded experiments; this low-cost approach did not require additional measurement devices or other expensive high-precision equipment.

State-space integral controllers were designed to provide robust feedback compensation while tracking reference signals. Several practical implementation issues were investigated such as disturbance rejection, digital controller design, switched mode reference tracking, and integrator anti-windup. Before each implementation, a software environment was created to predict system performance with high-fidelity by testing how the full-order nonlinear plant dynamics would respond to the controller design while accounting for higher order friction effects, cogging torque, gearbox backlash, sensor bias, and parameter mismatch. Simulated predictions of the RWP and WIP are strongly validated experimental measurements, and the developed methodology was applied in simulation to successfully prove the viability of the WBS concept.

This dissertation has made novel contributions to each application studied. In the RWP application, a few efforts have been made to study four-state control [20, 28] and sensor bias rejection [1, 13]; however, until §5.1.3 none have studied the two problems together and the experimental results demonstrated in Figure 36 are the first of their kind. The RWP swing-up problem has been well studied; however, until section §5.1.3 none have studied the effect of changing the platform base roll angle and the experimental results

demonstrated in Figure 37 represent the first documented rejection of this phenomenon. The RWP was advanced in several directions by modeling the dynamics with the general dynamic equation, providing the first experimental demonstration of inertia wheel position tracking, and successfully rejecting the effects of sensor bias, cogging torque, higher-order friction, and disturbances due to operating on uneven terrain. These contributions are worth providing because mastery of RWP technology is the critical prerequisite to inventing and proving the success of the WBS concept.

The WIP has been well studied and opportunities to demonstrate novelty were limited. The WIP application has been advanced by experimentally demonstrating two-time scale state-space integral controller design with robust reference tracking while switching between equilibrium modes, and rejecting sensor bias while operating on uneven terrain as seen in Figures 47 and 48. This contribution is worth providing because proof of the WBS concept requires mastery of the WIP technology as a prerequisite.

RWP and WIP technologies have only been combined twice (in [4] and [38]); however, both physical configurations differ from the WBS concept introduced in Chapter 1, modeled in Chapter 3, and simulated in Chapter 5. Until now the technology did not exist to cancel out the effects of centripetal acceleration acting on the payload of a WIP, or to keep a WIP payload upright while riding over uneven terrain (Figures 51 and 54). These contributions are worth providing because now the technology has been invented to provide a safer WIP riding experience for human operators.

APPENDIX A

WBS DYNAMIC EQUATIONS

$$m_1\dot{v} + m_4\dot{v} + m_5\dot{v} + 2m_w\dot{v} + (2I_{wx}\dot{v})/r^2 - d_4m_4\dot{\phi}\dot{\psi} - d_5m_5\dot{\phi}\dot{\psi} - d_4m_4\ddot{\theta}\sin\theta - d_5m_5\ddot{\theta}\sin\theta - d_4m_4\dot{\phi}^2\cos\theta - d_5m_5\dot{\phi}^2\cos\theta - d_4m_4\dot{\psi}^2\cos\theta - d_5m_5\dot{\psi}^2\cos\theta - d_4m_4\dot{\theta}^2\cos\theta - d_5m_5\dot{\theta}^2\cos\theta - d_5\dot{\delta}m_5\dot{\phi}\cos\theta^2 - d_4m_4\dot{\phi}\dot{\psi}\cos\theta^2 - d_5m_5\dot{\phi}\dot{\psi}\cos\theta^2 - d_5\dot{\delta}m_5\dot{\psi}\cos\theta = (\tau_L - (k_{vw}(v - (L\dot{\phi})/2))/r)/r + (\tau_R - (k_{vw}(v + (L\dot{\phi})/2))/r)/r$$

$$(2I_{wz} + (L^2m_w)/2 + I_{1z}\cos(\theta)^2 + I_{4z}\cos(\theta)^2 + I_{5z}\cos(\theta)^2 + I_{1y}\sin(\theta)^2 + I_{4y}\sin(\theta)^2 + I_{5y}\sin(\theta)^2 + (I_{wx}L^2)/(2r^2) + d_5^2m_5\cos(\theta)^2)\ddot{\phi} + (d_4m_4\dot{\phi}\cos(\theta) + d_5m_5\dot{\phi}\cos(\theta) + d_5\dot{\delta}m_5\cos(\theta)^2 + d_4m_4\dot{\psi}\cos(\theta)^2 + d_5m_5\dot{\psi}\cos(\theta)^2)v + I_{5z}\ddot{\delta}\cos(\theta) + I_{4z}\ddot{\psi}\cos(\theta) + I_{5z}\ddot{\psi}\cos(\theta) + I_{5x}\dot{\delta}\dot{\theta}\sin(\theta) - I_{5z}\dot{\delta}\dot{\theta}\sin(\theta) + I_{4x}\dot{\psi}\dot{\theta}\sin(\theta) - I_{4z}\dot{\psi}\dot{\theta}\sin(\theta) + I_{5x}\dot{\psi}\dot{\theta}\sin(\theta) - I_{5z}\dot{\psi}\dot{\theta}\sin(\theta) + I_{1y}\dot{\phi}\dot{\theta}\sin(2\theta) - I_{1z}\dot{\phi}\dot{\theta}\sin(2\theta) + I_{4y}\dot{\phi}\dot{\theta}\sin(2\theta) - I_{4z}\dot{\phi}\dot{\theta}\sin(2\theta) + I_{5y}\dot{\phi}\dot{\theta}\sin(2\theta) - I_{5z}\dot{\phi}\dot{\theta}\sin(2\theta) + d_5^2m_5\ddot{\psi}\cos(\theta) - d_5^2m_5\dot{\phi}\dot{\theta}\sin(2\theta) = \cos(\theta)(\tau - \dot{\delta}k_{v5}) + \cos(\theta)(\dot{\delta}k_{v5} - \tau + d_4gm_4\sin(\psi)\sin(\theta)) - (L(\tau_L - (k_{vw}(v - (L\dot{\phi})/2))/r))/(2r) + (L(\tau_R - (k_{vw}(v + (L\dot{\phi})/2))/r))/(2r) + d_5gm_5\cos(\theta)\sin(\psi)\sin(\theta)$$

$$(m_5d_5^2 + I_{1x} + I_{4x} + I_{5x})\ddot{\theta} + d_5m_5((d_5\sin(2\theta)\dot{\phi}^2)/2 + d_5\dot{\psi}\sin(\theta)\dot{\phi} - \dot{v}\sin(\theta)) - (I_{1y}\dot{\phi}^2\sin(2\theta))/2 + (I_{1z}\dot{\phi}^2\sin(2\theta))/2 - I_{4y}\dot{\phi}\sin(\theta)(\dot{\psi} + \dot{\phi}\cos(\theta)) + I_{4z}\dot{\phi}\sin(\theta)(\dot{\psi} + \dot{\phi}\cos(\theta)) - d_4m_4\dot{v}\sin(\theta) - I_{5y}\dot{\phi}\sin(\theta)(\dot{\delta} + \dot{\psi} + \dot{\phi}\cos(\theta)) + I_{5z}\dot{\phi}\sin(\theta)(\dot{\delta} + \dot{\psi} + \dot{\phi}\cos(\theta)) = \tau_L + \tau_R - (k_{vw}(v - (L\dot{\phi})/2))/r - (k_{vw}(v + (L\dot{\phi})/2))/r - d_4gm_4\cos(\psi)\cos(\theta) - d_5gm_5\cos(\psi)\cos(\theta)$$

$$(m_5d_5^2 + I_{4z} + I_{5z})\ddot{\psi} + I_{5z}\ddot{\delta} + (d_4m_4\dot{\phi} + d_5m_5\dot{\phi} + d_5\dot{\delta}m_5\cos(\theta) + d_4m_4\dot{\psi}\cos(\theta) + d_5m_5\dot{\psi}\cos(\theta))v + I_{4z}\ddot{\phi}\cos(\theta) + I_{5z}\ddot{\phi}\cos(\theta) - I_{4x}\dot{\phi}\dot{\theta}\sin(\theta) + I_{4y}\dot{\phi}\dot{\theta}\sin(\theta) - I_{4z}\dot{\phi}\dot{\theta}\sin(\theta) - I_{5x}\dot{\phi}\dot{\theta}\sin(\theta) + I_{5y}\dot{\phi}\dot{\theta}\sin(\theta) - I_{5z}\dot{\phi}\dot{\theta}\sin(\theta) + d_5^2m_5\ddot{\phi}\cos(\theta) - 2d_5^2m_5\dot{\phi}\dot{\theta}\sin(\theta) = d_4gm_4\sin(\psi)\sin(\theta) + d_5gm_5\sin(\psi)\sin(\theta)$$

$$I_{5z}\ddot{\delta} + I_{5z}\ddot{\psi} + I_{5z}\ddot{\phi}\cos(\theta) - I_{5x}\dot{\phi}\dot{\theta}\sin(\theta) + I_{5y}\dot{\phi}\dot{\theta}\sin(\theta) - I_{5z}\dot{\phi}\dot{\theta}\sin(\theta) = \tau - \dot{\delta}k_{v5}$$

APPENDIX B

IMPLEMENTATION CONSIDERATIONS

B.1 Saturation Function

When an actuator has a bounded characteristic, the saturation function is used to limit a signal to some feasible size. The mathematical model for the saturation effect is

$$u(t) = \begin{cases} u^*(t), & \text{if } |u^*(t)| \leq u_{\max} \\ u_{\max}\text{sgn}\big(u^*(t)\big), & \text{otherwise} \end{cases}$$

where $u(t)$ is a bounded signal, $u^*(t)$ is the desired signal, and $\text{sgn}(u^*(t))$ represents desired signal polarity. The saturation function only influences a signal if the signal amplitude exceeds some capability bound. Plant model simulations and control law updates should utilize this model to predict or implement a realizable performance.

B.2 Anti-Windup

During the implementation of integral control, it is not appropriate to integrate output error when the actuator is saturated. If the system has not reached the design goal but the actuator has saturated, then further increases in the feedback signal magnitude are not practical. One simple way to implement integrator anti-windup is to perform conditional integration so that the output error is only integrated when the actuator has not saturated. The mathematical model for performing conditional integration is

$$u^*(t) = -K_1 x(t) - K_2 \sigma(t)$$

$$u(t) = \begin{cases} u^*(t), & \text{if } |u^*(t)| \leq u_{\max} \\ u_{\max}\text{sign}\big(u^*(t)\big), & \text{otherwise} \end{cases}$$

$$\dot{\sigma}(t) = \begin{cases} x(t) - r(t), & \text{if } |u^*(t)| \leq u_{\max} \\ 0, & \text{otherwise} \end{cases}$$

where $\sigma(t)$ is the integrator output, $u^*(t)$ is a signal potentially subject to saturation, and x is some state vector of interest.

B.3 Forward Euler Discretization

When implementing feedback control using a microcontroller corrective actions are provided on a discrete-time basis. One simple discretization scheme is the Forward-Euler method which relies on taking the definition of a derivative and approximating it over small intervals of time (Δt),

$$\dot{x}(t) = \lim_{\Delta t \to 0} \frac{\Delta x}{\Delta t} \approx \frac{x(t + \Delta t) - x(t)}{\Delta t}$$

and when implementing $\Delta t = T$ during iteration k, variables are updated discretely according to

$$x[k + 1] = x[k] + T\dot{x}(kT).$$

APPENDIX C

WIP EQUILIBRIUM COMPUTATIONS

```
% Symbolic variables used for design
syms('z1','z2','z3','z4','z5','z6','u1','u2','real')

% Intermediate coefficients
a11 = (m1 + 2*mw + 2*Iwx/r^2);
a13 = m1*d*sin(z3);
a22 = (Iyy*sin(z3)^2 + Izz*cos(z3)^2 + mw*L^2/2 + 2*Iwz+ (Iwz*L^2)/(2*r^2));
a33 = Ixx;
b1 = d*m1*cos(z3)*z2^2 + d*m1*cos(z3)*z4^2  - 2*kv/r^2*z1;
b2 = - kv*L^2/(2*r^2)*z2 + Izz*z2*z4*sin(2*z3) - Iyy*z2*z4*sin(2*z3) - d*m1*z2*z1*cos(z3);
b3 = - (Izz*z2^2*sin(2*z3))/2 + (Iyy*z2^2*sin(2*z3))/2 - d*g*m1*cos(z3) - 2*kv/r*z1 ;
c1 = 1/r;
c2 = L/(2*r);
c3 = 1;

LHS = [a11 0 -a13;0 a22 0; -a13 0 a33];
RHS = [b1+c1*(u1+u2);b2+c2*(u1-u2);b3+c3*(u1+u2)];
WDY = [1/r*(z1+L/2*z2);1/r*(z1-L/2*z2)];
EQNs = LHS^-1*RHS;
NLN = [EQNs(1:2);z4;EQNs(3);WDY];

equilibArgs = [ z1; z2; z3; z4; z5; z6; u1; u2];
arg1=equilibArgs;

% Equilibrium Standing
v_eq1 = 0; phid_eq1 = 0; th_eq1 = pi/2; tR_eq1 = 0; tL_eq1 = 0;
equilibVals1 = [ v_eq1;phid_eq1;th_eq1;0;0;0;tR_eq1;tL_eq1];
arg2=equilibVals1;
A1 = cast(subs(jacobian(NLN,equilibArgs(1:6)),equilibArgs,equilibVals1),'double');
B1 = cast(subs(jacobian(NLN,equilibArgs(7:8)),equilibArgs,equilibVals1),'double');
```

REFERENCES

[1] D. Block, K. Astrom and M. Spong, *The Reaction Wheel Pendulum*. Morgan & Claypool, 2007.

[2] M. Spong, P. Corke and R. Lozano, "Nonlinear control of the reaction wheel pendulum," *Automatica*, pp. 1845-51, 2001.

[3] S. Kadam and B. Seth, "LQR controller of one wheel robot stabilized by reaction wheel principle," *IEEE International Conference on Instrumentation Control and Automation*, pp. 299-303, 2011.

[4] S. Kalra, D. Patel and K. Stol, "Design and hybrid control of a two wheeled robotic platform," *Australasian Conference on Robotics and Automation*, pp. 1-7, 2007.

[5] M. Muehlebach, G. Mohanarajah and R. D'Andrea, "Nonlinear analysis and control of a reaction wheel-based 3D inverted pendulum," *IEEE Conference on Decision and Control*, pp. 1283-8, 2013.

[6] M. Gajamohan, M. Merz, I. Thommen and R. D'Andrea, "The cubli: A cube that can jump up and balance," *IEEE/RSJ International Conference on Intelligent Robots and Systems*, pp. 3722-7, 2012.

[7] S. Lee and A. Goswami, "Reaction mass pendulum (RMP): An explicit model for centroidal angular momentum of humanoid robots," *IEEE International Conference on Robotics and Automation*, pp. 4667-72, 2007.

[8] F. Jepsen, A. Soborg, A. Pedersen and Z. Yang, "Development and control of an inverted pendulum driven by a reaction wheel," *IEEE International Conference on Mechatronics and Automation*, pp. 2829-34, 2009.

[9] A. Bobtsov, A. Pyrkin and S. Kolyubin, "Adaptive stabilization of a reaction wheel pendulum on moving LEGO platform," *IEEE International Conference on Control Applications*, pp. 1218-23, 2009.

[10] R. Martinez-Soto, A. Rodriguez, O. Castillo and L. Aguilar, "Gain optimization for inertia wheel pendulum stabilization using particle swarm optimization and genetic algorithms," *International Journal of Innovative Computing, Information and Control*, pp. 4421-30, 2012.

[11] R. Iriarte, L. Aguilar and L. Fridman, "Second order sliding mode tracking controller for inertia wheel pendulum," *Journal of the Franklin Institute*, pp. 92-106, 2013.

[12] C. Aguilar-Ibanez, O. Gutierrez and M. Suarez-Castanon, "Stabilization of the strongly damping inertia wheel pendulum by a nested saturation functions," *American Control Conference*, pp. 3434-9, 2008.

[13] R. Stadlmayr, A. Siuka and H. Daxberger, "State estimators for a class of nonlinear systems," *IEEE Conference on Decision and Control*, pp. 6913-18, 2011.

[14] M. Abrahantes, J. Mulder and K. Butter, "Modeling, identification and control of an under actuated inertial wheel pendulum," *IEEE Southeastern Symposium on System Theory*, pp. 1-5, 2007.

[15] D. Luo and A. Leonessa, "Nonlinear system identification of a reaction wheel pendulum using subspace method," *American Control Conference*, pp. 4590-5, 2003.

[16] V. Hernandez and H. Sira-Ramirez, "Generalized PI control for swinging up and balancing the inertia wheel pendulum," *American Control Conference*, pp. 2809-14, 2003.

[17] B. Bapiraju, K. Srinivas, P. Kumar and L. Behera, "On balancing control strategies for a reaction wheel pendulum," *IEEE India Annual Conference*, pp. 199-204, 2004.

[18] W. Yiqing, L. Sheng and C. Qingwei, "A recursive design method of stabilization controller for the inertia wheel pendulum," *IEEE Conference on Industrial Electronics and Applications*, pp. 1333-6, 2011.

[19] R. Olfati-Saber, "Global stabilization of a flat underactuated system: the inertia wheel pendulum," *IEEE Conference on Decision and Control*, pp. 3764-5, 2001.

[20] Y. Huawen, H. Yang, H. Shuqing and G. Weihua, "Novel stabilization design for the inertia wheel pendulum," *Chinese Control Conference*, pp. 26-30, 2008.

[21] J. Huber, C. Gruber and M. Hofbaur, "Online trajectory optimization for nonlinear systems by the concept of a model control loop - applied to the reaction wheel pendulum," *IEEE International Conference on Control Applications*, pp. 935-40, 2013.

[22] B. Andrievsky, "Global stabilization of the unstable reaction-wheel pendulum," *Automation and Remote Control*, pp. 1981-93, 2011.

[23] K. Srinivas and L. Behera, "Swing-up control strategies for a reaction wheel pendulum," *International Journal of Systems Science*, pp. 1165-77, 2008.

[24] N. Qaiser, N. Iqbal and N. Qaiser, "A novel nonlinear controller design for the inertia wheel pendulum," *International Bhurban Conference on Applied Sciences & Technology*, pp. 58-62, 2007.

[25] D. Murdock and D. Taylor, "Balancing a reaction wheel pendulum with PM synchronous motor actuation," *IEEE Industrial Electronics Conference*, pp. 96-102, 2014.

[26] S. Andary, A. Chemori and S. Krut, "Estimation-based disturbance rejection in control for limit cycle generation on inertia wheel inverted pendulum testbed," *IEEE/RSJ International Conference on Intelligent Robots and Systems*, pp. 1302-7, 2009.

[27] S. Andary, A. Chemori, M. Benoit and J. Sallantin, "A dual model-free control of underactuated mechanical systems, application to the inertia wheel inverted pendulum," *American Control Conference*, pp. 1029-34, 2012.

[28] L. Aguilar, I. Boiko, L. Fridman and L. Freidovich, "Generating oscillations in inertia wheel pendulum via two-relay controller," *International Journal of Robust and Nonlinear Control*, pp. 318-30, 2012.

[29] P. Pannil, A. Klaeoyotha, P. Ukakimaparn, T. Trisuwannawat, K. Tirasesth and N. Komine, "Development of inverted pendulum system at KMITL," *IEEE International Symposium on Communications and Information Technologies*, pp. 389-93, 2008.

[30] W. Younis and M. Abdelati, "Design and implementation of an experimental Segway model," *Mediterranean Conference on Intelligent Systems and Automation*, pp. 350-4, 2009.

[31] S. Nawawi, M. Ahmad, and J. Osman, "Real-Time Control of a Two-Wheeled Inverted Pendulum Mobile Robot," *International Journal of Electrical, Computer, Energetic, Electronic and Communication Engineering*, pp. 407-12, 2008.

[32] M. Khan, M. Chaudhry, T. Tariq, Q. Fatima and U. Izhar, "Fabrication and modeling of Segway," *IEEE International Conference on Mechatronics and Automation*, pp. 280-5, 2014.

[33] L. Pinto, D. Kim, J. Lee and C. Han, "Development of a Segway robot for an intelligent transport system," *IEEE/SICE International Symposium on System Integration*, pp. 710-5, 2012.

[34] K. Goher, M. Tokhi and N. Siddique, "Dynamic modeling and control of a two wheeled robotic vehicle with a virtual payload," *ARPN Journal of Engineering and Applied Sciences*, pp. 7-41, 2011.

[35] D. Choi and J. Oh, "Human-friendly motion control of a wheeled inverted pendulum by reduced-order disturbance observer," *IEEE International Conference on Robotics and Automation*, pp. 2521-6, 2008.

[36] A. Almeshal, K. Goher and M. Tokhi, "Dynamic modeling and stabilization of a new configuration of two-wheeled machines," *Robotics and Autonomous Systems*, pp. 443-72, 2013.

[37] P. Abeygunawardhana and T. Murakami, "Vibration suppression of two-wheel mobile manipulator using resonance-ratio-control-based null-space control," *IEEE Transactions on Industrial Electronics*, pp. 4137-46, 2010.

[38] S. Larimi, P. Zarafshan and S. Moosavian, "Stabilized Supervising Control of a Two Wheel Mobile Manipulator," *International Conference on Robotics and Mechatronics*, pp. 265-70, 2013.

[39] R. Chan, K. Stol and C. Halkyard, "Review of modeling and control of two-wheeled robots," *Annual Reviews in Control* pp. 89-103, 2013.

[40] Y. Kwon, J. Son, J. Lee, J. Han and J. Lee, "Optimal posture control of two wheeled inverted pendulum robot on a slanted surface," *International Symposium on Artificial Life and Robotics*, pp. 293-6, 2011.

[41] Z. Guo, J. Xu and T. Lee, "Design and implementation of a new sliding mode controller on an underactuated wheeled inverted pendulum," *Journal of the Franklin Institute*, pp. 2261-82, 2014.

[42] L. Vermeiren, A. Dequidt, T. Guerra, H. Rago-Tirmant and M. Parent, "Modeling, control and experimental verification on a two-wheeled vehicle with free inclination: An urban transportation system," *Control Engineering Practice*, pp. 744-56, 2011.

[43] J. Huang, Z. Guan, T. Matsuno, T. Fukuda and K. Sekiyama, "Sliding-mode velocity control of mobile-wheeled inverted-pendulum systems," *IEEE Transactions on Robotics*, pp. 750-8, 2010.

[44] K. Pathak, J. Franch and S. Agrawal, "Velocity and position control of a wheeled inverted pendulum by partial feedback linearization," *IEEE Transactions on Robotics*, pp. 505-13, 2005.

[45] K. Su, Y. Chen and S. Su, "Design of neural-fuzzy-based controller for two autonomously driven wheeled robot," *Neurocomputing*, pp. 2478-88, 2010.

[46] J. Ha and J. Lee, "Position Control of Mobile Two Wheeled Inverted Pendulum Robot by Sliding Mode Control," *IEEE International Conference on Control, Automation and Systems*, pp. 715-9, 2012.

[47] D. Phaoharuhansa and A. Shimada, "Trajectory Tracking for Wheeled Inverted Pendulum Robot using Tilt Angle Control," *IEEE Industrial Electronics Conference*, pp. 4288-93, 2013.

[48] J. Villacres, M. Viscaino, M. Herrera and O. Camacho, "Controllers Comparison to stabilize a Two-sheeled Inverted Pendulum: PID, LQR and Sliding Mode Control," *International Journal of Control Systems and Robotics*, pp. 29-36, 2016.

[49] T. Ren, T. Chen and C. Chen, "Motion control for a two-wheeled vehicle using a self-tuning PID controller," *Control Engineering Practice*, pp. 365-75, 2008.

[50] R. Imamura, T. Takei and S. Yuta, "Sensor drift compensation and control of a wheeled inverted pendulum mobile robot," *IEEE International Workshop on Advanced Motion Control*, pp. 137-42, 2008.

[51] T. Kane and D. Levinson, *Dynamics Theory and Application*. McGraw-Hill, 1985.

[52] Y. Kim, S. Kim and Y. Kwak, "Dynamic Analysis of a Nonholonomic Two-Wheeled Inverted Pendulum Robot," *Journal of Intelligent and Robotic Systems*, pp. 25-46, 2005.

[53] S. Kim and S. Kwon, "Dynamic Modeling of a Two-wheeled Inverted Pendulum Balancing Mobile Robot," *International Journal of Control, Automation, and Systems*, pp. 926-33, 2015.

[54] A. Castro, C. Adams and W. Singhose, "Dynamic response characteristics of a two-wheeled inverted-pendulum transporter," *IEEE Conference on Decision and Control*, pp. 1532-7, 2013.

[55] A. Katariya, "Optimal State-Feedback and Output-Feedback Controllers for the Wheeled Inverted Pendulum System," Undergraduate Thesis, Georgia Institute of Technology, 2010.

[56] L. Ojeda, M. Raju and J. Borenstein, "FLEXnav: a fuzzy logic expert dead-reckoning system for the Segway RMP," *Proceedings of the SPIE*, pp. 11-23, 2004.

[57] S. Miao and Q. Cao, "Modeling of self-tilt-up motion for a two-wheeled inverted pendulum," *Industrial Robot: An International Journal*, pp. 76-85, 2011.

[58] M. Han, K. Kim, D. Kim and J. Lee, "Implementation of unicycle Segway using unscented Kalman filter in LQR control," *IEEE International Conference on Ubiquitous Robots and Ambient Intelligence*, pp. 695-8, 2013.

[59] H. Vasudevan, A. Dollar and J. Morrell, "Energy-based limit cycle compensation for dynamically balancing wheeled inverted pendulum machines," *ASME Dynamic Systems and Control Conference*, 9 pages, 2013.

[60] T. Schamm, M. Strand, T. Gumpp, R. Kohlhaas, J. Zollner and R. Dillmann, "Vision and ToF-based driving assistance for a personal transporter," *IEEE International Conference on Advanced Robotics*, 6 pages, 2009.

[61] D. Toishi and E. Konaka, "Point stabilization of two-wheeled vehicle based on machine learning," *IEEE International Conference on Vehicular Electronics and Safety*, pp. 175-80, 2012.

[62] T. Kuwata, M. Tanaka, M. Wada, R. Umetani and M. Ito, "Localization of Segway RMP," *SICE Annual Conference*, pp. 1675-80, 2011.

[63] J. Morrell and D. Field, "Design of a closed loop controller for a two wheeled balancing transporter," *IEEE/RSJ International Conference on Intelligent Robots and Systems*, pp. 4059-64, 2007.

[64] A. Wasif, D. Raza, W. Rasheed, Z. Farooq and S. Ali, "Design and implementation of a two wheel self balancing robot with a two level adaptive control," *IEEE International Conference on Digital Information Management*, pp. 187-93, 2013.

[65] M. Yue, X. Sun, N. Li and C. An, "Dynamic Motion Planning and Adaptive Tracking Control for a Class of Two-Wheeled Autonomous Vehicle With an Underactuated Pendular Suspension," *Journal of Dynamic Systems, Measurement, and Control*, pp. 1-11, 2015.

[66] K. Talke, L. Kelley, P. Longhini and G. Catron, "Tip-over prevention through heuristic reactive behaviors for unmanned ground vehicles," *Proceedings of the SPIE*, 11 pages, 2014.

[67] M. Alarfaj and G. Kantor, "Centrifugal Force Compensaton of a Two-Wheeled Balancing Robot," *International Confrence on Control, Automation, Robotics and Vision*, pp. 2333-8, 2010.

[68] F. Villegas, R. Hecker, M. Pena, D. Vicente and G. Flores, "Modeling of a linear motor feed drive including pre-rolling friction and aperiodic cogging and ripple," *International Journal of Advanced Manufacturing Technology*, pp. 267-77, 2014.

[69] S. Buechner, V. Schreiber, A. Amthor, C. Ament and M. Eichhorn, "Nonlinear modeling and identification of a DC motor with friction and cogging," *IEEE Industrial Electronics Conference*, pp. 3621-7, 2013.

[70] K. Shouse and D. Taylor, "A digital self-tuning tracking controller for permanent-magnet synchronous motors," *IEEE Transactions on Control Systems Technology*, pp. 412-22, 1994.

[71] C. Heiberg, "Variable periodic disturbance rejection filter," *U.S. Patent*, 5,944,761, 1999.

[72] B. Saunders, G. Heins, F. De Boer and M. Thiele, "Cogging torque estimation for sensorless PMSM," *IEEE International Conference on Electrical Machines*, pp. 2949-54, 2012.

[73] G. Heins and F. De Boer, "PMSM parameter determination using pulsating torque decoupling for feed-forward control," *IEEE International Conference on Control and Automation*, pp. 1055-61, 2009.

[74] G. Bramerdorfer, S. Winkler, M. Kommenda, G. Weidenholzer, G. Kronberger, M. Affenzeller and W. Amrhein, "Using FE calculations and data-based system identification techniques to model the nonlinear behavior of PMSMs," *IEEE Transactions on Industrial Electronics*, pp. 6454-62, 2014.

[75] M. Costa, E. Braga-Filho and A. Lima, "AC motor drive system based on a custom designed strontium ferrite motor," *IEEE Brazilian Power Electronics Conference*, pp. 844-51, 2013.

[76] A. Cavagnino, S. Saied and S. Vaschetto, "Experimental identification and reduction of acoustic noise in small brushed DC motors," *IEEE Transactions on Industry Applications*, pp. 317-26, 2014.

[77] D. Ionel, M. Popescu, M. McGilp, T. Miller and S. Dellinger, "Assessment of torque components in brushless permanent-magnet machines through numerical analysis of the electromagnetic field," *IEEE Transactions on Industry Applications*, pp. 1149-58, 2005.

[78] Z. Zhu, S. Ruangsinchaiwanich and D. Howe, "Synthesis of cogging-torque waveform from analysis of a single stator slot," *IEEE Transactions on Industry Applications*, pp. 650-7, 2006.

[79] W. Van. "Cogging Compensation in Embedded Brushless Motor Control for Haptics Applications," M.S. Thesis, Delft University of Technology, 2013.

[80] Z. Jabbour, A. Riwan, S. Moreau, J. Van Rhijn and G. Champenois, "Identification and compensation of torque ripples of a PMSM in a haptic context," *IEEE Industrial Electronics Conference*, pp. 1665-70, 2010.

[81] A. Kapun, A. Hace and K. Jezernik, "Identification of stepping motor parameters," *IEEE International Conference on Computer as a Tool*, pp. 1856-63, 2007.

[82] D. Greenwood, *Advanced Dynamics*. Cambridge, 2003.

[83] D. Taylor. ECE 4550. Class Notes, Topic: "Torque vs. speed capability of AC motor drive systems." School of Electrical and Computer Engineering, Georgia Institute of Technology, Atlanta, GA, 2014.